

# Extraction of Structural Metrics from Crossing Fiber Models

Von der Fakultät für Mathematik und Informatik  
der Universität Leipzig  
angenommene

## DISSERTATION

zur Erlangung des akademischen Grades

DOCTOR RERUM NATURALIUM

(Dr. rer. nat.)

im Fachgebiet

Informatik

vorgelegt

von Dipl.-Mat. Till W. Riffert

geboren am 08.11.1983 in Starnberg

Die Annahme der Dissertation wurde empfohlen von:

1. Prof. Dr. Gerik Scheuermann, Universität Leipzig
2. Jun.-Prof. Dr. Thomas Schultz, Universität Bonn

Die Verleihung des akademischen Grades erfolgt mit Bestehen  
der Verteidigung am 16.05.2014 mit dem Gesamtprädikat cum laude



# Abstract

---

Diffusion MRI (dMRI) measurements allow us to infer the microstructural properties of white matter and to reconstruct fiber pathways in-vivo. High angular diffusion imaging (HARDI) allows for the creation of more and more complex local models connecting the microstructure to the measured signal. One of the challenges is the derivation of meaningful metrics describing the underlying structure from the local models. The aim hereby is to increase the specificity of the widely used metric fractional anisotropy (FA) by using the additional information contained within the HARDI data.

A local model which is connected directly to the underlying microstructure through the model of a single fiber population is spherical deconvolution. It produces a fiber orientation density function (fODF), which can often be interpreted as superposition of multiple peaks, each associated to one relatively coherent fiber population (bundle). Parameterizing these peaks one is able to disentangle and characterize these bundles. In this work, the fODF peaks are approximated by Bingham distributions, capturing first and second order statistics of the fiber orientations, from which metrics for the parametric quantification of fiber bundles are derived. Meaningful relationships between these measures and the underlying microstructural properties are proposed. The focus lies on metrics derived directly from properties of the Bingham distribution, such as peak length, peak direction, peak spread, integral over the peak, as well as a metric derived from the comparison of the largest peaks, which probes the complexity of the underlying microstructure. These metrics are compared to the conventionally used fractional anisotropy (FA) and it is shown how they may help to increase the specificity of the characterization of microstructural properties.

Visualization of the micro-structural arrangement is another application of dMRI. This is done by using tractography to propagate the fiber layout, extracted from the local model, in each voxel. In practice most tractography algorithms use little of the additional information gained from HARDI based local models aside from the reconstructed fiber bundle directions. In this work an approach to tractography based on the Bingham parameterization of the fODF is introduced. For each of the fiber populations present in a voxel the diffusion signal and tensor are computed. Then tensor deflection tractography is performed. This allows incorporating the complete bundle information, performing local interpolation as well as using multiple directions per voxel for generating tracts.

Another aspect of this work is the investigation of the spherical harmonic representation which is used most commonly for the fODF by means of the parameters derived from the Bingham distribution fit. Here a strong connection between the approximation errors in the spherical representation of the Dirac delta function and the distribution of crossing angles recovered from the fODF was discovered.

The final aspect of this work is the application of the metrics derived from the Bingham fit to a number of fetal datasets for quantifying the brain's development. This is done by introducing the Gini-coefficient as a metric describing the brain's age.

# Acknowledgments

---

First and foremost, I would like to express my deep gratitude to my two supervisors Dr. Thomas Knösche and Prof. Dr. Gerik Scheuermann. Especially the numerous scientific discussions with Thomas and his constructive and thorough reviews greatly improved my work.

I am very thankful to my co-supervisor Dr. Alfred Anwander and his constant support as well as his input on all questions. The discussions with him as well as his encyclopedic knowledge of about everything written in the field of neuroscience proved invaluable more than once.

To my colleagues David Moreno, Marie Uhlig, Marieke van der Steen, Jan Schreiber, and Ralph Schurade: Thank you so much for all your help and support! It was great working with you. Having people around who are at the same point in their PhD was great for the exchange of ideas, concepts and questions. Furthermore I want to thank everyone from the group “MEG and EEG - cortical networks and cognitive functions” for the discussions, the input and the overall great time. I am grateful to have met all of you.

Huge thanks to Adrian Viehweger, with whom I had the joy of working together. I really hope our next projects are as successful as the last one.

A special thanks at this point to my parents, who always supported me and nurtured my love for science from a young age. Without them I would not be who I am today.

Finally many thanks to my wife Yiyang for her continued support and understanding throughout the whole time of my PhD studies, especially during the last stretch of writing my thesis.

Part of this work was supported and financed by the FET project CONNECT of the EU ([www.brainconnect.eu](http://www.brainconnect.eu)).



# Contents

---

Abstract.....	iii
Acknowledgments.....	v
Contents.....	vii
1 Introduction.....	1
1.1 Motivation.....	1
1.2 Outline and Contributions.....	4
2 Background.....	6
2.1 Introduction.....	6
2.2 Brain Tissue .....	8
2.3 Physics of MRI .....	10
2.3.1 Spins and Magnetic Fields.....	10
2.3.2 $T_1$ -relaxation.....	13
2.3.3 $T_2$ -relaxation.....	15
2.3.4 MRI Measurements .....	17
2.3.5 Diffusion MRI .....	18
2.4 Conclusions.....	20
3 Spherical Harmonics .....	21
3.1 Introduction.....	21
3.2 Laplace's Equation.....	21
3.3 Spherical Harmonic Functions.....	22
3.4 Spherical Harmonic Expansion .....	23
3.5 Interpretation of the Coefficients .....	26
3.6 Funk-Hecke Theorem .....	27
3.7 Spherical Convolution Theorem.....	29
3.8 Sampling Theorem .....	30
3.9 Conclusion .....	30

4	Local Modeling.....	32
4.1	Introduction.....	32
4.2	The Diffusion Propagator .....	35
4.3	Diffusion Tensor .....	36
4.3.1	Introduction .....	36
4.3.2	Calculation of the Tensor from the Diffusion Signal.....	39
4.3.3	Tensor Metrics .....	41
4.3.4	Advantages and Limitations of the Diffusion Tensor.....	43
4.4	Diffusion Orientation Density Function .....	44
4.4.1	Introduction .....	44
4.4.2	General Definitions .....	45
4.4.3	Linear dODF.....	46
4.4.4	General dODF.....	48
4.4.5	Calculation of the dODF from the Diffusion Signal.....	50
4.4.6	dODF Metrics .....	51
4.4.7	Advantages and Limitations of the dODF .....	52
4.5	Fiber Orientation Density Function.....	52
4.5.1	Introduction .....	52
4.5.2	Math of Spherical Deconvolution .....	53
4.5.3	Calculation from the measured signal.....	55
4.5.4	Metrics from Spherical Deconvolution .....	58
4.5.5	Problems arising in Spherical Deconvolution .....	59
4.5.6	Crossing Angle Distribution Derived from CSD.....	62
4.5.7	Advantages and limitations .....	64
4.6	Conclusion .....	64
5	Bingham Fit.....	66
5.1	Introduction.....	66
5.2	Bingham Distribution .....	67
5.3	fODF Fitting Process .....	68



5.4	Conclusion .....	72
6	Bingham Metrics.....	73
6.1	Introduction.....	73
6.2	Bingham Function Parameters.....	74
6.3	Fiber Density (FD) .....	76
6.4	Fiber Spread (FS) .....	76
6.5	Structural Complexity (CX) .....	77
6.6	Evaluating Metrics.....	78
6.6.1	Introduction .....	78
6.6.2	Data Generation and Measurements .....	79
6.6.3	Simulated Data.....	82
6.6.4	Phantom Data .....	84
6.6.5	Human Brain Data.....	86
6.7	Conclusion .....	89
7	Bingham Fit Tractography .....	93
7.1	Introduction.....	93
7.2	Tensor Deflection .....	94
7.3	Tensor Calculation from the Bingham Fit .....	94
7.4	Results .....	96
7.5	Conclusion .....	97
8	Fetus Data Analysis.....	99
8.1	Introduction.....	99
8.2	Measurements .....	101
8.3	Results .....	102
8.4	Conclusions.....	104
9	General Discussion .....	105
10	Abbreviations.....	109
11	List of Figures .....	111
12	References .....	118

Curriculum Vitae.....	128
Selbstständigkeitserklärung.....	130

# 1 Introduction

---

## 1.1 Motivation

The human brain is an utterly complex organ and still many parts of its structure and working remain unknown. It consists in large parts of so called neurons (nerve cells), which are responsible for the transfer of information. The neurons prolongation is called axon (nerve fiber). These axons are in most cases organized in directionally aligned populations (bundles). The only ways to gain insight on the architecture of these fiber bundles and their properties used to involve cerebral dissection (Curran, 1909). The greatest advance for the study of the brains architecture in-vivo was diffusion magnetic resonance imaging (dMRI). The foundation for dMRI is that molecules are in constant motion due to their thermal energy (Brownian Motion) (Brown, 1827). The pathway of a particle is guided by the collision with other molecules, membranes or structural barriers. In dMRI this random displacement (diffusion) can be observed within a small (size  $1\text{-}30\text{mm}^3$ ) spatial volume (voxel) in terms of the dephasing of water molecules in the presence of a spatially varying magnetic field (Bihan et al., 1986; Merboldt et al., 1985; Taylor and Bushell, 1985). Hereby the diffusion is observed in a number of angular directions, guided by the so called diffusion gradients. This leads to a voxel-wise signal profile reflecting the local tissue structure, as the fiber bundles hinder diffusion perpendicular to their main direction (P J Basser et al., 1994a, 1994b). The number of diffusion gradients determines the angular resolution at which the signal profile is measured. If a large number of diffusion gradients (more than 40) are used, this method is referred to as high angular resolution diffusion imaging (HARDI).

In order to draw conclusions on the underlying fiber structure from the measured diffusion weighted signal, it is necessary to impose a model connecting anatomy and diffusion signal. This model is called the local model, because it describes the influence of the local microstructural boundaries within a voxel on the spatial displacement of water molecules (i.e. diffusion), thereby it describes the influence on the measured signal from that voxel. In many cases, approximations of the average water diffusion propagator  $p(r, t)$  in the voxel are constructed. This function gives the ensemble averaged probability of a water molecule traveling the distance  $r$  within time  $t$  (Callaghan, 1991; Cory et al., 1990). It is related to the underlying tissue structure by the diffusion equation and the appropriate boundary conditions. In practice, probing the diffusion propagator is constrained by sensitivity of the measurement with respect to diffusion direction, governed by the diffusion gradients, and

diffusion time and length, which is expressed by the b-value. Both together they form the so-called q-space. The propagator is related to the signal attenuation, that is, the quotient of the signals measured in presence of a diffusion gradient and without the influence of a gradient, via Fourier transform. Modeling the entire propagator, however, impossible in practice, since it would require infinitely dense sampling of the whole q-space ( $\mathbb{R}^3$ ) and the diffusion time. Therefore usually simple models are used for describing the propagator. This leads a reduction in necessary measurements due to certain modeling assumptions. In the simplest case one assumes anisotropic Gaussian diffusion, which leads to a diffusion propagator that can be approximately described by a tensor. This technique is called diffusion tensor imaging (DTI) (P J Basser et al., 1994a). Theoretically this approach is appropriate in situations with only one, approximately coherent, fiber population per voxel.

A different approach involves a less constrained reconstruction of the diffusion propagator. An approach which circumvents the limitation of having to sample the entire q-space was first introduced by Tuch (D. S. Tuch, 2004). He uses the Funk-Radon transform to only evaluate the marginal probability of the diffusion in a given direction, leading to the orientation profile of the diffusion propagator for a fixed, sufficiently high, b-value. This result is referred to as the diffusion orientation density function (dODF) or q-ball. It has recently been shown that the original dODF formulation by Tuch (D. S. Tuch, 2004) overvalues points which are located close to the origin, due to it using a linear radial projection. This has led to the introduction of more accurate dODFs by considering the properties of the spherical coordinate system (Aganj et al., 2010; Alan Barnett, 2009; Canales-Rodríguez et al., 2009; Tristán-Vega et al., 2009).

A model which is not based on the diffusion propagator is spherical deconvolution (D. C. Alexander, 2005a; Dell'Acqua et al., 2007; Kaden et al., 2007; Tournier et al., 2007, 2004). Here the signal is assumed as constituted by the convolution of the signal associated to a single fiber or group of coherently oriented fibers with a fiber ODF (fODF). This requires an estimate of the signal attenuation generated by a single fiber bundle, the so-called deconvolution kernel. In return this model gives fiber and not diffusion information.

Several more local models exist. The three models discussed above, however, are some of the most prevalent. Therefore in this thesis the focus is mainly on these models. For an overview over more local models see the work of Assemlal and colleagues (Assemlal et al., 2011).

All local models can be used to define metrics. These describe distances in a parameter space and are characterized by their specificity and sensitivity towards differences in the physical quantities they are meant to reflect. These metrics are used for inferring the microstructural information from the local model. The most widely used metric is fractional

anisotropy (FA) (P J Basser, 1995). It is based on the tensors geometry and describes the isotropy of the observed diffusion. While this metric is very sensitive to changes in the microstructure, it is not very specific towards the type of change observed. Although the limited amount of acquired data makes it impossible to achieve absolute specificity, the fact that the tensor represents only part of the available information in the data gives reason for hope that more specific metrics than FA might be possible. Such metrics should be designed to improve the situation in one of the following two ways: (1) They reproduce results which are also uncovered by FA, thus endowing them with additional meaning. In other words, the fact that a new metric shows the same differences as the FA may tell us something about the possible origin of the FA changes, thereby increasing specificity. (2) The metrics uncover microstructural changes, which are not seen in FA, thus increasing sensitivity. Since the FA is very sensitive but not very specific in its nature, one can expect to mostly encounter the former situation. Not many HARDI metrics are used in practice. Actually the most commonly used HARDI metric the generalized FA (GFA) has been shown to correlate linearly with the FA (Gorczewski et al., 2009). It therefore does not offer much more in terms of specificity.

The central question of this thesis can be formulated as: Can one meaningfully characterize the voxel-wise bundle microstructure in terms of metrics derived from HARDI measurements? For this we first have to ask ourselves: Can we identify the contribution of fiber bundles in each voxel separately? To answer this question several local models were investigated. However, since the fODF directly describes the microstructural arrangement it is a natural choice when trying to derive microstructural metrics. The fODF is usually represented as SH series expansion, which is difficult to interpret directly. The goal of this work was therefore to find a robust parameterization of the fODF, which identifies multiple compartments, each representing a relatively coherent fiber bundle described by a set of meaningful parameters, and to interpret these parameters, as far as possible, in terms of microstructural properties, increasing the specificity of the assertions made from changes in FA. For determining the bundles present within a voxel the criterion that each peak of the fODF is caused by a distinct bundle present within a voxel was chosen. Each of the peaks is then described using a Bingham distribution, as this has been shown to be an accurate description for coherent fiber bundles (Kaden et al., 2007; Kiran K Seunarine et al., 2007).

In this thesis I will introduce a Bingham fitting scheme which is able to characterize the peaks of the fODF. Then I introduce metrics based on the Bingham fit, which can be used for the characterization of microstructural properties. An application of the Bingham fit beyond the description of metrics is for the use in the reconstruction of fiber pathways from the local model (tractography), as the separation of the fODF into compartments allows deciding which population to follow more easily. Additionally I applied the Bingham fit to

fetal MRI data describing the microstructural development and introducing the Gini coefficient as novel metric for determining the developmental age of the brain.

## 1.2 Outline and Contributions

In Chapter 2 I start off by explaining the brains tissue composition and the anatomical position of some of the important fiber bundles. Afterwards I discuss the basics of MRI focusing especially on the physics behind MRI and dMRI, as for the interpretation of local models knowledge on what is measured is fundamental.

I discuss the math behind spherical harmonics (SH) in Chapter 3. This chapter covers the mathematical basis needed for two of the main local models (dODf and fODF). I derive the SH functions from Laplace's equation, define the spherical harmonic base and discuss the interpretation of the coefficients of the SH expansion. Afterwards I introduce the Funk-Hecke theorem and give the spherical convolution theorem. These are the basic tools needed for working with SH.

In Chapter 4 I introduce several local models. These are the diffusion tensor, the dODF and the fODF. Here I especially focus on the dODF and the fODF. Since the approach of calculating the dODF by Tuch (D. S. Tuch, 2004) uses a linear simplification, I discuss the methods by Aganj and colleagues (Aganj et al., 2009) as well as Tristan-Vega and colleagues (Tristán-Vega et al., 2009) and introduce a common framework for these two methods. Finally I discuss the fODF and the implications on the accuracy of the method from the use of the SH basis. I furthermore explore the correlation between the distribution of crossing angles derived from the fODF and the Dirac delta approximation of the SH expansion, showing a connection which might be used for detecting bias in the reconstructions.

In Chapter 5 I introduce the Bingham fitting scheme, for characterizing the peaks of the fODF. The idea is to use the fODF calculated via spherical deconvolution, since the fODF describes the fiber bundle configuration, as basis. This assumes the peaks of the fODF to reflect the underlying properties of one fiber bundle each. The fODF peaks are then approximated with Bingham functions. These are then used for the separate characterization of the fiber bundles present within a voxel. The Bingham functions and the fitting scheme introduced in this chapter form the foundation for most of the work done in this thesis.

Metrics derived from the Bingham fit are discussed in Chapter 6. In this chapter the Bingham fit is used to capture first and second order statistics of the fiber orientations, from which metrics for the parametric quantification of fiber bundles are derived. Furthermore meaningful relationships between these measures and the underlying microstructural

properties are proposed. The focus hereby lies on metrics derived directly from properties of the Bingham distribution, such as peak length, peak direction, peak spread, integral over the peak, as well as a metric derived from the comparison of the largest peaks, which probes the complexity of the underlying microstructure. These metrics are then compared to the conventionally used FA and show how they may help to increase the specificity of the characterization of microstructural properties.

Chapter 7 discusses a simple tractography method derived directly from the Bingham fit and the inversion of the convolution theorem. A Bingham fit is performed for each of the fiber populations present in a voxel. From the Bingham fit the diffusion signal and tensor are computed. Afterwards a tensor deflection tractography modified for multiple tensors per voxel is applied. This allows incorporating the complete bundle information, performing local interpolation as well as using multiple directions per voxel for generating tracts, thereby avoiding several of the problems arising when performing tractography directly on the basis of HARDI models.

Finally in Chapter 8 the Bingham metrics are applied to fetal dMRI data. Here for developmental landscapes from the tensor based metrics apparent diffusion coefficient (ADC) and FA as well as from the complexity (CX) are calculated. I then introduce the Gini coefficient as metric describing the homogeneity of the distribution of these values throughout the brain, giving an index for the developmental state of the brain. This is done on the assumption that the brain starts out very homogenous and becomes more inhomogeneous in its structure as it differentiates.

The important contributions of this thesis are the introduction of a method for characterizing the peaks of the fODF and the introduction of metrics derived from this characterization. The direct connection between fODF and microstructure enables specific metrics. Since the characterization of the fODF allows for the investigation of the fODF behavior in detail, I also uncovered some problems of the SH formulation of the fODF, which also translate to the dODF. I specifically examine the problem of spurious peaks and the connection to the Dirac delta function. Furthermore I propose a novel fODF based tractography approach and introduce a common framework to the dODF formulations of Tristan-Vega et al. (Tristán-Vega et al., 2009) and Aganj et al. (Aganj et al., 2009).

## 2 Background

---

### 2.1 Introduction

Gaining insight on the working of the human brain is a difficult task. To this day it remains unknown how information is carried through the brain and how different parts are connected. At microscopic scale the brain consist of over 15-33 billion neurons, which exchange electrical signal pulses (action potentials) along protoplasmic fibers called axons. The axons are often referred to as nerve fibers and form directionally aligned populations of axons, which are called fiber bundles.

Up to about 40 years ago, the only mean to access the brain's neural architecture for studying the anatomy involved dissection. With the advent of *magnet resonance imaging* (MRI) investigating the brain in-vivo became possible (Lauterbur, 1973; Mansfield, 1977). MRI uses the principles of *nuclear magnetic resonance* (NMR) (Bloch, 1946; Purcell et al., 1946; Rabi et al., 1938) to measure a signal from spinning nuclei, in case of MRI mostly hydrogen nuclei. In essence this is done by placing a patient inside a large magnet, aligning the spins of the hydrogen nuclei with the field and then using radio waves to excite the nuclei at their resonance frequency. This disturbs the equilibrium state of the nuclei. The

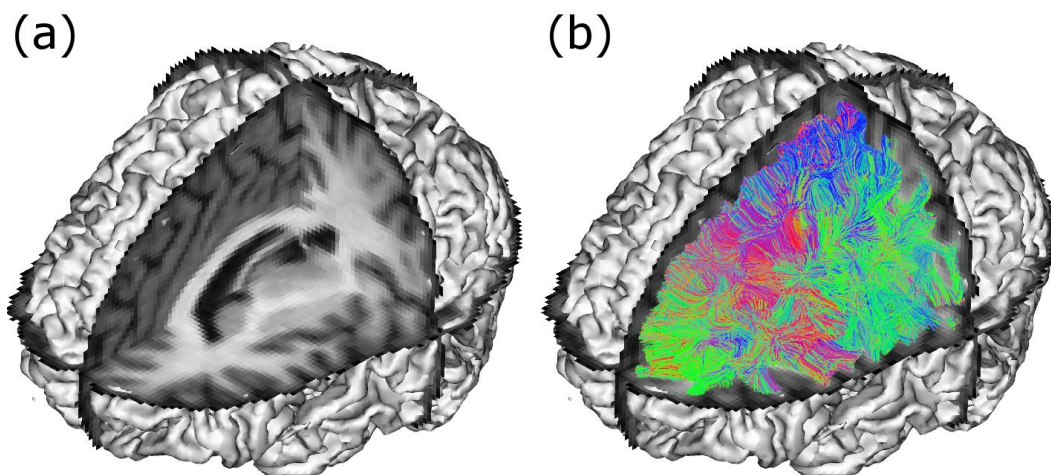


Figure 2.1: MRI images and fiber reconstruction. On the left a  $T_1$  image is shown (a). On the right the corresponding fiber reconstruction from dMRI is shown (b). Both images are visualized with an iso-surface calculated on the basis of the dMRI dataset.



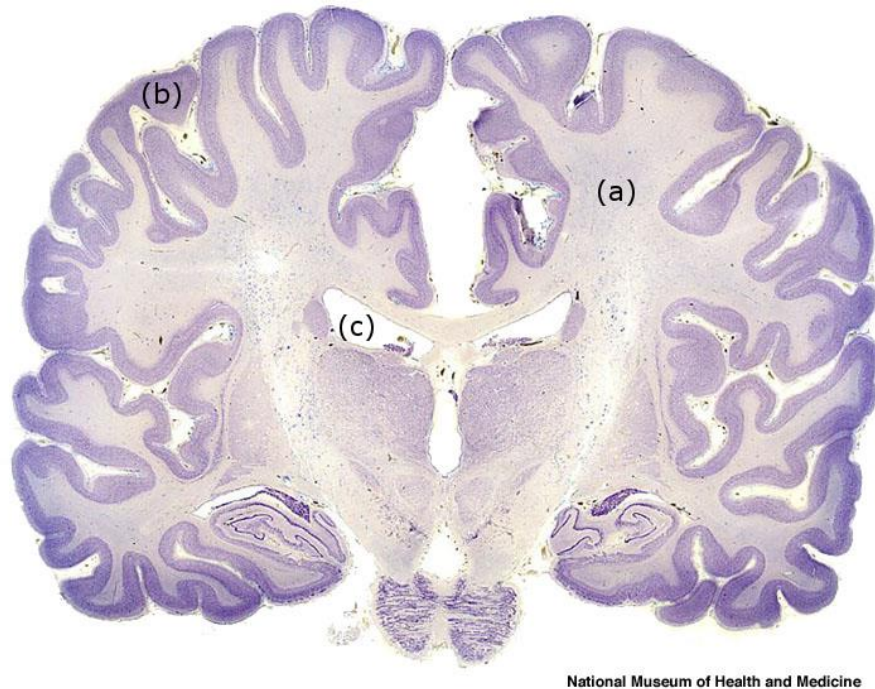


Figure 2.2: Full Brain. This image was taken from the brain museum ([www.brainmuseum.org](http://www.brainmuseum.org)). The image shows a coronal slice taken from a human specimen. One can clearly observe the white matter (a) and grey matter (b). As can be seen the grey matter area close to the surface (cortex) is darker, while the more central white matter areas are lighter. The areas marked as ventricles (c) are filled with CSF. The difference in composition of these types of tissue is the main cause for contrast in MRI.

return to the equilibrium state after applying the radio frequency pulse is referred to as relaxation and can be measured in terms of an electrical signal induced into a receiver coil. This signal is sensitive to different types of biological tissue, allowing us to probe the brain's anatomy in terms of tissue composition in-vivo. A typical MR image is shown in Figure 2.1.

In the middle of the 1980's *diffusion weighted MRI* (dMRI) was introduced (Bihan et al., 1986; Merboldt et al., 1985; Taylor and Bushell, 1985). Diffusion MRI is based on the spatial dislocation (diffusion) of water molecules due to their thermal energy propelled motion (Brownian motion) (Brown, 1827). It allows probing the microstructural organization of the fiber bundle layout, since coherent populations of nerve fibers reduce diffusion perpendicular to their orientation. In contrast to MRI, which probes tissue composition, dMRI probes tissue microstructure in terms of fiber arrangement. From the local fiber arrangement probed by dMRI long range connections can be calculated by means of tractography (shown in Figure 2.1), allowing to explore the connection between different areas of the brain.

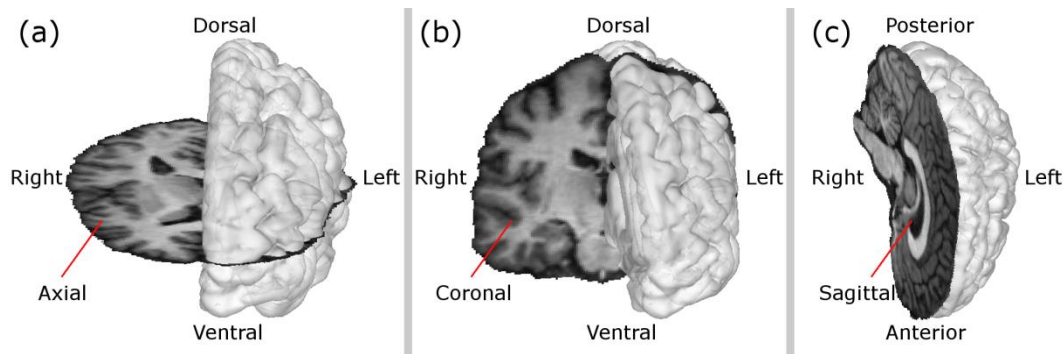


Figure 2.3: The anatomic reference planes. Images acquired in MRI are usually presented in terms of section on reference planes. In (a) the axial, in (b) the coronal and in (c) the sagittal reference plane is shown. Additionally the terminology used for describing directions is introduced.

In this chapter I will first discuss the composition of the brain's tissue to give some background on what causes the contrast in MRI. Then talk about the physics of MRI by explaining how NMR works. I will introduce the b-value,  $T_1$  and  $T_2$  weighting, as well as the standard MRI sequences. Then I will introduce dMRI. This chapter does not contain contributions from my part, but rather introduces the basics of the measurements, which are necessary for understanding the further work, since for interpretation of data and especially the introduction of metrics it is important to have a deep understanding of what actually is measured.

## 2.2 Brain Tissue

Visually the brain's interior can be divided into light areas, the so called white matter, and darker areas of so-called grey matter (see Figure 2.2). It is surrounded by *cerebrospinal fluid* (CSF). These three types of tissue and their differences in composition are the main influence for the contrast in MRI. The distinct coloring of the different areas is influenced by the cellular configuration of the tissue.

At cellular level the brain consists mainly of two types of cells, glia cells and neurons. Glia cells mainly function as physical support for the neurons (Jessen and Mirsky, 1980). Furthermore they supply nutrients and oxygen to neurons, insulate neurons from each other and play a role in the modulation of neurotransmission (Auld and Robitaille, 2003). The neurons transmit signals as electrical impulses to target cells over long distances. These signals are transmitted by the means of axons as electrochemical pulses (action potentials). Most space in the brain is occupied by axons, which are often covered in myelin sheaths.

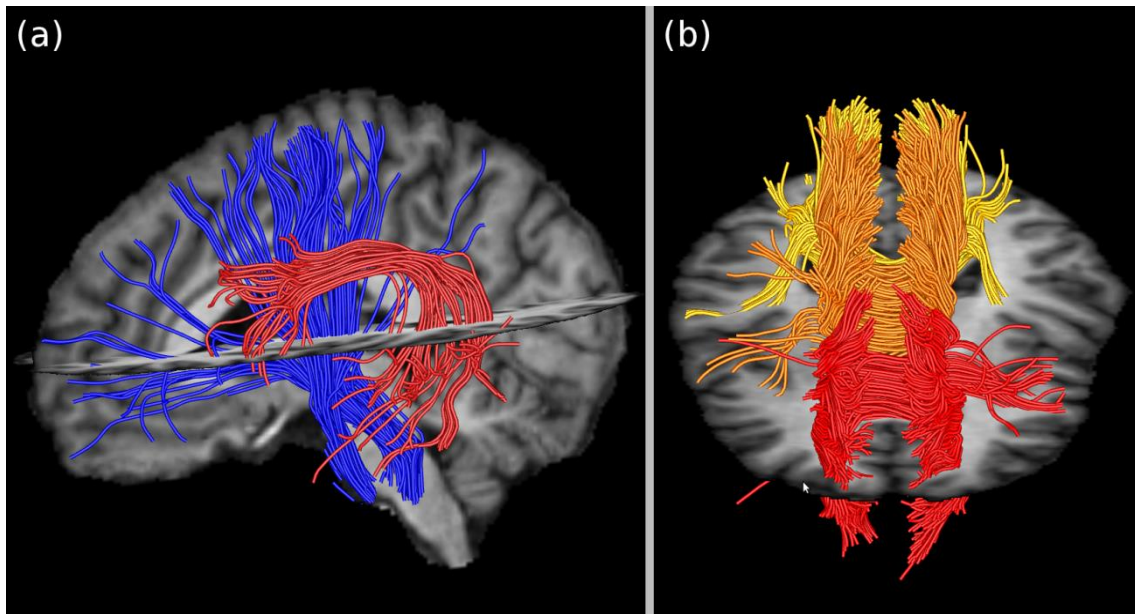


Figure 2.4: Significant fiber bundles. In this image some of the most significant fiber bundles, which are used in this thesis and their location in the brain are shown. On the left (a) the corticospinal tract (CST) is shown in blue, while the arcuate fasciculus (AF) is shown in red. On the right (b) the corpus callosum is depicted. It is divided into a frontal (red), medial (orange) and lateral (yellow) section.

This white substance serves to increase the speed of signal propagation. Due to the myelination, areas of the brain filled with lots of nerve fibers appear white, while areas with a high density of neuron cell bodies appear darker. This causes the visual divide of the brain's interior.

The most common way of viewing the brain is to use slices along anatomical reference planes. The three planes are axial, coronal and sagittal planes. They are shown in Figure 2.3.

The axons are often referred to as nerve fibers and form directionally aligned populations, which are called fiber bundles. The investigation of the fiber bundle arrangement is one of the main advances of dMRI. In this work I am looking to describe properties of fiber bundles in terms of the number of fibers involved, their configuration, their thickness, collinearity and spread. I am therefore very interested in the influence these bundles have on the observed signal in dMRI. The significant fiber bundles mentioned in this work are shown in Figure 2.4.

## 2.3 Physics of MRI

### 2.3.1 Spins and Magnetic Fields

The spin of a particle is a fundamental property of nature (Dirac, 1982). The protons and neutrons in every nucleus have a spin (angular momentum). If the total number of neutrons and protons in the nucleus is even, the spins cancel. In case of an uneven number, like for example in hydrogen, which only has a single proton, the proton's spin leads to the generation of a small magnetic field, since a moving electrically charged particle produces a magnetic field. The magnitude of the magnetic field depends on the amount of electrical charge and the speed at which the charged particle moves. Generally speaking the faster a particle moves and the larger the charge is, the larger the generated magnetic field is. In case of hydrogen the proton does not have a specifically large charge ( $1.6 \cdot 10^{-19} \text{ C}$ ) but moves very fast, leading to a small, but observable magnetic field. In the following when talking about nuclei I only refer to those with a non-zero spin, which therefore possess a small magnetic field, similar to a small bar magnet (as shown in Figure 2.5).

The physical basis for MRI is NMR. This physical phenomenon describes the behavior of nuclei in a constant magnetic field, which absorb and re-emit electromagnetic radiation. It was simultaneously described by Purcell (Purcell et al., 1946) and Bloch (Bloch, 1946). When applying a constant external magnetic field ( $B_0$ ) the magnetic fields of the nuclei align with the external magnetic field (see Figure 2.5). There are two states in which the nuclei's fields can align with the external field, a low-energy-state aligned with the direction of the external magnetic field (parallel) and a high-energy-state aligned against the direction (anti-parallel) of the external magnetic field. Both of these states are shown in Figure 2.6. The number of parallel aligned magnetic fields in relation to the anti-parallel aligned is governed by thermodynamic equilibrium and can be described by the Maxwell-Boltzmann distribution. On a more macroscopic scale this leads to a net magnetic field of a substrate, depending on the relation of the nuclei's magnetic fields in the two energy states. The net magnetic field is described by a vector, the net magnetization field vector. At room temperature a small excess number of the nuclei's magnetic fields will be aligned with the external magnetic field, therefore the net magnetic field vector is aligned with the external magnetic field. Due to their angular momentum the nuclei precess around the external field's direction, rather than completely aligning with (or against) the  $B_0$ -field. The frequency of precession is the so called Larmor frequency ( $\omega_L$ ), which is specific to each atomic nucleus. The Larmor frequency is proportional to the external magnetic field's strength and depends on the nucleus's charge ( $q$ ), mass ( $m$ ) and the so called gyromagnetic factor ( $g$ ), which describes the relation between the nucleus's magnetic dipole momentum and its spin:

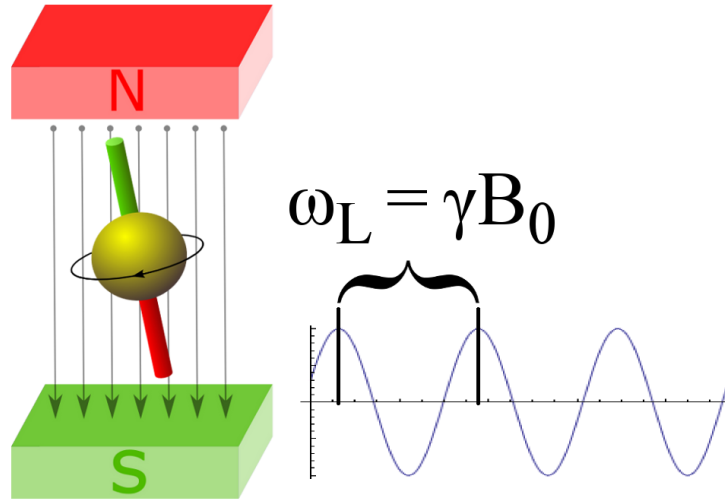


Figure 2.5: Spins in a magnetic field. In a magnetic field, nuclei (which due to their spin act as small magnets) align with the external field's axis. They hereby precess around the field's axis. This precession is similar to the precession of a gyroscope. It is characterized by its frequency and its phase. The frequency defines how fast a spin is rotating and the phase defines the current position of rotation. The frequency of precession is called the Larmor frequency  $\omega_L$  and depends on the external  $B_0$  field's strength, as well as the nuclei specific gyromagnetic ratio.

$$\omega_L = g \frac{q}{2m} B_0 = \gamma B_0. \quad (2.1)$$

The quantity  $\gamma = g \frac{q}{2m}$  is referred to as the gyromagnetic ratio. The Larmor frequency usually lies in the radio frequency (RF) range of the electromagnetic spectrum.

It should be pointed out, that even though the individual magnetic fields precess around the  $B_0$ -field's direction, the net magnet field does not naturally precess. This is due to the precession of the individual nuclei being out of phase and therefore canceling.

In order for a nucleus to absorb energy, it has to be excited, such that it switches from the low-energy state to the high-energy state. The energy difference between these two and therefore the energy needed to switch from the lower to the higher energy state is equal to:

$$\Delta E = \hbar \frac{\omega_L}{2\pi}, \quad (2.2)$$

where  $\hbar$  stands for Planck's constant. If one applies an electromagnetic RF-pulse with energy  $\Delta E$  at their Larmor frequency to the particles in the external magnetic field, they start to resonate. This causes nuclei in the low energy state to absorb energy, bringing them

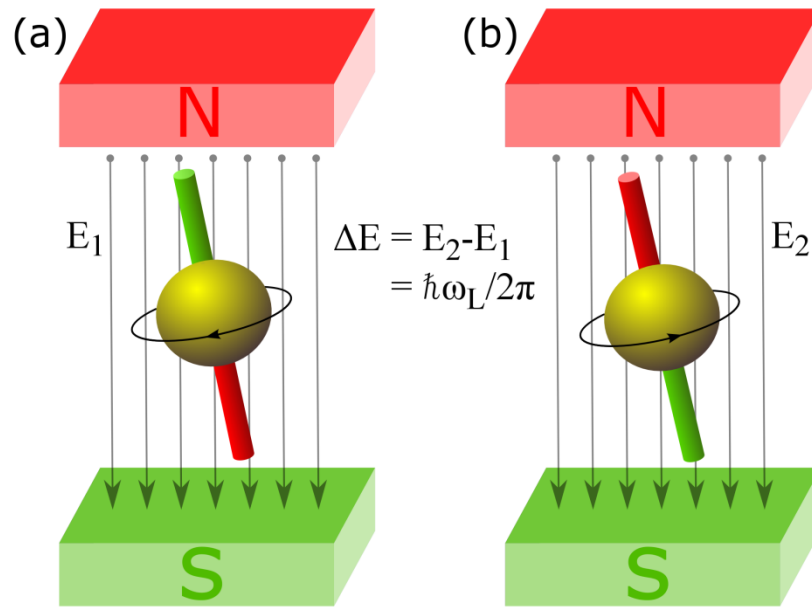


Figure 2.6: The two energy states. The two energy states a nucleus can take are a low energy state (parallel) shown in (a) and a high energy state (anti-parallel) shown in (b). The difference in energy states is  $\Delta E = E_2 - E_1 = \hbar\omega_L/2\pi$ . Due to thermal effects, a slightly higher number of nuclei are in parallel than in anti-parallel alignment with the external field. This leads to an excess magnetization of a substance in the magnetic field in alignment with the orientation of the  $B_0$ -field. This is also referred to as net-magnetization.

to the higher energy state. This rotates their magnetic field to align anti-parallel to the external field. In addition the phases of the precessing nuclei synchronize, which causes the net magnetization vector to rotate away from the  $B_0$ -field direction and to start precessing at the nuclei's Larmor frequency. The amount of rotation is dependent on the strength and duration of the RF-pulse. The RF-pulses are usually classified by the rotation they induce on the net magnetization vector. The two most important pulses are the  $90^\circ$  RF-pulse and the  $180^\circ$  RF-pulse. The frequency spectrum of the RF-pulse determines the spatial extension and the homogeneity of the nuclei for which the net magnetization is influenced.

After stopping to apply the RF-pulse two phenomena can be observed. First the spins start to return to an energy state distribution governed by thermodynamic equilibrium as before applying the RF-pulse ( $T_1$ -relaxation). Second the spins which were brought into phase by the RF-pulse start dephasing ( $T_2$ -relaxation). For a more detailed description of these phenomena, which cause the net magnetization vector to return into alignment with the  $B_0$  field, I will view the net magnetization vector as composed of two vector components, one longitudinal magnetization vector ( $M_z$ ) in direction of the  $B_0$ -field and an orthogonal transversal magnetization vector ( $M_T$ ). In the terms of these two vectors  $T_1$ -relaxation

describes the change in net longitudinal magnetization, while  $T_2$ -relaxation describes the change in transversal magnetization.

### 2.3.2 $T_1$ -relaxation

The shift from the lower energy state to the higher energy state, caused by the RF-pulse, leads to some of the nuclei's magnetic fields switching from parallel to anti-parallel alignment with the external field. This decreases the net magnetization in longitudinal direction. After stopping to apply the RF-pulse, the net magnetization in  $B_0$ -field direction can be observed to increase again. This is due to nuclei dissipating excess energy in terms of heat to their environment (in solids this environment is called lattice), returning the relation between parallel and anti-parallel aligned nuclei to the thermal equilibrium. This process depends on the difference between the current state and the thermal equilibrium state. It therefore can be described by an exponential. The relaxation process is referred to as spin-lattice relaxation. The time  $T_1$  characterizes the rate at which the net magnetization vector recovers towards alignment with the external field, it thereby describes the average time a nuclei remains in the high energy state. The recovery of the longitudinal magnetization is exponential and can be described by:

$$M_z = M_{z(eq)} \left( 1 - \exp\left(-\frac{t}{T_1}\right) \right), \quad (2.3)$$

where  $M_{z(eq)}$  describes the magnetization vector's z-component at equilibrium. From this one can see that the longitudinal magnetization is recovered to about 63% of the equilibrium value after time  $T_1$  and that it takes about  $5 \cdot T_1$  to recover to 99% of the equilibrium. The value for  $T_1$  is dependent on the nuclei and its gyromagnetic ratio and furthermore the lattice's mobility. The recovery rate is therefore dependent on the spin's environment. In case of biological tissue this implies a dependence on the local properties of the tissue.

The time  $T_1$  depends on the magnetic field strength. The higher the external  $B_0$ -field strength is, the higher the relaxation time gets. This is due to higher Larmor frequencies being needed at higher field strength, which reduces the spectral densities at the Larmor frequency. This causes fewer nuclei to be excited and therefore the number of nuclei which are able to transfer energy to the lattice are reduced.



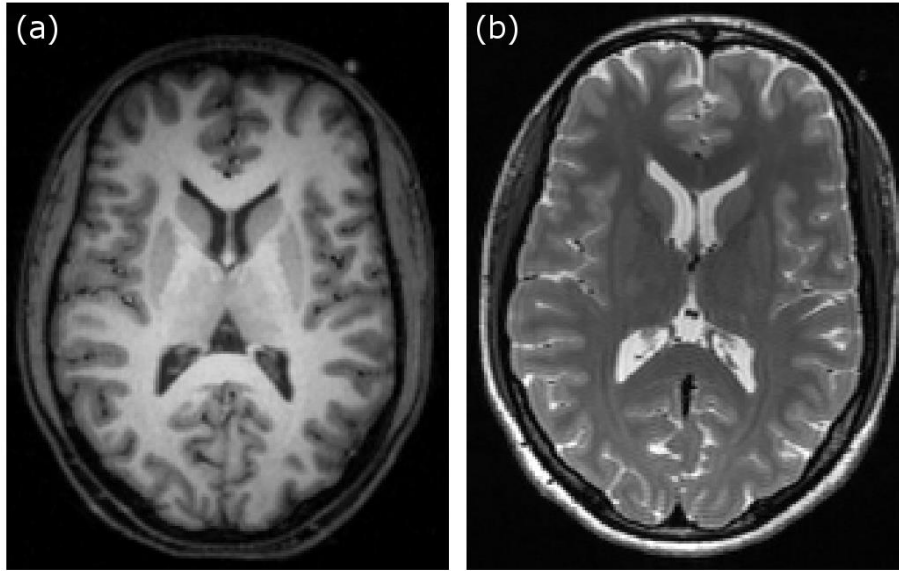


Figure 2.7: Axial view of a  $T_1$  and a  $T_2$  image. The composition of the tissue is the source for the contrast in MRI. In (a) the light areas correspond to white matter areas. The grey areas show the grey matter, while the CSF shows no signal and is therefore dark. In (b) the dark areas correspond to white matter areas. The light areas show the grey matter, while the CSF shows a high signal and therefore is white.

The net magnetization in longitudinal direction is several magnitudes smaller than the strength of the external  $B_0$ -field. It therefore is difficult to measure directly (Kelso et al., 2009). If the longitudinal magnetization, however, is rotated orthogonal to the main magnetic field, then the net magnetization starts precessing around the main direction. This precession induces a free-induction-decay (FID) signal, which can be measured by a receiver coil in terms of an electrical signal. For this a  $180^\circ$  RF-Pulse is applied, which allows longitudinal relaxation to occur during a recovery time and then a  $90^\circ$  RF-pulse is applied, which rotates  $M_z$  in the xy-plane orthogonal to the external field. This process is called inversion recovery. The amplitude of  $M_z$  is then measured in terms of the induced electrical current from the receiver coil.

The  $T_1$  values vary between different types of tissues. In case of a long  $T_1$  time of the tissue a small signal-amplitude is measured, while a short  $T_1$  time causes observing a large signal-amplitude. The recovery time is chosen in order to maximize the contrast between the observed signals. In praxis one wants a short recovery time, as the longer one waits, the smaller the contrast is.

In a  $T_1$  weighted image the axons and nerve connections in the white matter give a high signal, while the grey matter gives a medium signal. Nearly no signal can be observed in the



areas of CSF. Therefore the white matter appears white in a  $T_1$ -image, while grey matter appears grey and the CSF appears dark (as can be seen in Figure 2.7).

### 2.3.3 $T_2$ -relaxation

Applying the RF-pulse causes the nuclei in a sample to precess in phase. This generates a magnetic field rotating at the nuclei's Larmor frequency. This can be described in terms of a rotating transversal component of the net magnetization vector. As soon as the application of the RF-pulse ends, the nuclei begin to dephase. This happens as the spins interact with the neighboring spins influencing each other's rotation speed and leads to decay of the induced magnetic field and therefore of the net-magnetization-vector's transversal component. This effect is known as  $T_2$  relaxation or spin-spin relaxation. In terms of the transversal magnetization it can be described as:

$$M_T = M_{T(eq)} \exp\left(-\frac{t}{T_2}\right). \quad (2.4)$$

As the  $T_2$  relaxation is caused mainly by the interaction of neighboring spins,  $T_2$  is higher in neighborhoods where a lot of spins are present. In case of biological tissue the main source of spins are protons in the hydrogen of water. Macromolecular environments therefore display shorter spin-spin relaxation times while water based fluids carry higher  $T_2$  values. It should be noted, that the  $T_2$  decay is completely independent of the  $B_0$  field and only depends on the spin-spin interactions.

Measuring a  $T_2$  weighted signal is relatively straightforward. A  $90^\circ$  RF-pulse is applied. This causes an observable transversal magnetization. This signal is measured after a time  $TE$  during which the spins start dephasing. Again  $TE$  controls the contrast between tissues with a longer or a shorter relaxation time. In contrast to measuring  $T_1$  a large signal corresponds to a high  $T_2$  relaxation time, while a small signal corresponds to low  $T_2$  relaxation time. In practice, one wants a large time  $TE$  for observing a large contrast between areas with different  $T_2$  times.

In theory the signal decay only depends on the spin-spin interactions. Imperfections in  $B_0$ -field, chemical shifts, and differences in magnetic susceptibility as well as tissue boundaries can lead to signal decay which is faster than  $T_2$ . This smaller relaxation time is referred to as  $T_2^*$  and can be seen as the superposition of  $T_2$  with a fixed  $T_2^f$ :

$$\frac{1}{T_2^*} = \frac{1}{T_2} + \frac{1}{T_2^f}. \quad (2.5)$$

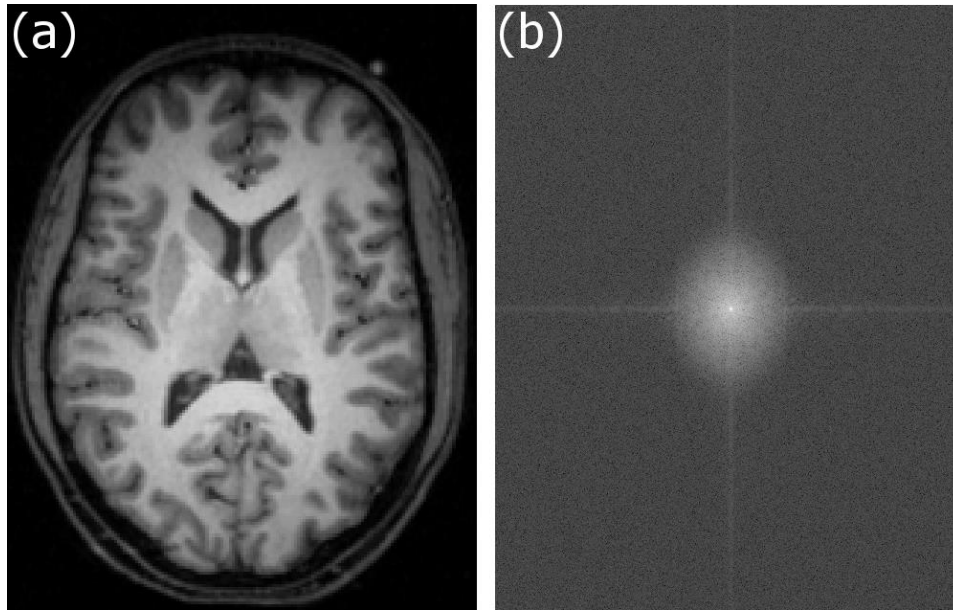


Figure 2.8: Connection between k-space and MR image. In (a) the k-space image, which was read line wise, is shown. In (b) the resulting MR image is shown. The connection between the two images is the 2D-Fourier transform.

In order to preserve the MR signal and increase the  $T_2$  contrast it is desirable to reduce the influence of the fixed  $T_2^f$  and thereby reduce the difference between  $T_2$  and  $T_2^*$ . As mentioned before, after applying a  $90^\circ$  RF pulse, nuclei that were in phase begin to dephase in the xy-plane. If a  $180^\circ$  RF pulse is applied after a certain time, the nuclei's spins will rotate over to the opposite axis. This pulse will cause these spins to start rephasing, reach alignment, forming a maximal signal, before starting to dephase again. The rephasing will cause a so called spin echo. Now another  $180^\circ$  RF pulse can be applied. The  $T_2$  relaxation curve covers the signal peaks caused by spin echo. The cause of this is described in the work of Pooley (Pooley, 2005).

The contrast between the three main types of tissue in the human brain is inverse in  $T_2$  compared to  $T_1$  measurements. In  $T_2$  weighted images, the white matter appears dark, due to a low signal, while the grey matter and especially the CSF provide a high signal and appear very bright. The difference between the two types of images is the sensitivity to different aspects of tissue. They therefore display different types of contrast and uncover different aspects of tissue composition (see Figure 2.7).

## 2.3.4 MRI Measurements

If one investigates biological tissue the spatial positions at which one measure the relaxation are of great interest for investigating the spatial arrangement. For this a process called spatial encoding is used. The spatial encoding is performed by using spatial gradient fields. These superimpose three fields, one for each x-, y- and z-direction, thereby encoding the positions within the sample in terms of x-, y- and z-coordinates. These gradient fields provide a discretization of the measured signal, leading to the signal within a small volume element being measured. This volume element is referred to as voxel. The basic idea behind spatial encoding is to vary the field dependant Larmor frequencies of the excited nuclei, thereby encoding their position.

The gradient in z-direction is usually referred to as the slice selection gradient, as it selects the plane in which the image is taken. A gradient varying along the z-axis, which is along the direction of the external field, is applied, while administering the RF-pulse. As the Larmor frequency varies with the field strength, only nuclei in the slice targeted by the RF-pulse are excited. It should be noted that the slice selection has to be completed before subsequent spatial encoding magnetic field gradients can be applied. The thickness of the selected slice depends on the bandwidth of the RF-pulse used for exciting the nuclei and the slope and thereby the strength of the slice selection gradient.

The gradient in x-direction is called the frequency encoding gradient. It is applied left to right for spatial encoding in x-direction. It influences the Larmor frequencies and is applied during the recording phase of the signal acquisition. It causes the frequency of the measured signal to vary in x-direction. After measuring one can use Fourier analysis to determine the frequency, which then translates to the x-position of the measured signal. As the frequency encoding gradient changes the Larmor frequency, it also causes dephasing of the spins. As a result the signal decays faster.

For determining the y-position a gradient is used, which modifies the phase of the spin in y-direction. When the phase shift gradient is turned on, the nuclei spin faster or slower than their Larmor frequency. After the y-gradient is switched off, they return to their initial Larmor frequency, however their phase remains unchanged. The position in y-direction can then be determined by Fourier analysis of the measured signal, as the y-position corresponds with the phase. The application of all of the gradient pulses is shown in Figure 2.10.

The slice-wise measurements are stored in k-space, which is also referred to as the raw-signal space. It is the 2-dimensional space of frequency and phase. The columns in k-space correspond to different frequencies, while the rows correspond to different phases. The

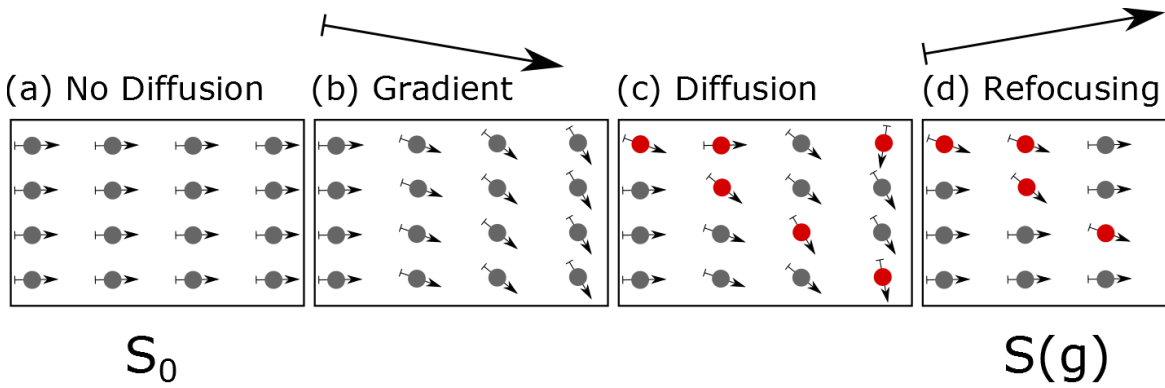


Figure 2.9: The diffusion encoding process. In this image the influence of the diffusion gradient on the phase of the spins is visualized. After the application of the RF pulse the spins are all in phase (a). Here the signal  $S_0$  can be observed. In (b) the application of the diffusion gradient can be seen. The spins now possess a spatially varying phase. Due to diffusion the spins randomly displace, which causes the phase to lose its spatial connection (c). Afterwards a refocusing gradient is applied (d), which is the inverse of the gradient which was applied before. This should cause the spins to return to phase coherence. The diffusion has caused phase incoherence, which manifests in a signal  $S(g)$  that is smaller than the signal at phase coherence.

value at each point corresponds to the amplitude of the observed signal. The MR image is created from k-space via 2D-Fourier transform. This connection is visualized in Figure 2.8. For each slice a separate k-space image is created.

### 2.3.5 Diffusion MRI

Diffusion MRI is based on the spatial dislocation of water molecules. Propelled by thermal energy water molecules freely move in an isotropic medium. The movement of a single particle appears random as its direction changes by the constant collision with other particles (Einstein, 1956). This random movement is referred to as Brownian motion (Brown, 1827). On a larger scale this movement leads to a so called diffusion process (Fick, 1855). Diffusion itself is a bulk-motion-free transport phenomenon which results in molecule or particle mixing. Within biological tissues this process is hindered by the microstructural boundaries of the tissue (P J Bassar, 1995). From the measurement of the influence of the tissue on the diffusion one can then infer the microstructural arrangement.

Observing the diffusion process is done by exploiting the electromagnetic properties of hydrogen nuclei (protons) in water molecules. When applying a magnetic field to biological tissue the nuclei's spins align themselves with the magnetic field, precessing about the field direction. In dMRI one observes the dephasing of spins of hydrogen nuclei in the presence of a directional, spatially-varying magnetic field (diffusion gradient field) by observing the

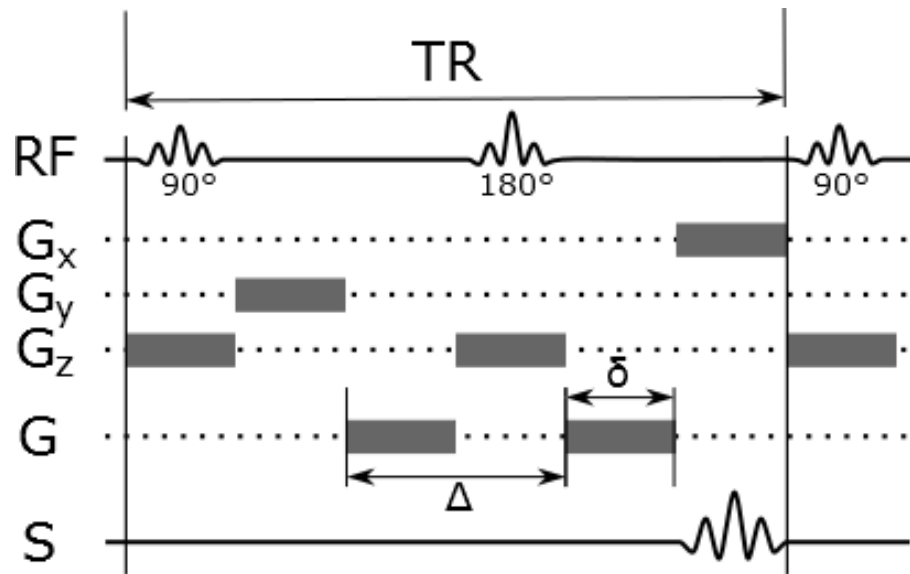


Figure 2.10: The Stejskal-Tanner pulse gradient echo diffusion sequence. This image show the application of different gradients, the RF pulses as well as the signal readout over time. The type of gradient is marked on the left. The letters  $G_x$ ,  $G_y$  and  $G_z$  mark the encoding gradients for the respective spatial direction,  $G$  marks the diffusion gradient. At the top the repetition time (TR) is shown. The gradient length  $\delta$  and the time  $\Delta$  during which the particles diffuse are marked as well.

amount of signal loss due to diffusion effects (Bihan et al., 1986; Stejskal, 1965; Taylor and Bushell, 1985). These measurements are applied to an array of diffusion gradient direction, which are usually distributed on a half sphere. This gives the hindrance of diffusion in terms of a reduced signal for each of the observed gradients, thus indirectly creating a directional profile of diffusion, which can be put into microstructural context using a local model.

For measuring diffusion a so called diffusion gradient is applied. Movement along the applied gradient field leads to a change of the corresponding Larmor frequency, which in turn leads to a phase change. The longer the water molecules can diffuse, i.e. the higher the diffusion time  $\Delta$  is, the more they will distribute over different distances, which leads to higher phase dispersion and in turn to a loss of signal coherence and therefore a reduction of the measured signal amplitude after applying a refocusing pulse, which is opposite to the diffusion-gradient. This diffusion encoding process is shown in Figure 2.9. The quotient of the signal without diffusion encoding and signal in presence of a diffusion gradient is called the signal attenuation and characterizes the portion of dephasing caused by displacement. As this influences the phase coherence of the spins, this effect affects  $T_2$  relaxation times and is observed by  $T_2$  measurements.

The diffusion encoding happens in three steps. The spins in the magnetic field are subjected to the spatially varying diffusion gradient pulse. This step is also known as diffusion weighting. Afterwards the magnetization is flipped by applying a  $90^\circ$  RF-pulse. Then the gradient pulse is applied again. Since the magnetization had been flipped in between, in case of no diffusion the same signal as without applying gradients is measured. However, due to Brownian motion the spins undergo different phase shifts by the spatially varied gradient pulse in the time  $\Delta$  lying between application of the first and second pulse. This pulse-sequence which is known as Stejskal-Tanner sequence (Stejskal, 1965) is shown in Figure 2.10. The dephasing leads to a drop in  $T_2$  signal attenuation, which is defined as the quotient of the signal  $S(t, \vec{q})$  to which a gradient  $\vec{q}$  was applied and the signal  $S_0(t)$  measured without application of a gradient field. One can assume the signal  $S_0(t)$  to be approximately free of diffusion effects. The quotient therefore eliminates the effects of relaxation and the attenuation signal can then be related to the diffusion in the corresponding gradient direction. The relation between signals and diffusion is discussed in depth in Chapter 4 (Local Modeling). The number of diffusion gradients defines the angular resolution of the dMRI measurement. For simple local models as few as 6 gradient directions are sufficient (Pierpaoli et al., 1996). In *high angular resolution diffusion imaging* (HARDI) a large number of gradients (more than 40) are used to acquire more information on the diffusion profile. One of the assumptions required in dMRI is that negligible diffusion occurs during the application of the gradient pulse. This assumption is also called the narrow pulse approximation.

## 2.4 Conclusions

In this chapter I first discussed the composition of the brain in terms of its microstructure. I then introduced MRI as well as dMRI. For this I discussed the physical principles of NMR and the phenomena  $T_1$  and  $T_2$  relaxation and the sequences necessary for measuring the changes in magnetization in terms of an electrical signal. I introduced diffusion and the diffusion weighting in terms of a diffusion gradient as well as defined signal attenuation. These are the basics of measuring one has to know, in order to understand how to model the microstructural influence on the diffusion signal. I did not yet give the connection between the measured diffusion signal and the microstructural arrangement, but will do so in depth in Chapter 4 (Local Modeling).

# 3 Spherical Harmonics

---

## 3.1 Introduction

In dMRI one acquires positive, antipodal symmetrical signal data sampled at discrete points on the sphere. From this data one estimates local models describing the influence of the tissue microstructure on the signal. As these local models and the data lives on the sphere it is desirable to describe it using a representation in terms of analytical functions. One of the most straightforward ways to achieve this is by the means of *spherical harmonic* (SH) expansion, which is the approximation of the function using a sum of coefficients and SH base functions.

The SH functions are the solution to Laplace's equation in spherical coordinates. They form an orthonormal base. Spherical deconvolution and q-ball, two of the main local models used in dMRI, are usually represented using a SH expansion.

In this chapter I will discuss the derivation of SH from Laplace's equation. I introduce the SH base, the SH expansion and the spherical convolution theorem, that the spherical deconvolution method is based upon. Additionally I introduce the spherical sampling theorem and the Funk-Hecke theorem, which are necessary as well in spherical deconvolution, as in the calculation of the q-ball.

I discuss the meaning of the first SH expansion coefficient and prove the connection to the integral of the expanded function over the sphere. This is a small and simple result which seems genuine to the field of neuroscience.

## 3.2 Laplace's Equation

Laplace's equation is one of the simplest second-order *partial differential equations* (PDE). It can be found in many physical problems such as fluid flow and electrostatics. Using the Laplace operator ( $\Delta$ ) it can be written as:

$$\Delta^2\psi = 0. \tag{3.1}$$

In three dimensions this leads to the following. Let  $\psi: \mathbb{C}^3 \mapsto \mathbb{C}$  be a twice differentiable function of the variables  $x$ ,  $y$  and  $z$ . Then Laplace's equation can be written as:

$$\frac{\partial^2}{\partial x^2}\psi + \frac{\partial^2}{\partial y^2}\psi + \frac{\partial^2}{\partial z^2}\psi = 0 \quad (3.2)$$

The solutions of Laplace's equation follow the principle of superposition, which states that if two functions are the solution to Laplace's equation, their sum is also a solution. Since one is dealing with discrete samplings of spherical data in HARDI, one needs to use Laplace's equation in spherical coordinates  $(r, \theta, \phi)$  with  $\theta \in [0, \pi]$ ,  $\phi \in [0, 2\pi]$ , which amounts to:

$$\frac{1}{r^2} \frac{\partial}{\partial r} \left( r^2 \frac{\partial \psi}{\partial r} \right) + \frac{1}{r^2 \sin^2 \theta} \frac{\partial^2 \psi}{\partial \phi^2} + \frac{1}{r^2 \sin \theta} \frac{\partial}{\partial \theta} \left( \sin \theta \frac{\partial \psi}{\partial \theta} \right) = 0. \quad (3.3)$$

This PDE can be solved by separation of variables in a radial, azimuthal and zenithal portion:

$$\psi(r, \theta, \phi) = R(r)\Phi(\phi)\Theta(\theta). \quad (3.4)$$

The solutions to Laplace's equation are called harmonic functions. They are analytic in the domain in which the equation is specified. In case of the functions being the solution to Laplace's equation in spherical coordinates the solutions are referred to as SH functions.

The radius independent part of equation (3.4) is referred to as the Laplace-Beltrami operator. It is defined as:

$$\Delta_b = \frac{1}{\sin^2 \theta} \frac{\partial^2 \psi}{\partial \phi^2} + \frac{1}{\sin \theta} \frac{\partial}{\partial \theta} \left( \sin \theta \frac{\partial \psi}{\partial \theta} \right) \quad (3.5)$$

and satisfies the relation:

$$\Delta_b Y_l^m(\theta, \phi) = -l(l+1)Y_l^m(\theta, \phi). \quad (3.6)$$

This relationship is especially interesting for the purpose of regularization. For example Descoteaux and colleagues proposed a Laplace-Beltrami regularization in their analytical q-ball calculation approach (Descoteaux et al., 2007).

### 3.3 Spherical Harmonic Functions

Using the separation of variables discussed in the previous section and assuming constant radius, which is reasonable in case of single shell (single b-value) HARDI acquisitions, one can derive a solution to Laplace's equation in spherical coordinates. The solution of Laplace's equation in spherical coordinates is as follows:



$$\psi(\theta, \phi) = \sum_{l=0}^{\infty} \sum_{m=-l}^l c_l^m P_l^m(\cos \theta) \exp(im\phi), \quad (3.7)$$

where  $P_l^m$  stands for the associated Legendre polynomial of order  $l$  and degree  $m$ . For in-depth derivation of the solution see the work of Descoteaux (Descoteaux, 2010). The associated Legendre polynomials used in the solution to Laplace's equation are defined as:

$$P_l^m(x) = \frac{(-1)^m}{2^l l!} (1-x^2)^{\frac{m}{2}} \frac{d^{m+l}}{dx^{m+l}} (x^2-1)^l. \quad (3.8)$$

The summands of equation (3.7) which are multiplied by coefficients  $c_l^m$  are called spherical harmonics (SH). This gives the definition of SH as:

$$Y_l^m(\theta, \phi) = P_l^m(\cos \theta) \exp(im\phi) \quad (3.9)$$

These functions are orthogonal with respect to the inner product. In many cases it is desirable to have an orthonormal set of function. This can be achieved by a normalization term which fulfills:

$$\langle Y_{l_1}^{m_1}(\theta, \phi), Y_{l_2}^{m_2}(\theta, \phi) \rangle = \int_{\Omega} Y_{l_1}^{m_1}(\theta, \phi) \bar{Y}_{l_2}^{m_2}(\theta, \phi) d\Omega, \quad (3.10)$$

In conjunction with the normalization term the SH functions are referred to as SH base functions. For rank  $m$  and order  $l$  they are defined as:

$$Y_l^m(\theta, \phi) = \sqrt{\frac{2l+1}{4\pi} \frac{(l-m)!}{(l+m)!}} P_l^m(\cos \theta) \exp(im\phi). \quad (3.11)$$

Several normalizations are in use for the SH functions. The particular SH base functions used here have been proposed by Descoteaux and colleagues (Descoteaux, 2010), which is the same version as commonly used in physics and seismology.

### 3.4 Spherical Harmonic Expansion

The SH base functions can be used to describe any complex function on the sphere, analogously to sines and cosines in the Fourier series expansion. This process is called SH expansion. In the case of diffusion measurements, values distributed on the surface of the sphere, describing the signal attenuation caused by the diffusion of water molecules are measured. These HARDI signal values are by definition real and antipodally symmetric. One can therefore simplify the defined SH base functions for the purpose of describing the

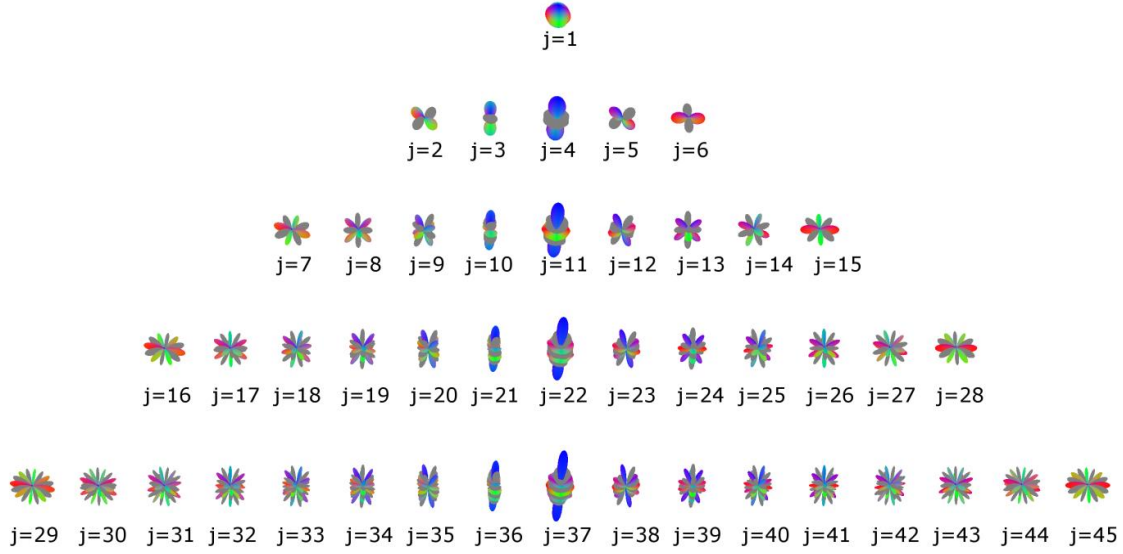


Figure 3.1: The SH base functions. Here glyphs of the SH base functions are shown for orders  $l = 0, 2, 4, 6$ . Negative function values are indicated in grey and positive values in color, indicating direction.

attenuation. The SH base functions have the property that even order harmonics are antipodally symmetric, while odd orders are antipodally anti-symmetric. The symmetry behavior can be described as:

$$Y_l^m(\pi - \theta, \phi - \pi) = \begin{cases} Y_l^m(\theta, \phi), & \text{if } l \text{ is even} \\ -Y_l^m(\theta, \phi), & \text{if } l \text{ is odd} \end{cases} \quad (3.12)$$

For describing the symmetric HARDI signals, one only needs to take into account even orders. In addition one only has to take into account the real part or the complex part of the SH functions, depending on the order. This can be summarized in terms of a modified SH base. Using the index  $j = \frac{1}{2}(l^2 + l + 2) + m$ . This base can be written as (Descoteaux, 2010):

$$Y_j(\theta, \phi) = \begin{cases} \text{Re}(Y_l^{|m|}(\theta, \phi)), & \text{if } m < 0 \\ Y_l^m(\theta, \phi), & \text{if } m = 0 \\ \text{Im}(Y_l^m(\theta, \phi)), & \text{if } m > 0 \end{cases} \quad (3.13)$$

Again there are several possibilities of defining the SH. In this work I use the formulation given by Descoteaux and colleagues (Descoteaux, 2010). The base functions are shown in Figure 3.1.

Using these base functions one can describe a function  $f(\theta, \phi)$  in terms of a SH expansion. This is defined as:

$$f(\theta, \phi) = \sum_{j=1}^{\infty} c_j Y_j(\theta, \phi), \quad (3.14)$$

The coefficients are defined as:

$$c_j = \int_0^{2\pi} \int_0^{\pi} f(\theta, \phi) Y_j(\theta, \phi) \sin(\theta) d\theta d\phi. \quad (3.15)$$

Due to the orthonormality of the SH base functions this can be understood as forming the inner product between the function  $f(\theta, \phi)$  and the SH. Thus the coefficient  $c_j$  can be determined by calculation of:

$$c_j = \langle f(\theta, \phi), Y_j(\theta, \phi) \rangle. \quad (3.16)$$

When applying the SH expansion to dMRI data one does not have an analytical representation of the function  $f(\theta, \phi)$  but rather a discrete representation in terms of a HARDI attenuation signal, which is observed at a set of  $N$  discrete diffusion encoding directions. Thus only a truncated spherical harmonic expansion can be determined. This expansion then smoothly interpolates between the observations. Let  $E$  be the attenuation signal estimated at the points  $(\theta_i, \phi_i)$ , then the discrete SH expansion can be formulated as:

$$E(\theta_i, \phi_i) = \sum_{j=1}^R c_j Y_j(\theta_i, \phi_i). \quad (3.17)$$

The order of the expansion is determined by the maximum order  $L$  that can be found in the definition of the SH function  $Y_j$ . The upper limit of the summation is then given by the term:

$$R = (L + 1)(L + 2)/2, \quad (3.18)$$

which also determines the minimum number of observation points for an expansion of order  $L$ . It should be pointed out that the restriction of the expansion to a finite number of summands can lead to the result taking positive and negative values due to the oscillating nature of the base functions.

As shown in the work of Descoteaux (Descoteaux, 2010), the coefficients of the discrete SH expansion can be calculated from an over-determined linear system using the coefficient

vector ( $\vec{c} = (c_1, \dots, c_R)^T$ ), the attenuation signal vector ( $\vec{E} = (E(\theta_1, \phi_1), \dots, E(\theta_N, \phi_N))^T$ ) and the matrix  $B$  containing the modified SH base:

$$\vec{E} = B\vec{c}. \quad (3.19)$$

The matrix  $B$  containing the modified SH base is an  $(N \times R)$ -dimensional matrix defined as follows:

$$B = \begin{pmatrix} Y_1(\theta_1, \phi_1), & Y_2(\theta_1, \phi_1), & \dots & Y_R(\theta_1, \phi_1) \\ \vdots & & \ddots & \vdots \\ Y_1(\theta_N, \phi_N), & Y_2(\theta_N, \phi_N), & \dots & Y_R(\theta_N, \phi_N) \end{pmatrix} \quad (3.20)$$

Solving the linear system can then be done in least square sense by using the Moore-Penrose pseudoinverse. The coefficients can therefore be calculated directly from the equation:

$$\vec{E} = (B^T B)^{-1} B^T \vec{c}. \quad (3.21)$$

The signal can then be approximated for arbitrary points on the sphere by evaluating the sum shown in (3.14), using the calculated coefficients and an updated set of base functions. In other words, for evaluating the function at the point  $(\theta_p, \phi_p)$  one evaluates the expression:

$$E(\theta_p, \phi_p) = \sum_{j=1}^R c_j Y_j(\theta_p, \phi_p). \quad (3.22)$$

This requires the recalculation of the SH base function at the point of interest.

### 3.5 Interpretation of the Coefficients

For many applications it is of interest how to interpret the coefficients of the SH series expansion. In the following I will derive a simple relationships between the described geometry and a SH coefficient, which is not commonly known in neuroscience yet. As shown earlier the coefficients are defined as:

$$c_j = \int_0^{2\pi} \int_0^\pi f(\theta, \phi) Y_j(\theta, \phi) \sin \theta \, d\theta d\phi. \quad (3.23)$$

This gives a direct connection between the first coefficient and the described shape. By using equation (3.11) and (3.13) the first coefficient can be calculated:

$$c_1 = \sqrt{\frac{1}{4\pi}} \int_0^{2\pi} \int_0^\pi f(\theta, \phi) \sin \theta \, d\theta d\phi. \quad (3.24)$$

This expression is equal to the integral of the function  $f(\theta, \phi)$  over the surface of the sphere, scaled by a factor. This is an important relationship for the interpretation of local models described by SH. The meanings of the other coefficients are not understood properly. For completeness sake I listed the second order coefficients ( $j = 2 \dots 6$ ) in the following:

$$\begin{aligned} c_2 &= \sqrt{\frac{15}{2\pi}} \int_0^{2\pi} \int_0^\pi f(\theta, \phi) \sin^3 \theta \cos 2\phi \, d\theta d\phi. \\ c_3 &= \sqrt{\frac{15}{2\pi}} \int_0^{2\pi} \int_0^\pi f(\theta, \phi) \sin^2 \theta \cos \theta \cos \phi \, d\theta d\phi. \\ c_4 &= \sqrt{\frac{5}{4\pi}} \int_0^{2\pi} \int_0^\pi f(\theta, \phi) (3 \cos^2 \theta - 1) \sin \theta \, d\theta d\phi. \\ c_5 &= \sqrt{\frac{15}{2\pi}} \int_0^{2\pi} \int_0^\pi f(\theta, \phi) \sin^2 \theta \cos \theta \sin \phi \, d\theta d\phi. \\ c_6 &= \sqrt{\frac{15}{2\pi}} \int_0^{2\pi} \int_0^\pi f(\theta, \phi) \sin^3 \theta \sin 2\phi \, d\theta d\phi. \end{aligned} \quad (3.25)$$

I have not found a simple ways of interpreting the meaning of these coefficients. Investigation of these integrals and their geometric interpretation may help for gaining further insight into the results of spherical deconvolution (Chapter 4.5) and q-ball (Chapter 4.4). This is especially interesting for the construction of metrics, as well as in the context of investigating spurious peaks and negative lobes.

## 3.6 Funk-Hecke Theorem

The Funk-Hecke theorem is an important integral for simplifying manipulations with spherical harmonics. For example, it is used for the derivation of the analytical solution in calculating the local model called q-ball (Descoteaux et al., 2010; D. S. Tuch, 2004). The Funk-Hecke theorem states that every surface SH is an eigenvector of integral operators

integrating over the surface of the sphere, whose kernels depend only on the distance between points in spherical geometry.

Formally this is defined by assuming  $f: [-1, 1] \mapsto \mathbb{R}$  to be a continuous, bounded and measurable function. The integral over the surface of the sphere ( $\Omega$ ) of the product of  $f$  with a spherical harmonic function then can be written as:

$$\int_{\Omega} f(\vec{u}^T \vec{\omega}) Y_l^m(\vec{\omega}) d\vec{\omega} = \lambda(l) Y_l^m(\vec{u}), \quad (3.26)$$

with  $\lambda(l)$  being defined as:

$$\lambda(l) = \frac{2\pi}{P_l(1)} \int_{-1}^1 P_l(t) \lambda(l) dt = 2\pi \int_{-1}^1 P_l(t) f(t) dt. \quad (3.27)$$

Here  $P_l(t)$  stands for the Legendre polynomial of degree  $l$ , which is not to be confused with the associated Legendre polynomial as defined in equation (3.8). The Legendre polynomial of degree  $l$  is defined as:

$$P_l(t) = 2^l \sum_{k=0}^n x^k \binom{n}{k} \binom{\frac{1}{2}(n+k-1)}{n}. \quad (3.28)$$

An important corollary of the Funk-Hecke theorem concerns the expansion of the Dirac delta function ( $\delta$ ), which is needed for the math behind both the local models q-ball and spherical deconvolution. This corollary is provided in the thesis of Descoteaux (Descoteaux, 2010). It states:

$$\int_{\Omega} \delta(\vec{u}^T \vec{\omega}) Y_l^m(\vec{\omega}) d\vec{\omega} = 2\pi P_l(0) Y_l^m(\vec{u}). \quad (3.29)$$

The Legendre polynomial of degree  $l$  evaluated at zero can be greatly simplified:

$$P_{l(0)} = \begin{cases} 0 & l \text{ odd} \\ (-1)^{\frac{l}{2}} \frac{1 \cdot 3 \cdot \dots \cdot (l-1)}{2 \cdot 4 \cdot \dots \cdot l} & l \text{ even} \end{cases} \quad (3.30)$$

Investigation of this function provides a great deal of insight on many problems arising in spherical deconvolution, which are discussed in depth in Chapter 4.5.

### 3.7 Spherical Convolution Theorem

Just like the Fourier expansion the SH expansion has some useful properties, which are utilized for example for computing local models. In this section I will focus on the spherical convolution theorem (Driscoll and D M Healy, 1994). It states that the spherical expansion of a convolution is equal to the point-wise product of the spherical expansions of the functions to be convolved. This is analogous to the result that the Fourier expansion of a convolution can be calculated by multiplication of the corresponding Fourier expansions. This theorem is the mathematical base for the computation of the spherical deconvolution local model (Tournier et al., 2007, 2004).

For properly phrasing the theorem I will for a second have to move away from the notation using the index  $j$ , introduced in equation (3.13) and instead define the SH expansion in terms of the order  $l$  and rank  $m$  of the SH base functions:

$$f(\theta, \phi) = \sum_{l=1}^{\infty} \sum_{m=-l}^l c_l^m Y_l^m(\theta, \phi) \quad (3.31)$$

Let  $f, g$  be functions defined on the surface of the sphere. Then the convolution is a point-wise product of the transforms:

$$(f * g)_l^m(\theta, \phi) = \sqrt{\frac{4\pi}{2l+1}} f_l^m(\theta, \phi) g_l^0(\theta, \phi). \quad (3.32)$$

It should be noted that convolution is not a symmetric operator on the sphere. The version stated above is the theorem for a right convolution (Driscoll and D M Healy, 1994). As can be seen for the function  $g$  only the SH functions of rank  $m = 0$  contribute to the convolution. This can be interpreted as the part of the function, which contributes to the convolution being z-aligned and rotational symmetric, since the SH functions representing other orientations do not contribute to the functions expansion. The function  $g$  in the equation is referred to as convolution kernel.

In terms of the expansion's coefficients the convolution theorem can be formulated using the index  $j$ :

$$(c_{f*g})_j = \sqrt{\frac{4\pi}{2l+1}} (c_f)_j (c_g)_{m(j)}, \quad (3.33)$$

where  $m(j)$  corresponds to the rank of the index  $j$ .

This theorem is especially important for the calculation of the local model spherical deconvolution (Tournier et al., 2004). Here one assumes the signal to be constituted by the convolution of the signal of fiber orientation distribution and the signal of a single z-aligned rotational symmetric fiber population. The calculation of the local model from the discrete SH expansions of the measured signal and the estimated kernel then amounts to the inversion of the convolution process shown in equation (3.33), which is a simple scalar division.

### 3.8 Sampling Theorem

When approximating a function, known only at discrete points, in terms of a SH expansion, the maximum rank  $R$  of the approximation strongly depends on the number of points at which the function is sampled. As stated before an upper limit can be defined by  $R = \frac{(L+1)(L+2)}{2}$ . However, this does not take into account the distribution of the samples and is a soft criterion based only on the number of parameters to estimate in the spherical harmonic model, not taking into account the distribution of points and therefore the sampling frequency. The fitted functions are then prone to aliasing or interpolation artifacts. However, sampling theorems only exist for equiangular sampling grids. A version of the spherical sampling theorem can be found in the work by Healy and colleagues (Dennis M. Healy et al., 1998).

Extension to the application in the area of local modeling would require the measurement of diffusion on equiangular grids as proposed by Daducci and colleagues (Daducci et al., 2011). On such a grid the sampling theorem holds. Otherwise a weighting of points needs to be introduced as a correction for not having sampled at the same frequencies. Furthermore the calculation then can be performed using fast spherical reconstruction algorithms such as the one presented by Driscoll and Healy (Driscoll and D M Healy, 1994).

I sadly cannot propose a sampling theorem for the grids used in MRI. This is however an area where further research could greatly improve the theory behind both SD and q-ball by mathematically defining sharp boundaries on the maximum SH order that can be used for a given number of diffusion measurements.

### 3.9 Conclusion

In this chapter I discussed the math of SH with the goal of introducing the necessary theorems and basics for understanding the derivation of certain local models (spherical



deconvolution, q-ball). I introduced the SH functions, the SH base as well as the SH expansion. The SH base is an orthonormal base for real and symmetric functions defined on the sphere. In terms of this base I introduced the SH expansion and discussed the meaning of the first coefficient. Interpretation of the other coefficients is still an open question which could lead to more insight in the results of SH based local models. I showed the Funk-Hecke theorem which is important for the simplification of SH expressions and solving integrals over the surface of the sphere. Afterwards I introduced the spherical convolution theorem, which spherical deconvolution is based upon. In this context a spherical sampling theorem would be of great interest which does not only cover equiangular samplings. This would be especially interesting in the context of determining the SH order for the use in the local models.

Something I have not discussed in this chapter, but will discuss later on (Chapter 4.5), are the problems which arise from the spherical representation of the local models. These problems include, but are not limited to, estimating maximum approximation order, arising of negative lobes, regularization issues and concealing of directional peaks.

In his thesis Descoteaux (Descoteaux, 2010) called SH a natural way to decompose signals on the sphere. In context of the problems arising in local modeling we should ask ourselves if there may be better alternatives to represent spherical data, especially when only having measured a sparse representation of a function of interest. I discuss this question more in depth in chapter 4.5.5. However, completely answering this would require an applicable sampling theorem, which can tell us the reliability of SH expansion depending on the order, when using the sparse data representation given through MRI.

# 4 Local Modeling

---

## 4.1 Introduction

Using dMRI the signal decay caused by the dephasing of spins of hydrogen nuclei can be measured. From this signal one wants to infer the microstructure in the human brain. However, one can only measure the microstructure indirectly. As stated in Chapter 2, microstructural barriers are observed in terms of reduced diffusion, which is a slower signal decay perpendicular to the boundary, than in an isotropic medium. From the signal profile one can therefore implicitly infer the microstructure.

To relate the measured diffusion weighted signal to the microarchitecture and especially the local fiber arrangement, it is necessary to impose a model connecting anatomy and diffusion signal. This model is called the local model, as it describes the influence of the local microstructural boundaries within a voxel on the spatial displacement of water molecules in that voxel, and it also describes the influence on the measured signal from that voxel.

One of the ways to determine the local arrangement is by reconstructing approximations of the so called diffusion propagator, which gives the probability of a particle diffusing from one position to another within the diffusion time (Callaghan, 1991; Cory et al., 1990). In practice not the true propagator, but the average water diffusion propagator within a voxel is reconstructed. Furthermore probing the diffusion propagator is constrained by sensitivity of the measurement with respect to diffusion direction, governed by the diffusion gradients, and diffusion time and length, expressed by the b-value. Together the diffusion direction and the diffusion time form the so-called q-space. The propagator is related to the tissue microstructure by the diffusion equation and appropriate boundary conditions (Fick, 1855). It can be calculated via Fourier transform from the signal attenuation. Reconstructing the full diffusion propagator, however, is impossible in practice, since it would require infinitely dense sampling of the whole q-space ( $\mathbb{R}^3$ ) and the diffusion time. One idea is to approximate the propagator by using a representative subspace, sampled at finite intervals in q-space and at a fixed diffusion time. This technique is known as diffusion spectrum imaging (DSI) (Wedeen et al., 2005). Since a rather large number of gradient directions and different b-values have to be examined, DSI significantly increases the necessary acquisition time, thereby reducing its clinical applicability.

One of the most used approximations of the diffusion propagator is the diffusion tensor. Here anisotropic Gaussian diffusion is assumed, leading to a diffusion propagator, which is described by a multivariate normal distribution, characterized by its covariance matrix, which is referred to as diffusion tensor. This technique is called *diffusion tensor imaging* (DTI) (P J Basser et al., 1994b) and is appropriate in situations with only one, approximately coherent, fiber population per voxel. One of the most significant limitations of this method lies in its inability to resolve the micro-structure in areas of more complex fiber geometries, for example crossing fibers. This situation, however, is rather common affecting between 30-60% (T. E. J. Behrens et al., 2007; Descoteaux et al., 2009; Jeurissen et al., 2010) of the measured white matter voxels at current resolutions.

In order to ease this situation multi-tensor models have been introduced, which allow more than one coherent fiber bundle within one voxel (Cook et al., 2005; Makris et al., 2002; D. Tuch, 2002). These methods are very attractive as long as the assumption holds, that the fibers belong to a small number of fairly coherent bundles. The advantage of these models is that they separate multiple fiber populations and describe each of these with the well-investigated diffusion tensor. However, in the work of Scherrer and Warfield (Scherrer and S K Warfield, 2010) it was shown that generalizing the multi-tensor model to any number of tensors per voxels leads to numerical problems stemming from the collinearity of the multi-tensor parameters. Therefore a single b-value is insufficient for estimating the full model of multiple tensors. This problem is usually mitigated by the introduction of additional constraints, such as restricting the number of tensor components (e.g.: two components; Caan et al., 2010; Geoffrey J M Parker and Daniel C Alexander, 2003), incorporating physiological constraints (Makris et al., 2002), reducing the complexity of the model by only allowing identical tensors (Tabelow et al., 2012). Other approaches use additional regularization or estimate a solution for optimization by using other local models. These approaches include stabilizing the problem by using Monte-Carlo algorithms (Kreher et al., 2005), regularizing over a spatial neighborhood (J. G. Malcolm et al., 2010; Pasternak et al., 2008), and incorporating other local models to estimate the initial non-linear optimization of the parameters of the multi-tensor model (Schultz et al., 2010).

A more sophisticated approximation of the diffusion propagator was introduced by Tuch (D. S. Tuch, 2004). He uses the Funk-Radon transform to evaluate only the marginal probability of the diffusion in a given direction, leading to the orientation profile of the diffusion propagator. The resulting profile is referred to as diffusion orientation density function (dODF) or q-ball. From its directional profile one can infer certain aspects of the orientation distribution of the underlying nerve fibers, in particular the main directions of the fiber bundles. The original dODF formulation uses a linear radial projection. It therefore overvalues points which are located close to the origin. This has led to the introduction of

more accurate dODF by considering the properties of the spherical coordinate system (Aganj et al., 2010; Alan Barnett, 2009; Canales-Rodríguez et al., 2009; Tristán-Vega et al., 2009). The two main approaches, however, differ in their description of the dODF. The differences between these two are investigated in more depth in Chapter 4.4. I additionally provide a framework which unifies the approaches and shows that their main difference lies in the assumption of the signal behavior beyond the measured sphere in q-space. This has also been investigated by Zhang and colleagues (N. Zhang et al., 2013).

All approaches mentioned so far involve models of the diffusion propagator, describing the relation between the measured signal and the water molecule displacement. The interpretation in terms of microstructure is then done rather intuitively, without any formalized relationship. A method that leads directly to a description of the fiber anatomy is spherical deconvolution (Dell'Acqua et al., 2007; Kaden et al., 2007; Tournier et al., 2007, 2004). In this model the signal is assumed to be constituted by the convolution of the signal associated to a single fiber or group of coherently oriented fibers with a fiber orientation density function (fODF). This method therefore requires a model of the signal of a single fiber or group of coherently oriented fibers, which is referred to as the convolution kernel. Alternatively, it is possible to calculate the fODF based on the dODF using an estimate of the dODF of a single fiber bundle as kernel (Descoteaux et al., 2009). A common framework for the different approaches to spherical deconvolution is given by Jian and Vermuri (Jian and Vermuri, 2007). Since spherical deconvolution requires an additional model the approach is classified as a so called model based approach, while the ones discussed earlier are called model free.

In this chapter I begin by introducing the diffusion propagator, which is a fundamental quantity of diffusion. Then I introduce the local models I investigated in depth, which are the diffusion tensor, the q-ball and spherical deconvolution. Furthermore I describe their calculation from the measured signal as well as their advantages and limitations. I investigate briefly the metrics which can be derived from each of these models. Metrics describe distances in a parameter space and are characterized by their sensitivity and specificity towards the differences in the physical quantities they are meant to reflect. In the context of dMRI, a sensitive metric should react to differences in a wide range of microstructural properties of the tissue, while a specific metric should be linked directly to a certain microstructural property.

Again for clarity I should mention that there basically are three distinct spaces one deals with when talking about local models. The first is the signal space. This is given in terms of the measured signal in each gradient direction. The second is the diffusion space. It is related to the measurement space by the Fourier relationship of the diffusion propagator

and describes the amount of diffusion occurring in each direction. The third is the fiber space, which can be calculated from as well the diffusion space as from the signal space by means of deconvolution using an appropriate representation of a single fiber population (kernel). As I discuss in Chapter 4.5.5 the connection between the kernel and the reconstructed fODF is not linear in the crossing fiber case. Therefore interpretation of results in any other space cannot be related directly to the underlying structure.

My main contribution in this chapter lies in the comparison of the math behind the dODF methods which do not use the linear radial projection used by Tuch. I formulate a common framework for the calculation of the corresponding dODFs. Additionally I investigated the crossing angle distribution for CSD and the relationship of these results to the approximation error of the Dirac delta function. This leads to insights on how identifying spurious peaks might be possible by variation of SH order.

## 4.2 The Diffusion Propagator

One of the most important quantities of diffusion is the diffusion propagator, as it can be used for describing the relation between diffusion and attenuation. The diffusion propagator  $P(\vec{r}_1, \vec{r}_2, \tau)$  (Callaghan, 1991) gives the probability of a particle traveling from  $\vec{r}_1$  to  $\vec{r}_2$  in time  $\tau$ . It is related to the underlying tissue by the diffusion equation and can be calculated from the signal attenuation via the Fourier transform ( $\mathcal{F}\{\dots\}$ ). For a given gradient direction  $\vec{q}$  in terms of the propagator the signal attenuation amounts to the following:

$$\begin{aligned} \frac{S(\vec{q}, \tau)}{S_0} &= \int_{\mathbb{R}^3} \int_{\mathbb{R}^3} P(\vec{r}_1, \vec{r}_2, \tau) \exp(i\vec{q}(\vec{r}_2 - \vec{r}_1)) d\vec{r}_1 d\vec{r}_2 \\ &= \mathcal{F}\{P(\vec{r}_1, \vec{r}_2, \tau)\}(\vec{q}, \tau). \end{aligned} \quad (4.1)$$

The magnitude of the signal-loss in presence of diffusion encoding depends on the diffusion gradient strength ( $G$ ) and duration ( $\delta$ ), which determines how sensitive the signal reacts towards diffusion, as well as the spatial distribution of the displacement during the time  $\tau$ . The quantities  $G$ ,  $\delta$  and  $\tau$  are known and incorporated in the so called b-value, which is defined as  $b = G^2 \gamma^2 \delta^2 \left( \tau - \frac{\delta}{3} \right)$ , where  $\gamma$  is the gyromagnetic ratio (Stejskal and Tanner, 1965). The above-mentioned relation only holds under the assumption of a narrow pulse approximation, which states that no significant diffusion occurs during the diffusion encoding process, i.e. the application of the diffusion gradient.

In practice the resolution at which one can observe diffusion is dictated by the voxel size, as one can only observe the average particle displacement in a given direction for the entire voxel. Therefore one cannot observe the diffusion propagator, but rather observes the propagator reflecting the spatial sum over the local microstructural environments present within the voxel (D. Tuch, 2002). Instead of traveling from position  $\vec{r}_1$  to  $\vec{r}_2$  one therefore rather observes the relative spin displacement, i.e.  $\vec{R} = \vec{r}_2 - \vec{r}_1$ . The resulting propagator, which can be described as the diffusion propagator averaged over all initial positions within the given voxel, is often referred to as the *ensemble-average propagator* (EAP) (D. Tuch, 2002). The relation to the diffusion propagator can be described using the position-dependent spin density ( $\rho$ ).

$$P(\vec{R}, \tau) = \int_{\vec{r}_1 \in V} P(\vec{r}_1, \vec{R} + \vec{r}_1, \tau) \rho(\vec{r}_1) d\vec{r}_1 \quad (4.2)$$

The EAP is related to the measured signal by a simple inverse Fourier relationship. This relation is derived for example in the work of Tuch (D. S. Tuch, 2004).

$$P(\vec{R}, \tau) = \int_{\vec{q} \in \mathbb{R}^3} \frac{S(\vec{q}, \tau)}{S_0} \exp(-i\vec{q}^T \vec{R}) d\vec{q} = \mathcal{F}^{-1} \left\{ \frac{S(\vec{q}, \tau)}{S_0} \right\} (\vec{R}, \tau) \quad (4.3)$$

This relation describes a method for the reconstruction of the EAP. Reconstructing the full EAP, however, is impossible in practice, since it would require infinitely dense sampling of the whole q-space ( $\mathbb{R}^3$ ) for all diffusion times. Several of the local models can be linked to the diffusion propagator and the question, how to efficiently sample q-space to maintain the significant features of the propagator.

It should again be noted, that even if one was able to completely reconstruct the diffusion propagator, that the connection to microstructure is still implicit, as the propagator describes the diffusion profile. For relating the propagator to the microstructure additional models are necessary, especially since the observed propagator is the EAP. This is discussed in more detail in the work by Jones and colleagues (Derek K Jones et al., 2013).

## 4.3 Diffusion Tensor

### 4.3.1 Introduction

The simplest way to approximate the diffusion propagator is by using a Gaussian assumption for modeling the radial profile of the diffusion signal. For an isotropic medium

this amounts to the diffusion tensor (P J Bassler et al., 1994a). In the following I will derive the diffusion tensor and describe the most popular method for calculating the tensor from the measured signal data.

The diffusion process can be characterized by a diffusion coefficient, which describes the mean square displacement of a particle undergoing Brownian motion. According to the Einstein-Smoluchowsky equation (Einstein, 1956) the diffusion coefficient, which describes the direction independent mobility of a molecule or particle in an isotropic medium, is given by:

$$d = \frac{1}{6\Delta} \langle \vec{r}^T \vec{r} \rangle, \quad (4.4)$$

where  $\vec{r} = \vec{r}_\tau - \vec{r}_1$ , i.e. the displacement of a spin from the position  $\vec{r}_1$  to the position  $\vec{r}_\tau$  in time  $\tau$  and the operator  $\langle \dots \rangle$  denotes the average over the spin ensemble. The diffusion coefficient for a fixed gradient direction  $\vec{g}$  can be related to the attenuation signal of a dMRI measurement by the Stejskal-Tanner equation (Stejskal and Tanner, 1965):

$$\frac{S(\vec{g})}{S_0} = \exp(-b d(\vec{g})). \quad (4.5)$$

It should be noted that the Stejskal-Tanner equation was initially derived from a NMR pulse sequence. Since in dMRI there are many more influences on the diffusion gradient and the dMRI pulse sequence is much more complex than in the original experiment by Stejskal and Tanner, the diffusion coefficient measured is actually an *apparent diffusion coefficient* (ADC) and not the true diffusion coefficient. In clinical application the ADC is sometimes still used as an easily calculated metric. Instead of using the ADC in a single direction the average ADC is calculated for several directions (Moseley et al., 1990).

The idea of a diffusion tensor was introduced to dMRI by Bassler and colleagues (P J Bassler et al., 1994a), who showed that the ADC was highly direction dependent in parts of the brain. They concluded that an isotropic diffusion model does not correctly represent the brain's cell microstructure. The simplest generalization is to assume anisotropic diffusion hindered by a single barrier. This leads to the generalization of Einstein's diffusion equation to a tensor instead of a single coefficient, which can be understood as relation between the covariance matrix of the average particle displacement  $\vec{R}$  for a diffusion time  $\tau$ :

$$D = \frac{1}{6\tau} \langle \vec{R}^T \vec{R} \rangle. \quad (4.6)$$

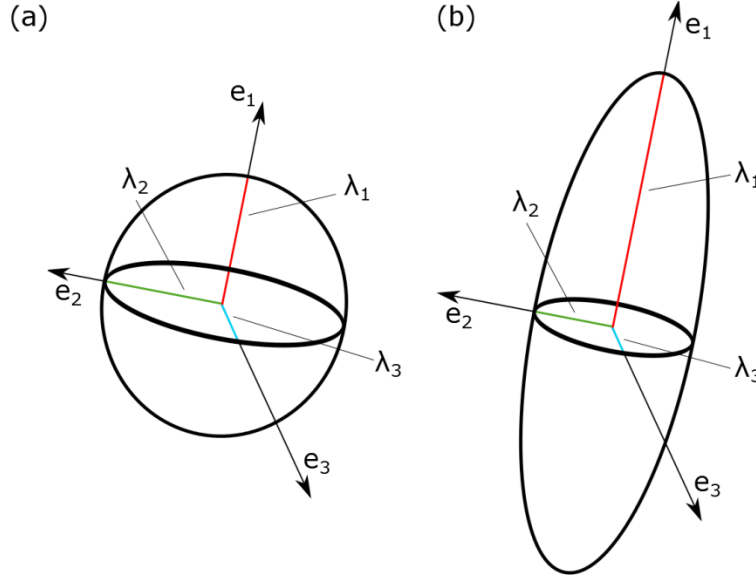


Figure 4.1: The diffusion tensor. The tensor is usually visualized as an ellipsoid. Here an isotropic (a) and an anisotropic tensor (b) are shown. The dimensions of the tensor are described by the tensor's eigenvalues ( $\lambda_i$ ) and eigenvectors ( $e_i$ ). The ellipsoid describes the distance a particle travels within the diffusion time  $\tau$ . As the eigenvalues describe the dimensions of the tensor, similar eigenvectors indicate isotropy, while a difference between the eigenvalues indicates anisotropy.

Campbell (Campbell, 2004) showed that if one uses Einstein's diffusion equation and the first order Taylor expansion of the EAP about  $\vec{R}$  and  $\tau$ , then the propagator is defined by the differential equation:

$$\frac{\delta P(\vec{R}, \tau)}{\delta \tau} = D \nabla^2 P(\vec{R}, \tau). \quad (4.7)$$

The solution to this gives the Gaussian propagator:

$$P(\vec{R}, \tau) = \frac{1}{\sqrt{(4\pi\tau)^3 \det(D)}} \exp\left(-\frac{1}{4\tau} \vec{R}^T D^{-1} \vec{R}\right). \quad (4.8)$$

This can be seen as approximating the full propagator in terms of a 3-variate normal distribution. The diffusion tensor then describes the symmetric covariance matrix of the water molecules' Brownian motion.



### 4.3.2 Calculation of the Tensor from the Diffusion Signal

The connection between the measured signal and the diffusion tensor is in principle given by the Stejskal-Tanner equation (4.5). In the following I will discuss the calculation of the diffusion tensor from the diffusion signal.

As stated above the tensor can be seen as the symmetric covariance ( $3 \times 3$ )-matrix of the water molecules' Brownian motion. It consequently can be described by a matrix with 3 unique diagonal entries and 3 unique off diagonal entries, i.e. 6 unique entries.

$$D = \begin{pmatrix} d_{xx} & d_{xy} & d_{xz} \\ d_{xy} & d_{yy} & d_{yz} \\ d_{xz} & d_{yz} & d_{zz} \end{pmatrix}. \quad (4.9)$$

Consequently at least 7 image acquisitions (1 non-diffusion-weighted for determining the attenuation and 6 diffusion-weighted) are necessary for fully determining the diffusion tensor. In the following  $S_0$  shall denote the non-diffusion-weighted signal and  $S(\vec{g}_i)$  the diffusion-weighted signal at a b-value of  $b$  for  $n$  gradients  $\vec{g}_i = (g_x^i, g_y^i, g_z^i)$  with  $i = 1, \dots, n$ . With these definitions one can formulate a system of linear equations for estimating the diffusion tensor. The Stejskal-Tanner Equation (4.5) can be written in terms of the diffusion tensor:

$$\frac{S(\vec{g}_i)}{S_0} = \exp(-b\vec{g}_i D \vec{g}_i^T). \quad (4.10)$$

In practice this can be solved using a linear equation system. First the  $(n \times 6)$ -matrix  $B$  is defined:

$$B = \begin{pmatrix} g_x^1 g_x^1 & 2g_x^1 g_y^1 & 2g_x^1 g_z^1 & g_y^1 g_y^1 & 2g_y^1 g_z^1 & g_z^1 g_z^1 \\ \vdots & \vdots & \vdots & \vdots & \vdots & \vdots \\ g_x^n g_x^n & 2g_x^n g_y^n & 2g_x^n g_z^n & g_y^n g_y^n & 2g_y^n g_z^n & g_z^n g_z^n \end{pmatrix}. \quad (4.11)$$

The tensor then is described in terms of a single vector  $\vec{d}$  containing the six values which have to be determined for defining the tensor, that is:

$$\vec{d} = (d_{xx}, d_{xy}, d_{xz}, d_{yy}, d_{yz}, d_{zz}). \quad (4.12)$$

By taking the logarithm of the measured signal attenuation, a vector  $\vec{s}$  is defined:

$$\vec{s} = \left( \ln\left(\frac{S(\vec{g}_1)}{S_0}\right) \quad \dots \quad \ln\left(\frac{S(\vec{g}_n)}{S_0}\right) \right)^T. \quad (4.13)$$

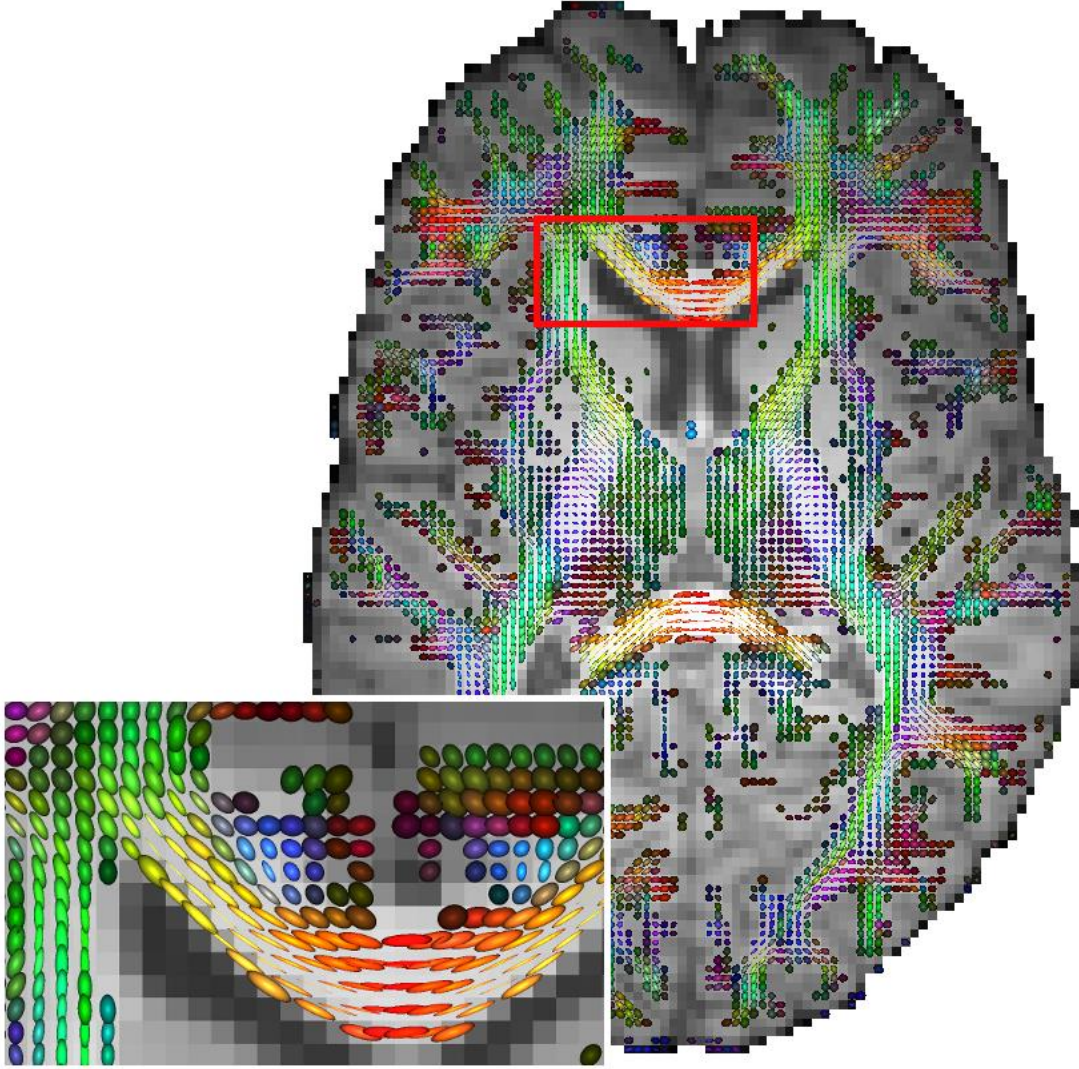


Figure 4.2: Tensors colored using the RGB color map. The tensors are visualized as ellipsoids and colored using the first eigenvector. Red stands for left-right, green for anterior-posterior and blue for dorsal-ventral direction. Round tensors indicate more than one fiber population being present, while elongated tensors indicate collinear fiber populations.

Using the matrix  $B$  and the vectors  $\vec{d}$  and  $\vec{s}$  equation (4.10) can be rewritten as:

$$\vec{s} = B\vec{d}. \quad (4.14)$$

This over determined linear system can be solved by least square fitting of  $\vec{d}$  by calculating the Moore-Penrose pseudoinverse (Penrose, 2008). The resulting entries of  $\vec{d}$  then define the tensor. As a comment it should be noted, that the noise on dMRI data is not Gaussian distributed but follows a Rician distribution (Andersen, 1996; Gudbjartsson and Patz, 1995).

By performing least square fitting one implicitly assumes the noise to have the same distribution as the underlying process. This can lead to a bias of the reconstructed tensor. As a solution, more complex tensor fitting approaches have been introduced (Arsigny et al., 2006; Lenglet et al., 2006). An overview over clinically applied diffusion tensor estimation methods is found in the work of Fillard and colleagues (Fillard et al., 2007). A typical tensor ellipsoid is shown in Figure 4.1.

### 4.3.3 Tensor Metrics

The diffusion tensor can be characterized in terms of its eigenfunctions. These are the three eigenvectors ( $\vec{e}_i$ ) and eigenvalues ( $\lambda_i$ ). Since the tensor characterizes the covariance matrix of the Gaussian diffusion propagator these have a close relation to the propagator.

The tensor's eigenfunctions are calculated by eigendecomposition of the  $(3 \times 3)$  diffusion tensor matrix:

$$D = (\vec{e}_1 \vec{e}_2 \vec{e}_3) \begin{pmatrix} \lambda_1 & 0 & 0 \\ 0 & \lambda_2 & 0 \\ 0 & 0 & \lambda_3 \end{pmatrix} (\vec{e}_1 \vec{e}_2 \vec{e}_3)^T \quad (4.15)$$

By convention the eigenvalues and their eigenvectors are sorted by size. The largest is the first eigenvalue ( $\lambda_1$ ). The eigenvectors are normalized to be orthonormal. As shown in Figure 4.1, the eigenvalues gives the distance that a particle maximally moves in the direction of the corresponding eigenvector.

The diffusion tensor is usually visualized as an ellipsoid. The ellipsoid is then colored using an RGB color map (Pajevic and Pierpaoli, 1999), which is obtained by encoding the coordinates of the first eigenvector ( $\vec{e}_1 = (x, y, z)$ ) in terms of a color. The corresponding RGB map gives an indication of the spatial orientation of the diffusion tensor. An example is shown in Figure 4.2.

The eigenvalues are used to calculate several metrics, which are indicators of the tissue microstructure. The most prominent and most widely used metric is the *fractional anisotropy* (FA) (Pierpaoli and P J Basser, 1996; Westin et al., 2002). It basically describes the shape of the diffusion tensor, by characterizing the mean spread of the eigenvalues. It is defined as:

$$FA = \sqrt{\frac{3}{2} \frac{\sqrt{(\lambda_1 - \langle \lambda \rangle)^2 + (\lambda_2 - \langle \lambda \rangle)^2 + (\lambda_3 - \langle \lambda \rangle)^2}}{\sqrt{\lambda_1^2 + \lambda_2^2 + \lambda_3^2}}}, \quad (4.16)$$

with  $\langle \lambda \rangle$  denoting the mean eigenvalue, which is also referred to as mean diffusivity. This metric is zero in case of the eigenvalues being identical and is close to one if one is larger

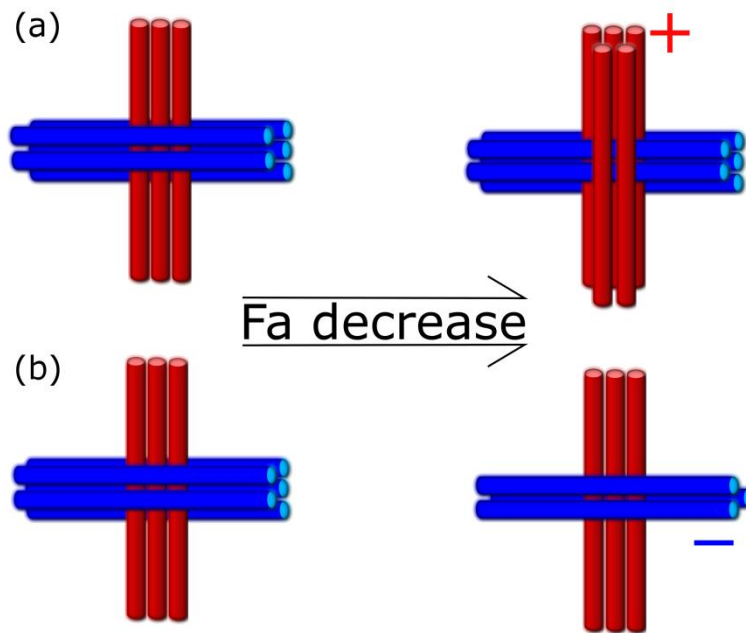


Figure 4.3: Specificity and sensitivity of FA. On the left the same fiber configuration is shown. In the top image (a) the secondary fiber bundle (red) is increased, while in the second image the primary fiber population (blue) is decreased. Both of these changes lead to a reduction of FA. The FA therefore is sensitive to both changes, however cannot discern the changes. This implies that the FA is sensitive to changes in configuration, but not specific to the type of change.

than the others. If it is zero it therefore describes a sphere like tensor and if it is close to one it describes an elongated tensor. Of the various metrics calculated from MRI this is the one which has been studied the most and is used the most in clinical application (Leow et al., 2009; Yamada et al., 2009). For an overview of applications see the work by Jones and colleagues (Derek K Jones et al., 2013). However the FA does not characterize the tensor shape completely as different combinations of eigenvalues can generate the same FA (A. L. Alexander et al., 2000). Exemplary maps of the tensor metrics are depicted in Figure 4.4.

It should be pointed out, that while the low degrees of freedom of the tensor make it very easy to compute, it also means that metrics derived from the tensor are very unspecific. This fact is visualized for the FA in Figure 4.3.

Two other important metrics derived from the diffusion tensor are the radial and the axial diffusivity. The axial diffusivity corresponds to the largest eigenvalue, while the radial diffusivity is the mean value of the second and third eigenvalue. It has been shown, that these metrics are sensitive to certain pathologies (S.-K. Song et al., 2002). However, so far it has not been possible to find a robust, quantitative relationship between a single

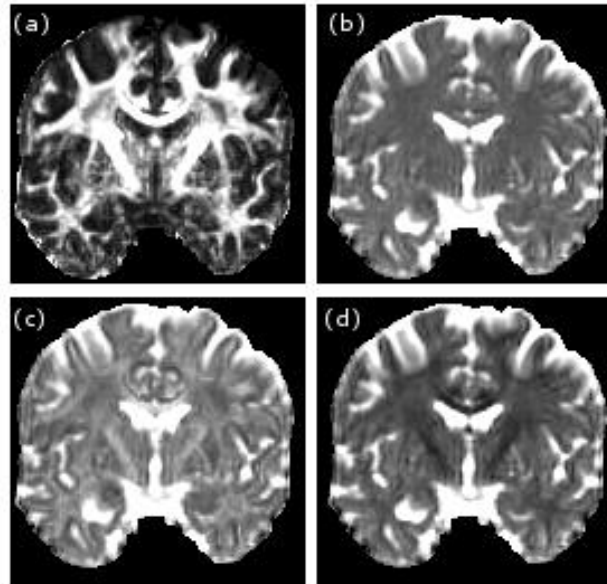


Figure 4.4: Maps of tensor metrics. Here the tensor metrics are visualized using a coronal section. The metrics are FA (a), MD (b), AD (c), RD (d). Each of these metrics describes a different aspect of the shape of the diffusion tensor.

microstructural property and the parameters extracted from the tensor (Derek K Jones et al., 2013). An overview over the tensor metrics is given in Figure 4.4.

#### 4.3.4 Advantages and Limitations of the Diffusion Tensor

The Gaussian approximation of the diffusion propagator uses the assumption, that the diffusion in a voxel is hindered by a single barrier. While this assumption is violated in large parts of the brain it leads to a fairly useful approximation of the propagator, since this approximation is easily computed, needs only a few measurements and is fairly robust.

The advantage of this local model lies in the ease of estimation, as only seven image acquisitions are necessary. This has led to this method becoming the standard clinical method (Leow et al., 2009). Therefore vast literature covering the model, its application and the analysis of the method is available. For an overview see the work of Jones and colleagues (Derek K Jones et al., 2013). However, it has severe limitations. The Gaussian diffusion assumption is violated in large parts of the brain, as more complex geometries than a single fiber are present. While this method is highly accurate in some regions, the Gaussian assumption makes it insufficient for a lot of applications. Furthermore only sampling at a constant radius, that is a constant b-value, disregards the radial information of the diffusion signal.

When calculating the diffusion tensor from HARDI measurements, the measurement space is reduced strongly. This leads to a very good robustness towards noise. On the other hand, this also leads to a considerable loss of information. In case of HARDI it therefore is recommended to use more complex models to incorporate more of the information contained in the data.

## 4.4 Diffusion Orientation Density Function

### 4.4.1 Introduction

The diffusion tensor assumes the diffusion signal to be constituted by a single coherent fiber population hindering anisotropic Gaussian diffusion. Therefore it cannot describe more complex configurations properly. Instead of using an explicit model for the diffusion, like in the tensor case, one can model the diffusion propagator directly by exploiting the Fourier relationship between the propagator and the diffusion signal (Callaghan, 1991). A method directly using this relationship is QSI, which uses a representative sampling of q-space in order to locally reconstruct the diffusion propagator. This method however is very time-consuming, since a large number of samples is required, rendering the method infeasible for clinical application.

This limitation was first circumvented by Tuch (D. S. Tuch, 2004), who used the Funk-Radon transform to estimate the marginal probability of diffusion in a given direction from the diffusion signal, measured on a sphere in q-space (q-ball). This result is referred to as the *diffusion orientation density function* (dODF). From its directional profile one can infer certain aspects of the orientation distribution of the underlying nerve fibers, in particular the main directions of the fiber bundles. In the definition of the dODF used by Tuch, however, not the true marginal probability of diffusion from the EAP is calculated. A linear radial projection of the EAP is computed instead, which disregards the quadratic growth of the volume element with its distance to the origin. Therefore points close to the origin are overvalued which distorts the dODF. This in turn leads to the need of normalization of the dODF, since it does not integrate to unit mass. Additionally the dODF is not dimensionless, but has the unit  $l^{-3}$  where  $l$  stands for the spaces length dimension. These problems are reconciled in the work by Aganj and colleagues (Aganj et al., 2010), in the work by Tristan-Vega and colleagues (Tristán-Vega et al., 2009) and in the work by Zhang and colleagues (N. Zhang et al., 2013). I investigated the works of Aganj and colleagues as well as Tristan-Vega and colleagues in depth.

In the following subchapters I will first give an overview over the calculation of the dODF in the frameworks by Tuch and colleagues, Aganj and colleagues as well as Tristan-Vega and

colleagues. As the dODF is computed from a q-ball, that is a sphere in q-space, the method for calculating the dODF is referred to as *q-ball imaging* (QBI). I compare the three approaches for calculating the dODF discussing the similarities and the differences in their assumptions and provide a common framework.

## 4.4.2 General Definitions

Instead of reconstructing the full EAP, in QBI one seeks to reconstruct the dODF. The dODF is a probability density function, which gives the probability of a particle diffusing from the origin to the infinitesimal solid angle volume element  $dv$  lying in direction  $\vec{u}$  within the diffusion time  $\tau$ . The dODF can be written in Cartesian coordinates. However, in dMRI one is mostly interested in the spherical representation of the dODF. The volume element  $dv$  in spherical coordinates can be written as:

$$dv = r^2 dr d\Omega, \quad (4.17)$$

where  $\Omega$  stands for the surface of the unit sphere and has the property  $d\Omega = \sin\theta d\theta d\phi$ . Subsequently the radial integral of the EAP in spherical coordinates can be written as:

$$\psi(\vec{u}) = \int_0^\infty P(r\vec{u}, \tau) r^2 dr, \quad (4.18)$$

where  $\vec{u}$  is a unit vector and  $r$  is the radial coordinate in the diffusion space coordinate system. For a fixed diffusion time this defines the dODF  $\psi$ . For comparison, the linear projection used in the work of Tuch is defined as:

$$\psi_{lin}(\vec{u}) = \frac{1}{Z} \int_0^\infty P(r\vec{u}, \tau) dr, \quad (4.19)$$

with a normalization constant  $Z$ , which ensures that  $\psi_{lin}$  is of unit mass. In the following I will refer to  $\psi_{lin}$  as linear dODF. As can be seen from comparing (4.18) and (4.19) the linear projection introduces a weighting by the factor  $r^{-2}$ . This leads to overvaluing of values close to the origin.

Computing the linear dODF as well as the general dODF requires the Funk-Radon transform ( $\mathcal{G}\{\dots\}$ ), which is a transformation of the sphere onto itself. This transformation gives a value in direction  $\vec{u}$  by integrating the function  $f$  on the sphere over the great circle in the plane perpendicular to the direction  $\vec{u}$ . Formally this is defined by:

$$\mathcal{G}[f(\vec{w})](\vec{u}) = \int_{\vec{w} \in \vec{u}^\perp} f(\vec{w}) d\vec{w} = \int_{S^2} f(\vec{w}) \delta(\vec{w}^T \vec{u}) d\vec{w}, \quad (4.20)$$

where  $\delta$  stands for the Dirac delta function.

For all methods the Fourier connection between the measured signal and the diffusion propagator is required. The relation is defined in equation (4.3), which is related to the inverse Fourier transform as follows:

$$P(\vec{R}, \tau) = \int_{q \in \mathbb{R}^3} \frac{S(\vec{q}, \tau)}{S_0} \exp(-i\vec{q}^T \vec{R}) dq = \mathcal{F}^{-1} \left\{ \frac{S(\vec{q}, \tau)}{S_0} \right\} (\vec{R}, \tau). \quad (4.21)$$

Since from here on one can assume the diffusion time to be fixed I will not continue to carry the variable  $\tau$ , which describes the diffusion time in the following formulas.

### 4.4.3 Linear dODF

As shown by Tuch (D. S. Tuch, 2004) the linear dODF is related directly to the Funk-Radon transform of the attenuation signal:

$$\begin{aligned} \mathcal{G}\{E(\vec{q})\}(\vec{u}) &= 2\pi \int_{-\infty}^{\infty} \int_0^{2\pi} \int_0^{\infty} P(r\vec{u}) J_0(2\pi r) r dr d\theta d\phi \\ &\approx Z \int_{-\infty}^{\infty} P(r\vec{u}) dr, \end{aligned} \quad (4.22)$$

where  $J_0$  is the 0<sup>th</sup> order Bessel function, which is used in the Funk-Radon transform to approximate the Dirac delta function. For the linear dODF equation (4.21) simplifies to the following:

$$\psi_{lin}(\vec{q}) \approx \frac{1}{Z} \mathcal{G} \left\{ \frac{S(\vec{q})}{S_0} \right\}. \quad (4.23)$$

It should however be noted that due to the Funk-Radon transform some blurring is introduced. The equation (4.23) can be solved analytically by using the Funk-Hecke theorem and a spherical representation of the measured signal attenuation. As shown in the work of Descoteaux (Descoteaux, 2010) the Funk-Hecke transform of the signal attenuation amounts to:



$$\begin{aligned}
\mathcal{G}\left\{\frac{S(\vec{q})}{S_0}\right\} &= \int \delta(\vec{q}^T \vec{\omega}) \left(\frac{S(\vec{\omega})}{S_0}\right) d\omega \\
&= \sum_{j=1}^R c_j 2\pi P_{l(j)}(0) Y_j(\vec{q}).
\end{aligned} \tag{4.24}$$

The estimation of the linear dODF  $\psi_{lin}$  then can be performed by simple multiplication of the coefficients of the spherical representation of the signal with  $2\pi P_{l(j)}$ . In other words, let the matrix  $B$  be the SH base as defined in equation (3.20), the vector  $\vec{S} = \left(\frac{S(\vec{g}_1)}{S_0}, \dots, \frac{S(\vec{g}_n)}{S_0}\right)$  be the signal attenuation vector observed for the  $n$  gradient directions ( $g_1, \dots, g_n$ ) and  $G$  be the diagonal matrix with entries  $G_{jj} = 2\pi P_{l(j)}$ . Then the calculation of the dODF coefficients of the SH expansion amounts to:

$$\vec{c}_{\psi_{lin}} = G(B^T B)^{-1} B^T \vec{S}. \tag{4.25}$$

In the work of Descoteaux (Descoteaux, 2010) a Laplace-Beltrami regularization parameter is introduced. Including the regularization parameter in equation (4.25) leads to the expression:

$$\vec{c}_{\psi_{lin}} = G(B^T B + \lambda L)^{-1} B^T \vec{S}, \tag{4.26}$$

where  $\lambda$  is a regularization parameter and the matrix  $L$  is a diagonal matrix with entries  $L_{jj} = l(j)^2(l(j) + 1)^2$ . This introduces additional smoothness constraints by suppression of higher order values.

Evaluation of the dODF for points in the SH base  $B^*$  is then done by simple matrix vector multiplication:

$$\vec{\Psi}_{lin} = B^* \vec{c}_{\psi_{lin}} \tag{4.27}$$

This requires the calculation of the SH base at all points at which the dODF is of interest.

In practice, the normalization parameter  $\frac{1}{Z}$  from equation (4.23) is not explicitly calculated. Instead the dODF is usually min-max normalized. This of course leads to a misrepresentation of rounder glyphs. In theory the dODF would have to be scaled, using their first spherical harmonic coefficients, since the first coefficient gives the integral of  $\psi_{lin}$  over the sphere (see Chapter 3.5).

#### 4.4.4 General dODF

The basic idea behind the general dODF formulation is that the Fourier transform of the spherical EAP is related to the Laplacian  $\nabla^2$  of the signal. This result uses a basic relation of Fourier analysis theory and is provided in the work of Aganj and colleagues (Aganj et al., 2009). The relationship amounts to:

$$\mathcal{F}(P(r\vec{u})r^2) = -\nabla^2 E(\vec{q}), \quad (4.28)$$

where  $\vec{u}$  is an arbitrary unit vector. In spherical coordinates  $(q, \theta, \phi)$ , the Laplacian of the signal is defined as:

$$\begin{aligned} \nabla^2 E(\vec{q}) = & \frac{1}{q^2} \frac{\partial}{\partial q} \left( q^2 \frac{\partial E(\vec{q})}{\partial q} \right) + \frac{1}{q^2 \sin \theta} \frac{\partial}{\partial \phi} \left( \sin \theta \frac{\partial E(\vec{q})}{\partial \phi} \right) \\ & + \frac{1}{q^2 \sin^2 \theta} \frac{\partial E(\vec{q})}{\partial \theta}, \end{aligned} \quad (4.29)$$

which can be split into a radial part and a radius independent part for calculating the general dODF:

$$\nabla^2 E(\vec{q}) = \frac{1}{q^2} \frac{\partial}{\partial q} \left( q^2 \frac{\partial E(\vec{q})}{\partial q} \right) + \frac{1}{q^2} \nabla_b^2 E(\vec{q}). \quad (4.30)$$

The operator  $\nabla_b^2$  is the Laplace-Beltrami operator. Using this relation and the Funk-Radon transform the general dODF can be written analogously to equation (4.26):

$$\psi(\vec{u}) \approx \frac{1}{2} \mathcal{G} \left\{ -\frac{1}{4\pi^2 q^2} \frac{\partial}{\partial q} \left( q^2 \frac{\partial E(\vec{q})}{\partial q} \right) \right\} + \frac{1}{2} \mathcal{G} \left\{ -\frac{1}{4\pi^2 q^2} \nabla_b^2 E(\vec{q}) \right\}. \quad (4.31)$$

Applying the Funk-Radon transform leads to a sum of two integrals, one representing the radial part and the other the angular part:

$$\psi(\vec{u}) = -\frac{1}{8\pi^2} \iint_{\vec{q} \in \vec{u}^\perp} \frac{1}{q^2} \frac{\partial}{\partial q} \left( q^2 \frac{\partial E(\vec{q})}{\partial q} \right) d^2 \vec{q} - \frac{1}{8\pi^2} \iint_{\vec{q} \in \vec{u}^\perp} \frac{1}{q^2} \nabla_b^2 E(\vec{q}) d^2 \vec{q}, \quad (4.32)$$

where  $\vec{u}^\perp$  stands for the plane perpendicular to the vector  $\vec{u}$ . As shown in the work by Aganj and colleagues (Aganj et al., 2010), the radial part is constant, assuming that the diffusion signal and its radial derivative go to zero (relatively fast) as the radius goes to infinity. Under these assumptions the radial part is constant:

$$\iint_{\vec{q} \in \vec{u}^\perp} \frac{1}{q^2} \frac{\partial}{\partial q} \left( q^2 \frac{\partial E(\vec{q})}{\partial q} \right) d^2 \vec{q} = -2\pi. \quad (4.33)$$

The difficulty lies in the evaluation of the angular portion of the integral. This is also the point where the works by Aganj and colleagues (Aganj et al., 2010) as well as the work of Tristan-Vega and colleagues (Tristán-Vega et al., 2009) diverge. Zhang and colleagues (N. Zhang et al., 2013) take a completely different approach, which tries to minimize the approximation error due to the Funk-Radon transform, by replacing the radial part with its mean value over the sphere. Since I investigated the differences and similarities in the dODF reconstruction methods before the work of Zhang et al. was published, I will only discuss the other two approaches in depth.

After calculating the radial portion the equation (4.32) simplifies to:

$$\psi(\vec{u}) = \frac{1}{4\pi} - \frac{1}{8\pi^2} \iint_{\vec{q} \in \vec{u}^\perp} \frac{1}{q^2} \nabla_b^2 E(\vec{q}) d^2 \vec{q}. \quad (4.34)$$

The approach by Aganj and colleagues to calculate the dODF is often referred to as *planar orientation probability density transform* (p-OPDT), while the approach by Tristan-Vega and colleagues is referred to as *circular orientation probability density transform* (c-OPDT). This stems from their assumptions for solving the angular portion of the integral.

Aganj and colleagues assume the signal to decay mono-exponentially with the radius, in order to approximate the behavior of  $E(\vec{q})$  in the entire  $q$ -space. This approximation is required for evaluating the integral in (4.34) within the entire plane  $\vec{u}^\perp$ . This results in the dODF  $\psi_p$ :

$$\psi_p(\vec{u}) \approx \frac{1}{4\pi} - \frac{1}{8\pi^2} \mathcal{G}\{\nabla_b^2 \ln(-\ln E(\vec{q}))\}(\vec{u}). \quad (4.35)$$

Tristan-Vega and colleagues on the other hand calculate the dODF  $\psi_c$  by approximating the integral in the entire plane  $\vec{u}^\perp$  by the integral on a disk in the plane. This assumes that the attenuation signal changes much faster than the shape of the ADC does. This allows the use of Stokes' theorem for solving the integral:

$$\psi_c(\vec{u}) \approx \frac{1}{4\pi} - \frac{1}{8\pi^2} \mathcal{G}\left\{\nabla_b^2 \frac{1}{2} E_{in}(-\ln E(\vec{q}))\right\}(\vec{u}). \quad (4.36)$$

The function  $E_{in}$  hereby stands for:

$$E_{in}(x) = \sum_{k=1}^{\infty} \frac{(-x)^k}{k \cdot k!}, \quad (4.37)$$

which describes the signal decay with the radius, substituting the mono-exponential decay assumed in the work of Aganj and colleagues. For more information on the calculation of the function  $E_{in}$  see the work of Tristan-Vega and colleagues (Tristán-Vega et al., 2010). In a common framework the dODF  $\psi$  could be described by:

$$\psi(\vec{u}) \approx \frac{1}{4\pi} - \frac{1}{8\pi^2} G\{\nabla_b^2 \mathcal{E}(-\ln E(\vec{q}))\}(\vec{u}), \quad (4.38)$$

where  $\mathcal{E}$  is a function describing the assumption of the radial signal decay. To distinguish between the results of p-OPDT and c-OPDT, I will refer to  $\psi_p$  as p-dODF and to  $\psi_c$  as c-dODF. The framework (4.38) allows the use of different assumptions on the signal decay.

#### 4.4.5 Calculation of the dODF from the Diffusion Signal

As discussed in the previous chapter the c-dODF and the p-dODF vary mainly in their assumption of the radial signal decay. For defining a common framework I therefore first need to introduce a term covering the signal approximation, which is denoted by the vector  $\vec{A}(\vec{S})$ , while  $\vec{S}$  denotes the signal attenuation vector, as defined in Chapter 4.4.3. The vector of coefficients  $\vec{c}_\Psi$  of the generalized ODF  $\Psi$  can then be written as:

$$\vec{c}_\Psi = -\frac{1}{8\pi^2} GL(B^T B + \lambda L^2)^{-1} B^T \vec{A}, \quad (4.39)$$

where the matrices  $B$ ,  $G$  and  $L$  are the SH base matrix, the diagonal Funk-Radon transform matrix and the diagonal Laplace-Beltrami regularization matrix. In case of the c-dODF and p-dODF the vector  $\vec{A}$  is defined differently:

$$\begin{aligned} \vec{A}_{c-dODF} &= -\log(-\log(\vec{S})), \\ \vec{A}_{p-dODF} &= E_{in}(-\log(\vec{S})). \end{aligned} \quad (4.40)$$

The calculation of the corresponding dODF values is less straightforward than in the case of the linear dODF, as for evaluating the dODF at points contained in the SH base  $B^*$  requires an extra addition step:

$$\vec{\Psi}_{B^*} = B^* \vec{c}_\Psi + \frac{1}{4\pi}. \quad (4.41)$$

#### 4.4.6 dODF Metrics

The dODF describes the probability of a particle diffusing in a particular direction. Therefore the peaks of the dODF can be interpreted as a large number of particles diffusing in the corresponding direction. This is a strong indicator that a collinear fiber population exists which is aligned with that direction. For quantifying this in terms of geometric properties, which again would lead to an interpretation in terms of the underlying microstructure, metrics describing this connection are of great interest. However, calculation of metrics from the dODF is not as straightforward, as for example in the tensor case. This is mainly because of the dODF describing diffusion and not structure, but also because of the description of the dODF in terms of a SH expansion and the dODF being a multimodal distribution. Due to the SH representation one can only infer information in terms of SH expansion coefficients directly (see Chapter 3.5). This currently does not exceed the first coefficient of the SH expansion which is basically the integral of the dODF over the sphere, which should be equal to  $\frac{1}{\sqrt{4\pi}}$  (as shown in Chapter 3.5). On the other hand, the multimodal distribution structure makes derivation of metrics from the dODF difficult, since each of the distribution's peaks has to be characterized separately in terms of microstructure. This requires an additional computation step identifying the dODF maxima.

A rotation invariant scalar measure similar to FA was introduced by Tuch and colleagues (D. S. Tuch, 2004). They call this metric the *generalized fractional anisotropy* (GFA), as it extends the idea of characterizing the overall anisotropy to more generalized geometries. It is defined analogously to the tensor FA:

$$\begin{aligned} GFA &= \frac{\sigma(\Psi)}{\mathbb{E}(\Psi)} \\ &= \sqrt{\frac{n \sum_{i=1}^n (\Psi(u_i) - \langle \Psi \rangle)^2}{(n-1) \sum_{i=1}^n \Psi(u_i)^2}}, \end{aligned} \tag{4.42}$$

where  $\langle \Psi \rangle$  stands for the average dODF value, which is constant in case of the c-dODF and p-dODF. This metric basically describes the variation of the dODF.

The GFA can be used for the characterization of results from arbitrary local models, like for example spherical deconvolution (see Chapter 4.5.4). However, the GFA value differs for each local model. This is also the case for each of the dODF formulations. It behaves very similar to FA. In the work of Gorczewski and colleagues (Gorczewski et al., 2009) it even could be shown, that a linear dependence between FA and GFA exists.

An extension of GFA to the separate peaks of the dODF has been proposed by Ghosh and Deriche (Ghosh and Deriche, 2011). This metric is called the *peak fractional anisotropy* (PFA) and describes the anisotropy of each peak separately. This approach then can be extended to a total PFA, which is calculated as a weighted sum of the separate PFA values.

In case of using a metric derived from the dODF for the characterization of the microstructure it should always be kept in mind, that the dODF strictly only models the diffusion and not the microstructure. Any connection to the fiber anatomy should be formed using an explicit model.

#### **4.4.7 Advantages and Limitations of the dODF**

The great advantage of the dODF in comparison to the diffusion tensor is its ability to resolve more complex fiber geometries. Furthermore no prior assumptions are necessary for estimation of the dODF, it therefore is classified as a model free approach. In case of the c-dODF and the p-dODF explicit assumptions are made on the radial profile of the diffusion propagator. Other advantages of these methods are the computation speed and that only about 60 directions have to be measured for an adequate reconstruction of the dODF (Khachaturian et al., 2007). On the other hand this model only describes the diffusion propagator and thereby only implicitly models the underlying fiber microstructure. Therefore the classification as model free is a little bit misleading as an implicit model is then used for interpretation, without explicitly being stated. This is to be seen extremely cautious when not comparing dODF based properties between each other, but formulating results in terms of properties of the underlying microstructure.

### **4.5 Fiber Orientation Density Function**

#### **4.5.1 Introduction**

All approaches mentioned so far are models of the diffusion propagator and do not need an explicit model of a fiber response function (signal of a single collinear fiber population). The connection to the microstructure is given implicitly and often used in a non-formularized fashion during the interpretation of the results in terms of microstructure and its properties. A method which leads to an explicit model of the fiber configuration in each voxel is spherical deconvolution (D. C. Alexander, 2005a; Dell'Acqua et al., 2007; Kaden et al., 2007; Tournier et al., 2007, 2004). It translates the direction dependent signal attenuation into a *fiber orientation density function* (fODF). It is measured in the unit  $(mm^3rad)^{-1}$ .

This method is based on the spherical convolution theorem introduced in Chapter 3.7. In the spherical deconvolution model the signal is seen as constituted by the signal associated

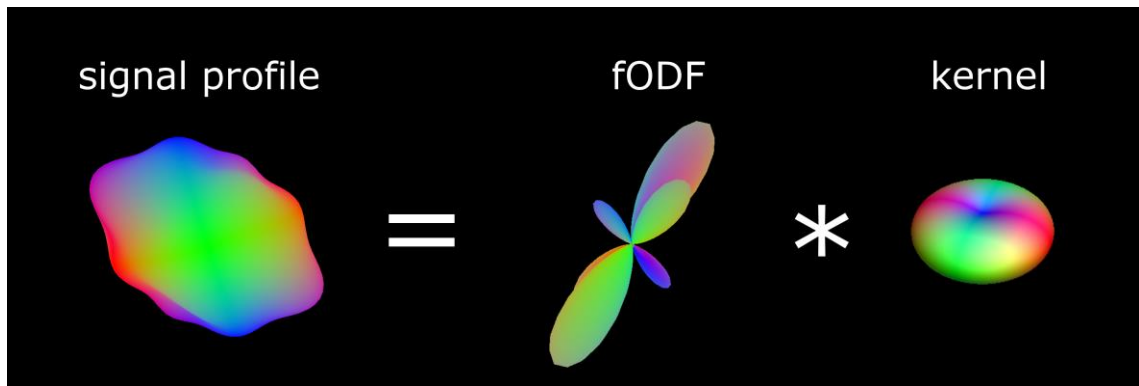


Figure 4.5: The principle of spherical deconvolution. In spherical deconvolution the signal is assumed to be constituted by the convolution of the signal of a single fiber (kernel) with a fODF. In theory the fODF is a sum of Dirac delta functions. Since spherical deconvolution is formulated in the space of spherical harmonic functions the fODF is blurred and appears rounder.

to a single fiber or group of coherently oriented fibers (convolution kernel), which is convolved with a fODF. This is visualized in Figure 4.5.

This is a model dependent method, as it requires the model of the convolution kernel. The resulting fODF greatly depends on the estimated model of the single fiber response. For the calculation of the kernel several approaches have been introduced. An overview of the different convolution methods and a common framework can be found in the work of Jian and Vemuri (Jian and Vemuri, 2007).

The fODF calculated from spherical deconvolution can be understood as an angular spatial distribution of the fiber density. That means for a given direction it represents the fiber density with regards to the voxel of interest.

In this chapter I will focus on the spherical deconvolution method introduced by Tournier and colleagues (Tournier et al., 2007, 2004) especially *constrained spherical deconvolution* (CSD) (Tournier et al., 2007). CSD was used for the fitting of the Bingham function (Chapter 5) and is implemented in the software package MRtrix (Tournier et al., 2012).

## 4.5.2 Math of Spherical Deconvolution

Spherical deconvolution can be seen as a generalization of mixture models. In mixture models one assumes a discrete number of fiber populations  $n$  for each voxel. In spherical deconvolution the problem of having to assume a number of fiber populations within a voxel is circumvented by using a continuous distribution of fibers rather than a discrete number to describe the microstructure. This is done, as described by Tournier and colleagues (Tournier et al., 2004), by generalizing the discrete problem:

$$\frac{S(\theta, \phi)}{S_0} = \sum_{i=1}^n f_i R(A_i(\theta_i, \phi_i)(\theta, \phi)). \quad (4.43)$$

The variable  $R(\theta)$  stands for the axially symmetric response function, which is defined to be aligned with the z-axis and rotated onto the direction of the fiber population  $\vec{d}_i = (\theta_i, \phi_i)$  by the rotation operator  $A_i$ . The value  $f_i$  gives the volume fraction of the  $i$ -th fiber bundle in the voxel.

In the continuous case this can be expressed as the convolution of the kernel function  $R(\theta)$  with the fODF  $Y(\theta, \phi)$ :

$$\frac{S(\theta, \phi)}{S_0} = (Y \otimes R)(\theta, \phi). \quad (4.44)$$

If one assumes  $R, Y \in L^2(S^2)$ , then the convolution theorem (3.32) states:

$$\frac{\hat{S}_l^m(\theta, \phi)}{S_0} = \sqrt{\frac{4\pi^2}{2l+1}} \hat{Y}_l^m(\theta, \phi) \hat{R}_l^0(\theta, \phi). \quad (4.45)$$

Hereby the expression  $(\cdot)_l^m$  stands for the corresponding coefficients of order  $l$  and degree  $m$  of the SH expansion. Assuming a single fiber being present in certain voxels, i.e. the fODF in these voxels corresponding to a Dirac delta function, one can estimate the response function  $R$  from the signal attenuation  $E$  in areas of a single z-aligned rotationally symmetric fiber population. This is done by applying the Funk-Hecke theorem (3.29) to describe the Dirac delta function in terms of a SH expansion. The coefficients of the response function can then be estimated by calculation of:

$$\hat{R}_l^0(\theta, \phi) = \sqrt{\frac{2l+1}{4\pi^2}} \frac{\hat{E}_l^0(\theta, \phi)}{P_l(0)}. \quad (4.46)$$

The calculation of the fODF coefficients  $\hat{Y}_l^m$  then amounts to:

$$\frac{\hat{S}_l^m(\theta, \phi)}{S_0} = \hat{Y}_l^m(\theta, \phi) \frac{\hat{E}_l^0(\theta, \phi)}{P_l(0)}. \quad (4.47)$$

In order to convey the fODF with more meaning it is desirable to scale the signal attenuation to that of a single fiber. This is done by dividing the kernel's signal attenuation by the corresponding voxel fiber density. This can be estimated from histological work, for example by Aboitiz and colleagues (Aboitiz et al., 1992). If one deconvolves the diffusion



signal from a particular voxel using the kernel estimated as described, the resulting fODF represents (an estimate of) the angular fiber density in the respective voxel to the extent to which the fibers in that voxel are similar to the average kernel voxel fiber. Without this normalization not the true fiber density is described but rather the density is measured in the unit of kernel fibers.

### 4.5.3 Calculation from the measured signal

In practice the calculation of the fODF from the measured signal is fairly straightforward. It requires a vector  $\vec{R}$  of the coefficients of the response of a single fiber. As this is assumed to be z-aligned and symmetric only the values for degree  $m = 0$  are required. This kernel is calculated using the pseudoinverse of the SH base. The symmetry is guaranteed either by generating the signal from a symmetric diffusion tensor representing the single fiber population or by disregarding the coefficients for degree  $m \neq 0$  and using the measured signal in an area where the populations are known to be relatively collinear and rotating the signal to z-alignment. For such a kernel signal vector  $\vec{S}_{kern}$ , the response amounts to:

$$\vec{R} = \frac{\vec{S}_{kern}}{S_0} (B^T B)^{-1} B^T, \quad (4.48)$$

In case of using the measured signal for the kernel estimation, the population has to be aligned with the z-axis. This is done by rotation of the gradients in the corresponding voxel on the basis of a tensor fit. Therefore an individually calculated base has to be used for each voxel.

After estimating the response the fODF  $\Upsilon$  is calculated by applying the discretized version of equation (4.47):

$$\Upsilon_j = P_l(0) \frac{s_j}{r_{j_0}}, \quad (4.49)$$

where  $P_l(0)$  is the Legendre polynomial, defined in equation (3.28), and  $r_{j_0}$  is the kernel coefficient with index  $j_0 = \frac{1}{2}(l^2 + l + 2)$  of the vector  $\vec{R}$ . The values  $s_j$  are the SH coefficients of the attenuation signal's SH expansion with index  $j = \frac{1}{2}(l^2 + l + 2) + m$ . The coefficients of the SH representation are calculated in terms of the vector  $\vec{s}$  using the vector of measured signals  $\vec{S}$  and the corresponding voxel's  $b_0$  signal  $S_0$ :

$$\vec{s} = (B^T B)^{-1} B^T \frac{\vec{S}}{S_0}, \quad (4.50)$$

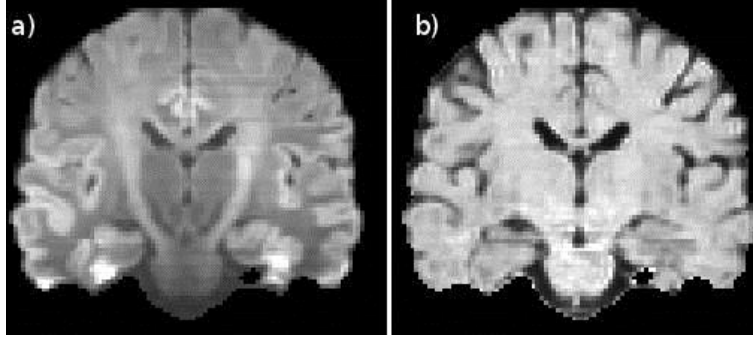


Figure 4.6: Effect of the CSD normalization. On the left (a) the first coefficient of the CSD is shown after normalization. On the right (b) the non-normalized image is shown.

Using a diagonal matrix  $D$  defined as follows, the calculation of the fODF can be written in terms of a matrix vector multiplication.

$$D = \begin{pmatrix} \frac{P_1(0)}{r_1} & & 0 \\ & \ddots & \\ 0 & & \frac{P_l(0)}{r_{j_0}} \end{pmatrix}. \quad (4.51)$$

The deconvolution can then be written as:

$$\vec{Y} = D\vec{s}, \quad (4.52)$$

where  $\vec{Y}$  is the vector of SH coefficients representing the fODF. This calculation of the fODF  $\vec{Y}$ , however, leads to problems in terms of negative value peaks (negative lobes) arising due to the oscillating nature of the SH base functions. For suppressing these, several strategies are employed. These reach from using a regularization vector for suppressing higher orders (Tournier et al., 2004), employing nonlinear fitting algorithms with a positivity boundary condition (Schwab et al., 2012) or fitting the fODF on a grid, on which positivity is iteratively enforced (Patel et al., 2010).

An approach introduced by Tournier and colleagues (Tournier et al., 2007) is to minimize the occurring negative lobes iteratively while at the same time minimizing the residuum of the reconstruction. This method is called CSD and is implemented in MRtrix (Tournier et al., 2012). For describing this method I need to introduce two base matrices  $P$  and  $N$ . These are generated by computing the attenuation signal for a tessellation on the sphere using a base  $B$  and then dividing this base into compartments. The division is based on the value of the reconstructed attenuation signal at the points on the tessellation. By introducing a threshold the base  $B$  is divided. The points which have a value above the threshold are used

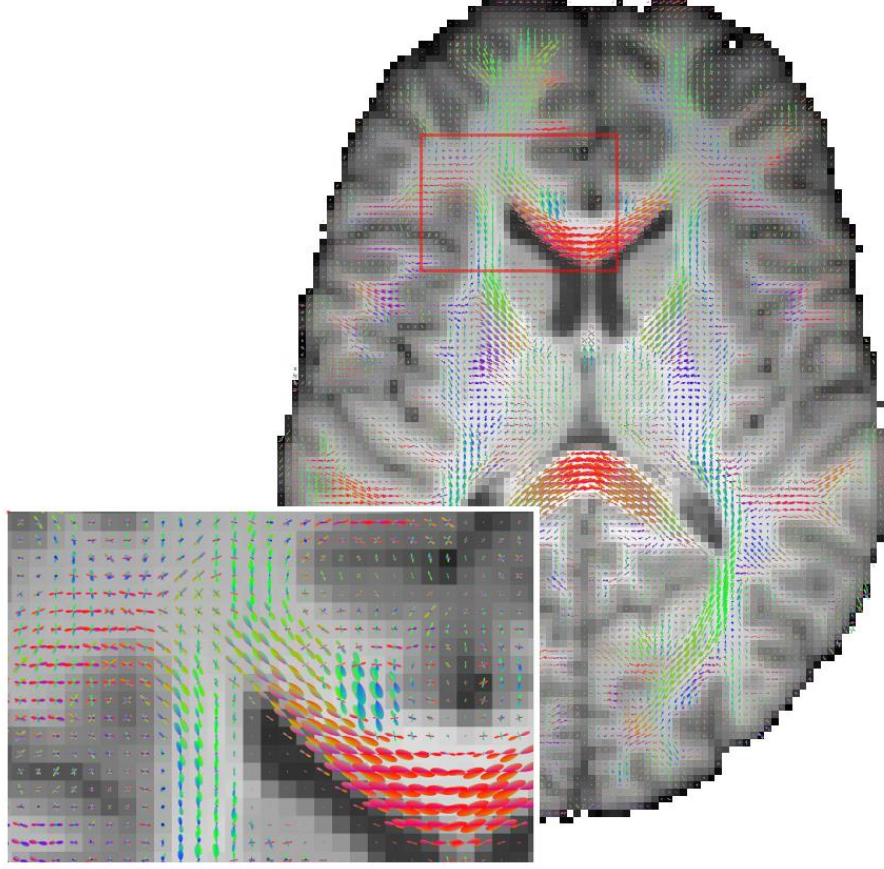


Figure 4.7: fODF from spherical deconvolution mapped onto the brain. The glyphs are shown using an axial slice. As can be seen in the highlighted section, the fODF can discern crossing voxels, from non-crossing voxels.

for building the base  $P$ , while the others are used for generating the base  $N$ . This method at once minimizes the residuum of the signal reconstruction and the error introduced from negative lobes:

$$\arg \min \left\{ \left\| \begin{pmatrix} P \\ \alpha N \end{pmatrix} \bar{\mathbf{Y}} - \begin{pmatrix} \hat{\mathbf{S}} \\ \frac{\mathbf{S}_0}{0} \end{pmatrix} \right\|^2 \right\}, \quad (4.53)$$

where  $\bar{\mathbf{Y}}$  is the vector of the fODF coefficients, which is subject to the optimization and  $\alpha$  is a parameter weighting the non-negativity constraint with the residuum of the signal reconstruction. For an exemplary dataset the fODF is visualized in Figure 4.7.

Note that the MRTrix software package (Tournier et al., 2012) applies the CSD to the diffusion weighted signal rather than the signal attenuation. This introduces a weighting of

the fODF by the ratio between the  $b_0$  (or  $T_2$ ) signal ( $S_0(voxel)$ ) in the respective voxel and the average  $b_0$  signal ( $S_0(kernel)$ ) in the kernel. Hence, the results must be corrected by a factor resulting from the quotient of the two ( $S_0(kernel)/S_0(voxel)$ ). The effect of the normalization is shown in Figure 4.6.

#### 4.5.4 Metrics from Spherical Deconvolution

Deriving metrics from the fODF is one of the most straightforward ways of finding connections to the underlying fiber microstructure. However, for the fODF the same problems concerning the SH representation and the multi-modal distribution structure arise as for the dODF (described in Chapter 4.4.6).

An easily derived metric comes from the description of the fODF in terms of an SH expansion. As shown in Chapter 3.5 the first coefficient of the fODF describes the integral of the fODF over the surface of the sphere. Integrating an angular spatial density in such manner leads to a spatial density. In case of the fODF this is the voxel-wise fiber density, which can be translated to a fiber count by multiplication with the voxel size.

A metric that can also be used for describing the anisotropy of the fODF is the GFA. However the concept of anisotropy is lost when moving from diffusion to a fiber configuration. In that case the GFA rather describes the structural variance of the underlying angular-spatial fiber density, which is not a very intuitive metric easily related to the microstructure.

A metric describing the underlying structure which is derived from spherical deconvolution is the apparent fiber density (Raffelt et al., 2012), which uses the maximum peak length of the fODF as a bundle specific metric. The quantity described, however, is not the fiber density but actually the angular fiber density within the peak's maximum direction, which for sufficiently high b-values is closely related to the apparent fiber density. An explanation of the connection is given in the work of Raffelt and colleagues (Raffelt et al., 2012). With a different scaling the same metric is used in the work of Dell'Acqua and colleagues (Dell'Acqua et al., 2012). Here it is called the *hindrance modulated orientational anisotropy* (HMOA) and calculated by putting the length of the peak into relation to a reference amplitude. This metric derived as a parameter of the Bingham function fitted to the fODF is used as described in Chapter 6. Here it is defined as the bundle specific *maximum angular fiber density* ( $AFD_{max}$ ).

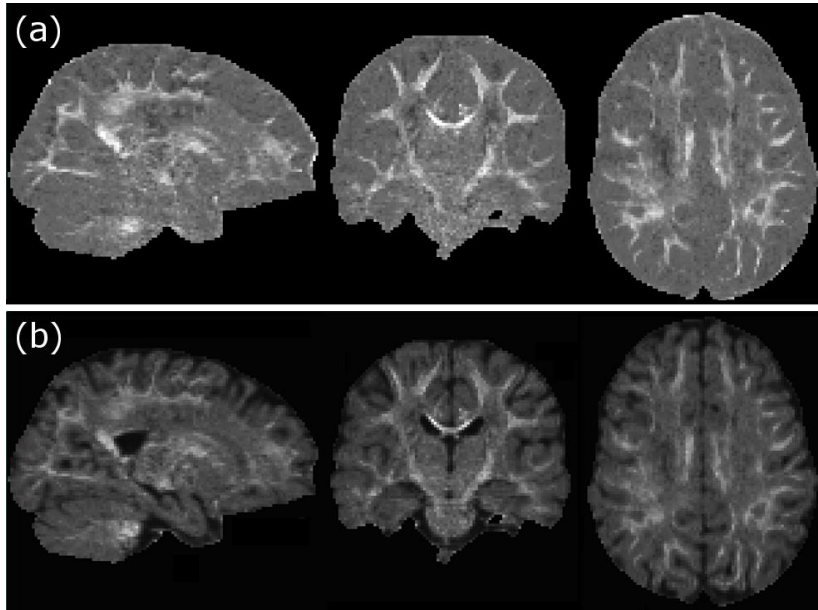


Figure 4.8: Map of integral over the negative lobes. Figure (a) shows the absolute value of integral over negative lobes, while figure (b) shows the relative value of integral over negative lobes. The highest values occur in areas where only a single fiber population is present.

### 4.5.5 Problems arising in Spherical Deconvolution

When working with the local model of spherical deconvolution and deriving metrics from the fODF, I came across several problems resulting from the SH representation of the fODF.

The most prominent of these problems is the occurrence of negative lobes. It stems from the truncation of the SH series expansion. These also appear for the dODF but are more prevalent in the fODF as it intrinsically has sharper peaks.. Since the functions used for fitting are oscillating functions, the truncation of the spherical expansion leads to ringing artifacts in terms of negative lobes in the approximation of the (strictly positive) fODF. Together with the negative lobes spurious positive peaks appear. This is compensated to a certain degree by CSD, however, the regularization influences the shape of the fODF and may lead to regularization artifacts. The danger here lies in the misrepresentation of peaks, but also, the regularization may cause further spurious positive peaks to arise as well as virtually reducing the order of the fODF's SH expansion which leads to a loss of the measured information that is integrated into the fODF. The spurious positive peaks are particularly dangerous, as these peaks cannot be discerned from peaks caused by the underlying microstructure. The stability and the occurrence of spurious peaks may also be improved by using the damped Richardson-Lucy deconvolution (Dell'Acqua et al., 2007; G. D. Parker et al., 2012).

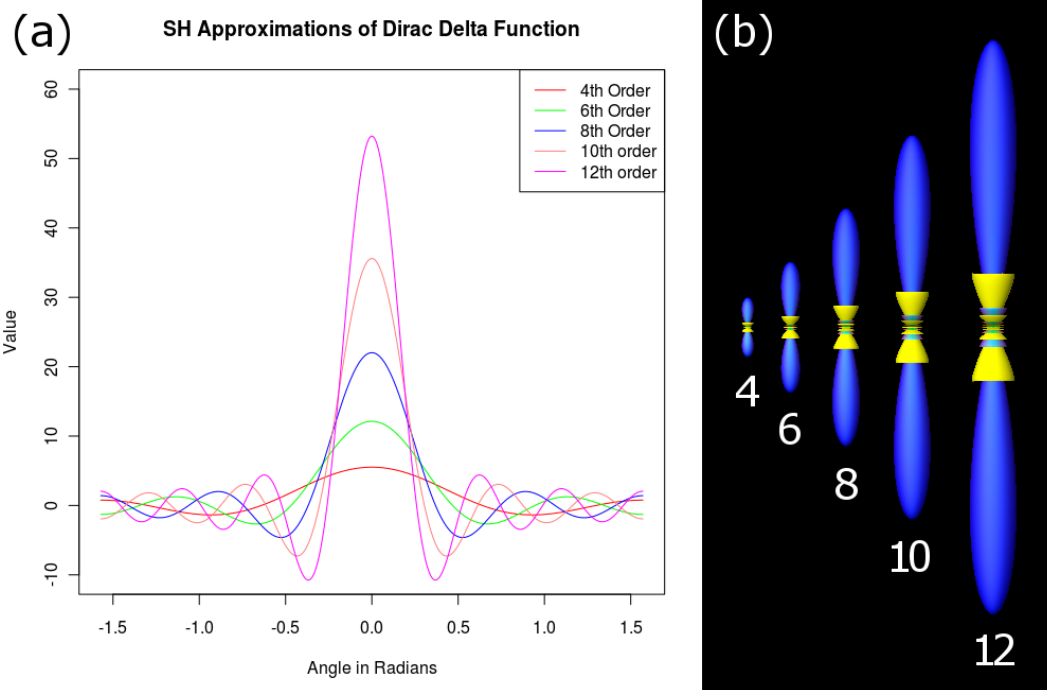


Figure 4.9: Approximation of Dirac delta function. The number of negative lobes of the Dirac delta function as well as the corresponding spurious positive peaks can be seen in (a). The higher the order is, the better the Dirac delta function is approximated, but the spurious peaks and negative lobes significantly increase as well. In (b) one sees the corresponding CSD glyphs. The glyphs seem much larger for higher orders. However the integral of the CSD over the sphere is constant. The glyphs are perceived as larger due their increase in volume.

For further analysis of the influence of the negative lobes the maps shown in Figure 4.8 were generated. In these I show the integral of the fODF's negative lobes over the unit sphere. As can be seen negative lobes arise mainly in areas where the kernel is similar to the observed signal. In other words, the largest errors occur in areas where only a single fiber population is present, causing a sharp Dirac delta like fODF. The sharpness of the fODF is governed by the SH expansion order and the shape of the convolution kernel.

I investigated the approximation of the Dirac delta function and its negative lobes as well as spurious peaks. These depend strongly on the deconvolution order. I investigated the shape of the Dirac delta approximation in terms of Legendre polynomials. The results can be seen in Figure 4.9. As can be seen the Dirac delta SH expansion introduces severe ringing artifacts, according to the SH order used for the approximation. These ringing artifacts manifest as positive and negative spurious peaks.

A further aspect of the SH representation of the fODF is that the truncation of the SH expansion smoothes the expanded function. This leads to the description of the fODF in

terms of rounded lobes. However, in theory the fODF is a sum of sharp impulse functions (Tournier et al., 2004). The effect of the smoothening on the shape of the reconstructed fODF is difficult to assess quantitatively, especially since these effects are additional to the effects induced by the kernel mismatch, which I discuss later on. As can be seen from Figure 4.9 the SH expansion order plays a large role in the sharpness of the reconstructed delta function. If one classifies the opening angle of the Dirac delta function in a similar way as described in Chapter 6.2, then one can see that the minimum opening angle is  $14^\circ$  for an 8<sup>th</sup> order reconstruction and  $17^\circ$  for a 6<sup>th</sup> order reconstruction. These hard boundaries are very important to be kept in mind when dealing with metrics derived from the fODF describing the spread of fibers (such as the metrics described in Chapter 6). As soon as one is interested in the shape of bundles with an opening angle below the minimum opening angle, one needs to use a higher order SH expansion and therefore need measurements using more gradient directions. Finding an optimal solution to this problem would require the introduction of a spherical sampling theorem, which gives the connection between the highest frequency which can be reconstructed and the number of samples.

Higher numbers of measurements alone, however, do not solve the shape resolution problem. This is due to higher order reconstructions introducing a stronger need for regularization, as the problem of reconstructing the fODF becomes more unstable the more degrees of freedom are added. In other words, the regularization artificially limits the order used for reconstruction. Using a low effective order due to strong regularization leads to the reconstructed Dirac delta function is again not represented appropriately.

Overall the main problem of the fODF reconstruction seems rooted in the reconstruction of Dirac delta like functions. An approach to avoid these problems during the fitting process is presented by Dell'Acqua and colleagues (Dell'Acqua et al., 2010), who use an approach which is not SH expansion based during calculation, introducing the SH expansion after computation of the results. All of this calls into question seeing the SH functions as a natural way to decompose signals on the sphere (Descoteaux, 2010) when main features of interest are the peaks of the SH approximated functions.

In context of the problems arising in local modeling we should ask ourselves if there may be better alternatives to represent spherical data, especially when only having measured a sparse representation of a function of interest. An approach to this problem might be the use of a matching library basis for the generation of the fODF. This would have to be designed such, that the matching library basis representation of the fODF can be estimated from the 60 diffusion directions and that sharper peaks can be reconstructed.

Problems do not only occur in terms of negative lobes. As Dell'Acqua and colleagues describe in their work (Dell'Acqua et al., 2012), mismatch of the kernel shape, that is a

difference between the kernel response and the true fiber signal, leads to blurring of the fODF.

Basically two types of mismatch concerning the kernel of the fODf can occur. Either it has a too wide or a too sharp kernel function. Since the reconstruction algorithm is linear with regard to scaling a mismatch in scaling is not of concern. If one uses a too narrow response function, that is a too narrow signal for a single fiber, then basically more fibers are needed to explain the observed signal. This leads to a wider fODF. In case of using a too wide response function the fODF gets sharper. Furthermore this sharpening can lead to inclusion of multiple populations within a single peak, which, with the correct kernel, could have been identified as separate populations.

The kernel mismatch occurs intrinsically to the spherical deconvolution methods. This is due to one of the base assumptions of the spherical deconvolution method, which is that the shape of the response function is constant over the whole brain. This assumption, however, is unlikely to be correct, as the measured signal varies slightly in amplitude throughout the brain and the structure of a single fiber probably varies as well. The use of the signal attenuation leads to suppression of the signal amplitude's variance. However, differences in the microstructural properties may lead to a local difference of the true response. One would therefore need to at once estimate the kernel as well as the fODF. This is not possible in practice, as this could only be solved by inputting external information on the structure, which one is looking to reconstruct. In the work of Parker and colleagues they discuss the differences between the reconstructed fODFs for different kernels (G. D. Parker et al., 2012).

It should be noted that all of these problems also arise in the dODF formulation (see Chapter 4.4) in two ways. First the resulting dODF is also subject to the smoothing artifacts due to truncation of the SH expansion. Second the highly nonlinear influence of the kernel on the fODF also plays a role for the dODF, where the kernel is not formulated explicitly. Instead the changes in dODF are interpreted in terms of microstructural properties without this highly complex connection. Therefore on the surface these problems seem inherent to the fODF reconstruction, even though they play a role for the SH expansion based computation of the dODF as well. A method to connect dODF and fODF was given by Descoteaux (Descoteaux, 2010). In his work he applies the deconvolution framework to the dODF, using the dODF of a single fiber as local model. This method again formularizes the connection between fibers and diffusion.

### **4.5.6 Crossing Angle Distribution Derived from CSD**

A question which was strongly discussed between Wedeen and colleagues (Wedeen et al., 2012a, 2012b) on the one side and Catani and colleagues (Catani et al., 2012) on the other



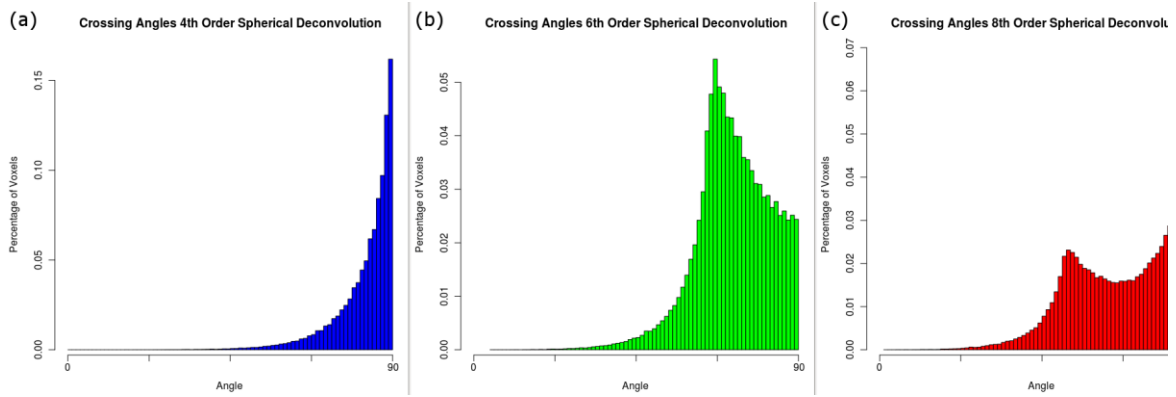


Figure 4.10: Connection between the crossing angle distribution and the SH reconstruction order. As can be seen the distribution's shape and peak vary greatly depending on the spherical deconvolution order (90° for 4<sup>th</sup> order, 70° for 6<sup>th</sup> order and 50° as well as 90° for 8<sup>th</sup> order).

side, was the question of the distribution of the angles at which the fibers in the brain cross. Wedeen and colleagues claim that 90° crossings are prevalent, while Catani and colleagues claim the crossing angles to be more evenly distributed. Methodology wise, Wedeen and colleagues use DSI, while Catani and colleagues investigated the question using a dODF.

I investigated the crossing angle between the largest two peaks of the fODF derived from CSD, thresholding the second peak at 10% of the largest peak. I calculated the results for 4<sup>th</sup>, 6<sup>th</sup> and 8<sup>th</sup> order SH expansions. The results are shown in Figure 4.10. The main result is that the distribution of crossing angles is strongly dependent on the order of the SH expansion.

In case of a 4<sup>th</sup> order approximation, the crossings occur mainly at close to 90° angles. An increase of the order shifts the angles closer to 60° which is the angle at which separate bundles can be discerned using a 6<sup>th</sup> order expansion additionally only a low number of 90° crossing can be observed. In case of using an 8<sup>th</sup> order CSD one finds both a peak at 50° as well as a peak at 90°. This indicates that the spherical harmonic base plays a large role in the determined crossing angle.

In the 4<sup>th</sup> order case one can detect crossings mainly at large angles, due to not being able to completely resolve small crossing angles. Additionally the Dirac delta function has a spurious peak at 90° (as can be seen in Figure 4.9), which may manifest in terms of incorrectly found fiber populations at this angle. The spurious peak of the Dirac delta function shifts to about 68° for a 6<sup>th</sup> order SH approximation. At the same time no spurious peak occurs at 90°. This again corresponds to the peaks in the crossing angle distribution. When using 8<sup>th</sup> order the oscillations of the SH functions cause two spurious peaks in the Dirac delta approximation. These are at 90° and around 50° which again correspond to the peaks in the crossing angle distribution. This leads to the conclusion that the crossing angle

distribution is strongly biased by the deconvolution process and correlated to inaccuracies in the approximation of the Dirac delta function. Since the fODF in many voxels (about 30%-60% (T. E. J. Behrens et al., 2007)) can be approximated by a Dirac delta function it can be hypothesized that the errors of the Dirac delta function approximation are responsible for the behavior of the crossing angle distribution.

### **4.5.7 Advantages and limitations**

In the following I will summarize the advantages and limitations of the local model spherical deconvolution. The greatest advantage of this model compared to the diffusion propagator based models is that it directly models tissue microstructure. It is able to resolve crossing configurations without requiring prior knowledge on the number of fibers present within a voxel and can be computed relatively easy, due to its linear nature. Furthermore it only requires about 60 directions to give a useful approximation of the fiber structure in terms of and fODF.

The greatest disadvantage of this method is the need for formulating an explicit model on the response of a single collinear fiber population. Furthermore, as discussed in Chapter 4.5.5, several problems arise due to the SH approximation. These include, but are not limited to estimating maximum approximation order, arising of negative lobes, regularization issues and concealing of directional peaks. The assumption of a constant kernel is not necessarily accurate as well as the Gaussian modeling of the radial profile of the measured signal, which is used implicitly (Assemlal et al., 2011).

As showed in Chapter 4.5.6 the approximation error of the Dirac delta function is strongly correlated with the errors in the CSD result and especially to errors in the crossing angle estimation. Further analysis would be necessary to determine the exact nature of the connection between the Dirac delta function approximation errors and the fODF reconstruction.

## **4.6 Conclusion**

In this chapter I first introduced the diffusion propagator, then derived the diffusion tensor and the dODF from this fundamental property of diffusion. I discussed the linear dODF approach (D. S. Tuch, 2004) and introduced a framework common to the c-dODF (Tristán-Vega et al., 2010) and p-dODF (Aganj et al., 2010) approach. Afterwards I introduced spherical deconvolution as an approach to model the fODF which is connected to the fiber architecture more explicitly and discussed the problems arising from the SH representation of the fODF. For each of the introduced local models I showed their mathematical definition, the process of calculating the model from the signal, some exemplary metrics and discussed

their advantages and disadvantages. For more information on these and further local models see the work of Assemlal and colleagues (Assemlal et al., 2011).

If I view the models discussed in this chapter under the aspect of clinical feasibility, then DTI is still one of the most useful methods. This is mainly due to the low acquisition time. However, this shorter time comes at the cost of a loss of information and therefore inaccuracies in the reconstructions. Especially when investigating the microstructural arrangement within a voxel, it is desirable to use a large number of diffusion gradients. However, a high number of gradients usually come at the expense of the spatial resolution, due to limited scanning time. For exploring the microstructural arrangement, high spatial resolution is also necessary. If I use a too low spatial resolution, then I get a large amount of partial volume effects. These effects describe the influence of structurally diverse microarchitectures on diffusion in the same voxel. It occurs mainly in regions close to macrostructural tissue boundaries, as observed for example at the boundary of the white matter and the CSF in the corpus callosum.

One of the main applications of the local models is tractography, which is the process of extrapolating long range connections from the local fiber arrangement. For tractography again one not only wants a large number of diffusion gradients in order to correctly identify the diffusion directions, but also a high spatial resolution, since tractography can be seen as solving an integration problem. The spatial resolution is the basis for calculating a lower boundary on the step width. Tractography requires accurate local models, as errors propagate when tracking. This also shows that the dODF and fODF and especially their SH expansion can lead to problems in tracking, since in tractography the shape of the corresponding function is often used as an indicator of fiber spread. The SH representation can, however, introduce an error in the fitted shape. This is one of the reasons that leads to questioning the use of SH expansion based local models and incentivizes deriving local models on a different basis. Since most of the difficulties and their extent were discovered, due to using the spherical deconvolution model, this work is still based on spherical deconvolution.

Additionally I mainly use the local model of spherical deconvolution due to the intrinsic connection between the fODF and the fiber microarchitecture. This connection is fundamental as the goal of this work is to discuss parameterizations of local models in terms of metrics which can specifically be related to certain changes in the tissue architecture.

# 5 Bingham Fit

---

## 5.1 Introduction

One of the main advances of dMRI is the ability to investigate the brain's microanatomy in-vivo. For the interpretation of the results it is desirable to have access to models, which can be directly related to the anatomy in terms of microstructural properties. As often more than one fiber population is present in a voxel it would be especially desirable to characterize these bundles separately.

Models which inherently have these properties are multi-tensor models (D. C. Alexander, 2005b; Makris et al., 2002). These allow for multiple coherent fiber bundles within one voxel and describe the contribution of each fiber population in the voxel in terms of a diffusion tensor, which is an easily parameterized well known model. For a given number of tensors per voxel these models are very reliable. However, a generalized model allowing any number of diffusion tensors leads to numerical problems. In the work of Scherrer and Warfield (Scherrer and S K Warfield, 2010), it has been shown that these problems stem from the collinearity of the multi-tensor parameters. Therefore a single b-value is insufficient for estimating the full model of multiple tensors. Additionally the tensor describes diffusion, while this work aims at modeling fiber properties.

A different approach to the problem of separately characterizing the fiber bundles present in a voxel is choosing a more complex local model, which can properly assess the microstructure and then to extract features from this model, which accurately represent the properties of single fiber populations. The two local models which come to mind for this task are dODF and fODF. Both of these are usually represented by analytical SH functions. In this parameterization, the parameters do not usually bear any direct meaning, which makes direct interpretation in terms of fiber properties, such as mean directions and spreading of the particular fiber populations, difficult (as discussed in Chapter 4). Additionally, the SH representation does not allow for separate characterization of the different fiber bundles present in one voxel, since these are part of the multimodal distribution structure represented by the SH. Therefore, a different parameterization is desirable for partitioning the fODF into contributions from individual underlying fiber populations and providing interpretable measures, which might be used as biomarkers for anatomical properties.

As discussed in the chapter on local modeling (Chapter 4), methods describing the diffusion do not explicitly model microstructural fibers properties, but rather implicitly describe them in terms of reduced diffusion perpendicular to the main fiber directions. As approach to this problem the fODF was chosen as base model, from which to extract the microstructural properties. The fODF is assumed to be constituted by the overlaying of multiple coherent fiber populations, leading to peaks in the multimodal distribution structure of the fODF. Since the true angular distribution of fiber densities within a single bundle is not known, they were approximated using the Bingham distribution as spherical equivalent to the normal distribution. This use of the Bingham distribution to describe coherent fiber bundles has been discussed previously. For example, Seunarine and colleagues (Kiran K Seunarine et al., 2007) used the Bingham distribution for describing the uncertainty of the fiber direction for its use in tractography. Kaden and colleagues (Kaden et al., 2007) proposed fitting a multi-compartment model composed of Bingham distributions into the measured data. In contrast in this work the Bingham distribution is used as model of a single fiber and fit to the peaks of the fODF.

In this chapter I will first introduce the Bingham distribution and describe the related Bingham function, used for describing the fODF peaks. Afterwards I will describe the fitting problem and show how to linearize the fitting process. Finally I will discuss the relation between the Bingham function and the diffusion signal, introducing a method to calculate the diffusion signal for each of the fiber bundles in a voxel separately and introduce a tracking method based on the fitted Bingham functions. The work within this chapter is an original contribution and has been submitted (Riffert et al., 2013).

## 5.2 Bingham Distribution

The Bingham distribution was introduced by Christopher Bingham (Bingham, 1974) for the purpose of treating bimodal elliptical data. It is an antipodally symmetric probability distribution with an elliptical cross-section and can be constructed by constraining multivariate normal distributions to lie on the surface of a unit sphere. It can be described by the following density function:

$$b(\vec{u}) = \frac{1}{F_k} \exp(-k_1(\vec{\mu}_1\vec{u})^2 - k_2(\vec{\mu}_2\vec{u})^2), \quad (5.1)$$

where  $\vec{u}$  is a point on the sphere. This function has two maxima, which due to the antipodal symmetry are located on opposite sides of the sphere. The cross-section of this peak is an ellipse. The spread and the ovality of the profile of the Bingham distribution are characterized by the concentration parameters  $k_1$  and  $k_2$  ( $k_2 \geq k_1$ ). The larger the

concentration parameters are, the sharper the peak becomes. The directions of the Bingham distribution are described by its direction vectors  $\vec{\mu}_1$  and  $\vec{\mu}_2$ , which characterize the axis of the oval profile. Hereby  $\vec{\mu}_1$  is the major axis and  $\vec{\mu}_2$  is the minor axis. The distribution's main orientation, i.e. the direction of the distribution's mean ( $\vec{\mu}_0$ ), is orthogonal to  $\vec{\mu}_1$  and  $\vec{\mu}_2$ . The distribution's normalization constant  $F_k$  is the confluent hypergeometric function of matrix argument. This constant can be computed by integrating the exponential part of the equation ( $\exp(k_1(\vec{\mu}_1 \vec{u})^2 + k_2(\vec{\mu}_2 \vec{u})^2)$ ) over the surface of the unit sphere. A more direct way of computing the confluent hypergeometric function of matrix argument is by means of Laplace approximations (Abramowitz and Stegun, 1964).

Since the Bingham distribution is used for the characterization of the peaks of the fODF it has to be ensured, that they are scaled to fit. As the fODF does not characterize a probability distribution, but an angular-spatial distribution of fibers, it is not necessarily scaled in such a manner that the Bingham distribution can be used for direct classification. Therefore a scaling parameter is introduced ( $c_{\text{scale}}$ ), which together with  $F_k$  defines the size parameter  $f_0 = c_{\text{scale}}/F_k$ . The size parameter corresponds to the maximum amplitude of the fODF within the peak currently characterized. In order to distinguish the probability distribution from the scaled version of the Bingham distribution I from here on refer to the scaled Bingham distribution  $\beta$  as Bingham function. It is defined as:

$$\beta(\vec{u}) = f_0 \exp(-k_1(\vec{\mu}_1 \vec{u})^2 - k_2(\vec{\mu}_2 \vec{u})^2) \quad (5.2)$$

This function is not a probability density function anymore, since it does not integrate to unit mass. For fitting an fODF peak with a Bingham function the five parameters  $f_0$ ,  $\vec{\mu}_1$ ,  $\vec{\mu}_2$ ,  $k_1$  and  $k_2$  need to be estimated.

## 5.3 fODF Fitting Process

Fitting the Bingham functions to the peaks of the fODF is a three step process. First the maxima of the fODF are identified using a spherical tessellation, second the Bingham function's direction vectors are fitted via an orientation matrix and third the concentration parameters are computed by solving a system of linear equations.

For fitting the fODF peaks with Bingham functions one first estimates the peaks of the fODF. For this the fODF is overlaid with a discrete search grid. Then a regular tessellation is constructed by iteratively refining a regular icosahedron resulting in 10,242 vertices and 20,480 faces. This corresponds to a spherical grid with an angular resolution of 2°. On this search grid points are identified, which are close to a local maximum. This is done by calculating the discrete local maxima on the search grid and using them as starting points for further optimization. The discrete local maxima of the fODF are found by comparison of

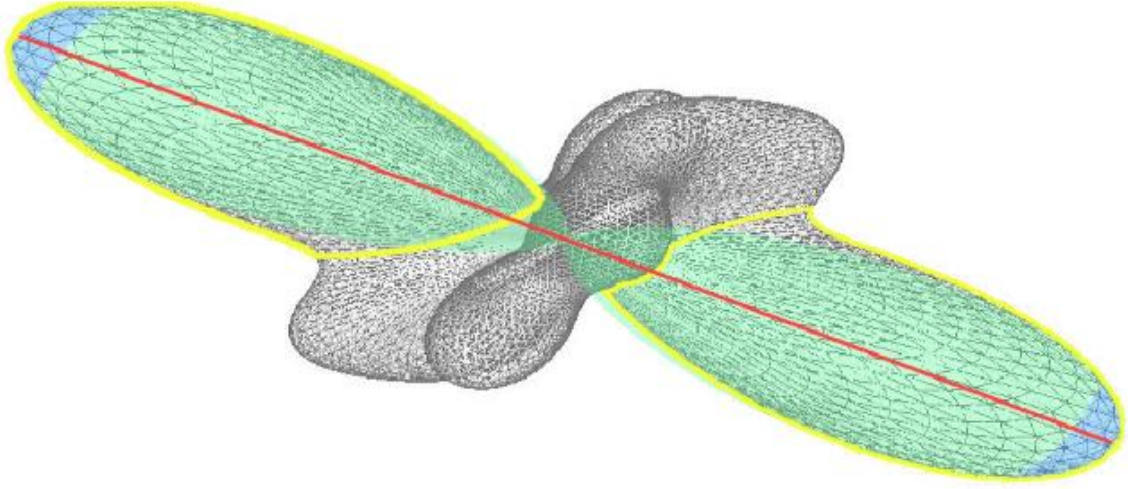


Figure 5.1: The Bingham neighborhood and fit. The fODF is shown in light grey. The maximum direction  $\vec{\mu}_0$  of its largest peak is visualized as the red line. The directions of the Bingham distribution (green) are fitted using a small neighborhood of the maximum direction. The points considered part of the peak are those within the yellow line. To ensure that the neighboring peaks do not have too large an impact, only the neighbors of first, second and third degree are considered, which corresponds to the points in the blue area.

the values of the fODF at grid points with the fODF values at neighboring points on the tessellation. I use the criterion, that a point on the search grid is a discrete local maximum if the fODF value at that point is larger than that at the neighboring points. In practice the fODF is computed at all grid points by matrix-vector-multiplication of the SH base, calculated for the tessellation points, with the SH expansion coefficients of the fODF.

Each of the discrete local maxima is assumed to represent a peak of the fODF. The Bingham functions main direction is taken to coincide with the direction of the respective fODF peak. Using the fODF maxima and a certain number of surrounding points (neighborhood) an orientation matrix is computed for each peak. Assuming  $\vec{p}_i = (x_i, y_i, z_i)$ ,  $i = 1 \dots N$ , to be neighboring points of the estimated discrete local maximum, the orientation matrix is defined as:

$$T = \begin{bmatrix} \sum x_i^2 & \sum x_i y_i & \sum x_i z_i \\ \sum x_i y_i & \sum y_i^2 & \sum y_i z_i \\ \sum x_i z_i & \sum y_i z_i & \sum z_i^2 \end{bmatrix} \quad (5.3)$$

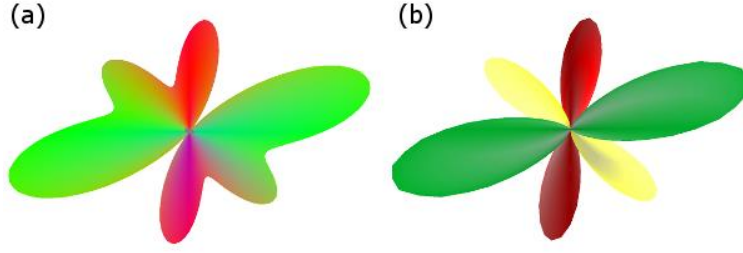


Figure 5.2: Fit of the fODF by Bingham functions. (a) fODF calculated by spherical deconvolution, (b) Bingham functions representing the separate peaks. The shape of each of the fitted Bingham functions closely corresponds to the fODF peak shape.

As shown in previous works (Onstott, 1980; Tanaka, 1999), the eigenvectors of  $T$  correspond to the principal directions of the Bingham function, fulfilling the maximum likelihood estimate for the points  $\vec{p}_i$ . However this estimation of the maximum direction is biased towards the points used in the estimation. Therefore the vectors  $\vec{\mu}_0$ ,  $\vec{\mu}_1$  and  $\vec{\mu}_2$  from the eigenvalue decomposition of  $T$  are used as starting points for a gradient descent optimization, to improve the estimates of the Bingham function directions.

The calculated values for the vectors  $\vec{\mu}_0$ ,  $\vec{\mu}_1$  and  $\vec{\mu}_2$  can then be substituted in equation (5.2). Since the maximum direction  $\vec{u} = \vec{\mu}_0$  is orthogonal to  $\vec{\mu}_1$  and  $\vec{\mu}_2$ , the scaling parameter is given by the fODF value at the maximum:

$$f_0 = \beta_{max} = \beta(\vec{\mu}_0). \quad (5.4)$$

Then the vector  $\vec{\beta}$  is defined. This vector is obtained by taking the logarithm of the fODF values at the  $N$  neighborhood points  $\vec{p}_i$ , which were scaled by the fODF's maximum value:

$$\beta_i = \left( \log \left( \frac{b(\vec{p}_i)}{b_{max}} \right) \right)_i. \quad (5.5)$$

The matrix  $A$  of the scalar products of the neighborhood points with the direction parameters is calculated, that is:

$$A = \begin{pmatrix} (\vec{p}_1 \vec{\mu}_1)^2 & (\vec{p}_2 \vec{\mu}_2)^2 \\ \vdots & \vdots \\ (\vec{p}_N \vec{\mu}_1)^2 & (\vec{p}_N \vec{\mu}_2)^2 \end{pmatrix}. \quad (5.6)$$

The concentration parameters can then be calculated in least-square sense from the following linear equation system using the Moore-Penrose pseudoinverse:



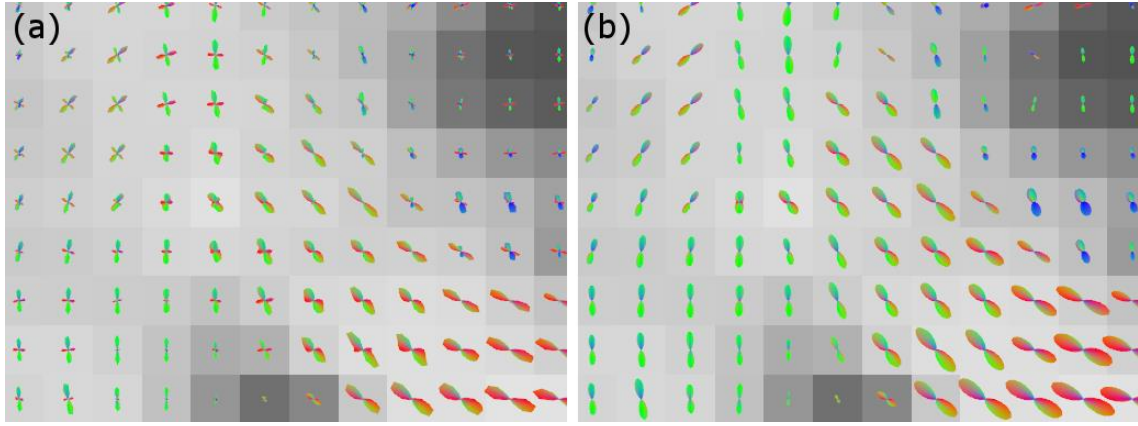


Figure 5.3: fODF and Bingham fit visualized on the brain. This image is taken from the coronal area, where the corticospinal tract and the corpus callosum cross. In (a) the fODF is shown. In (b) the Bingham fit for the largest peak can be seen, extracting the main bundle behavior.

$$\vec{\beta} = A \begin{pmatrix} k_1 \\ k_2 \end{pmatrix}. \quad (5.7)$$

An important aspect of this approach is the neighborhood of the fODF peak, which is used for as well the least square fit of the concentration parameters, as the fit of the Bingham function directions. Therefore it is important to ensure that the neighborhood represents the properties of the selected fiber peak as accurately as possible. This is done by using an adaptive neighborhood estimation, which successively adds points to the neighborhood as long as the sign of the slope of the fODF does not change. This way every point is included that can be identified with a certain peak and the number of points used for the Bingham fit is maximized. However, one does not want to include too many points in the estimation of the orientation matrix, since this may shift the maximum direction due to bias introduced from the other bundles present in the voxel. Therefore a smaller area is used for estimation of the orientation matrix, comprised only of first-, second- and third-degree neighbors (about 35 points on the search grid). For fitting the concentration parameters a larger number of points is used, determined adaptively as described above. The fitting result and the areas used for estimating the parameters are exemplified in Figure 5.1.

While the Bingham fit is able to characterize each of the separate fODF peaks, it does not provide a decomposition of the fODF. This is due to overlap between the Bingham functions. Main source for the overlap are the wide tails of the Bingham distribution. When comparing the Bingham fit to the fODF, then one can also observe a mismatch in the areas where the fODF drops to zero. This, however, does not imply that the fibers are not necessarily Bingham distributed. Instead the mismatch may be caused by the blurring introduced to the

fODF due to the SH fit. As discussed in Chapter 4.5.5 this has the effect of widening of the fitted Bingham functions, which also manifests in thicker tails.

## 5.4 Conclusion

In this chapter I presented an approach for fitting a Bingham distribution to the fODF. This gives a parameterization of the fODF, which can be directly interpreted in terms of microstructural arrangement (see Chapter 6). I discussed the three steps for fitting the fODF, which are finding the maximum, fitting the peak directions and calculation of the concentration parameters. As can be seen in Figure 5.2 this method is able to describe each of the fODF peaks separately.

One of the most interesting findings was the mismatch in shape between Bingham functions and the fODF. Since this mismatch also appears in regions with a single fiber population, I can conclude that the mismatch is not due to the separate fit of the individual fODF peaks. It either stems from the Bingham function being ill suited to describe the distribution of fibers within a fiber population or from errors in the fODF description of the underlying structure. I cannot answer this question completely, however, as discussed in Chapter 4.5.5 the SH expansion introduces blurring to the fODF. It therefore is likely that this blurring leads to the mismatch, especially as it causes peaks to be wider than they in fact are.

Another phenomenon is the overlap of the individual fitted Bingham functions. This may be mitigated by taking into account the overlap during fitting and not fitting each peak individually. However, this reintroduces a model selection problem. An approach to solving this was presented in the work of Kaden and colleagues (Kaden et al., 2007), where the Bingham distributions are fitted directly to the signal.

In summary the Bingham fit is a useful tool for characterizing the separate peaks and thereby characterizing underlying fiber populations, without the need for solving a model selection problem. It thereby characterizes not only the microstructure, but also describes the properties of the fODF which are most commonly used in tractography. The fitted functions can then be used for the calculation of tractograms (see Chapter 7) and the definition of metrics (see Chapter 6). These results can then be used for gaining insight on the workings of the human brain.

# 6 Bingham Metrics

---

## 6.1 Introduction

The human brain to this day remains one of the big mysteries. To gain more insight on the human brain, describing its microstructure is fundamental. In this chapter I will introduce a few metrics I derived directly from the Bingham fit, introduced in Chapter 5. Due to them being derived directly from the fit of the fODF, they are inherently connected to the brain's fiber architecture. This makes these metrics sensitive to variations in particular changes in fiber arrangement and shape, which is the big advantage of these metrics compared to FA.

Generally speaking metrics quantify physical quantities by reflecting them in terms of a distance in a parameter space. In biological tissue a large number of properties can be reflected. This leads to metrics usually having only one of two characteristics. They can either be very specific in describing the difference in a certain microstructural property or they can be sensitive to changes in a more general sense. An example for a sensitive but unspecific metric is the FA. The anisotropy in a region may be lower because of a reduction in myelination or an increase in the variance of fiber orientation, but also because there is a larger axon diameter, a lower packing density (S. Takahashi et al., 2002) – both of which denote fewer barriers to diffusion in a given space – or it could be due to increased membrane permeability (reducing the effectiveness of a boundary). However, as this example already shows one is not able to determine the particular type of microstructural change simply from a change in FA. Other metrics derived from the tensor, such as radial, axial and mean diffusivity, have also been shown to correlate with microstructural properties, but not to be quantitatively related to certain microstructural properties.

In summary, the goal of the work presented within this chapter is to use the introduced parameterization of the fODF (see Chapter 5), which identifies multiple compartments, each representing a relatively coherent fiber bundle described by a set of meaningful parameters, and to interpret the parameters of this model, as far as possible, in terms of microstructural properties, hopefully increasing the specificity of the assertions made from changes in FA.

The fODF describes the angular spatial fiber density, while the Bingham function describes the bundle wise angular spatial fiber density. This enables us to extract metrics for each of the bundles present within a voxel, which is observable as fODF peak. This connection of

the Bingham fit to the microstructure is of fundamental importance for the interpretation of the meaning of the derived metrics.

In this chapter, I explore several metrics derived directly from the Bingham functions used to characterize the fODF and with it the tissue microstructure. These are for example the parameters of the Bingham distribution itself, which are scaling parameters and concentration parameters, characterizing the size and shape of the underlying fiber bundles. In addition I use more complex parameters such as the bundle specific fiber density, the fiber spread and a complexity metric, which reflects the fiber populations present within each voxel and their relative sizes. This allows us to examine the microstructure in the voxel.

The work within this chapter is an original contribution and has been submitted (Riffert et al., 2013).

## 6.2 Bingham Function Parameters

The metrics which are most easily estimated from the Bingham fit are the parameters of the Bingham function (equation (5.2)). These are the scaling parameter  $f_0$ , the concentration parameters  $k_1$ ,  $k_2$  and the directions  $\vec{\mu}_0$ ,  $\vec{\mu}_1$  and  $\vec{\mu}_2$ .

The scaling parameter corresponds to the angular density of fibers (AFD) which are aligned with the peak's main direction. I therefore named this parameter the *maximum angular fiber density* ( $AFD_{\max}$ ). It has the same unit as the fODF  $(mm^3 rad)^{-1}$  and is defined as:

$$AFD_{\max} = f_0 \quad (6.1)$$

The two concentration parameters characterize the peak anisotropy and provide a measure for the spread of fiber orientations within one bundle. Large concentration parameters stand for a sharp peak. The relation between the two concentration parameters provides information on the fODF's cross section. If the concentration parameters differ strongly in their amplitude, the peak's cross section is very oval, indicating fan-like spreading as expected in thin sheet-like fiber populations. Concentration parameters of similar value correspond to a round fODF profile. In order to make the concentration parameters more accessible to intuition I translated them to directional peak opening angles along the axes  $\vec{\mu}_1$  and  $\vec{\mu}_2$  ( $\kappa_1, \kappa_2$ ; see Figure 6.1). The opening angles are defined analogously to the angle at which a normal distribution has a distance of one standard deviation to its mean.

When viewing the Bingham function as angular function in one of the planes spanned by the main direction and one of the minor directions (i.e.  $\vec{\mu}_0 \times \vec{\mu}_1$  or  $\vec{\mu}_0 \times \vec{\mu}_2$ ), then one can write the Bingham function in dependence of the angle  $\alpha$  between the direction for which

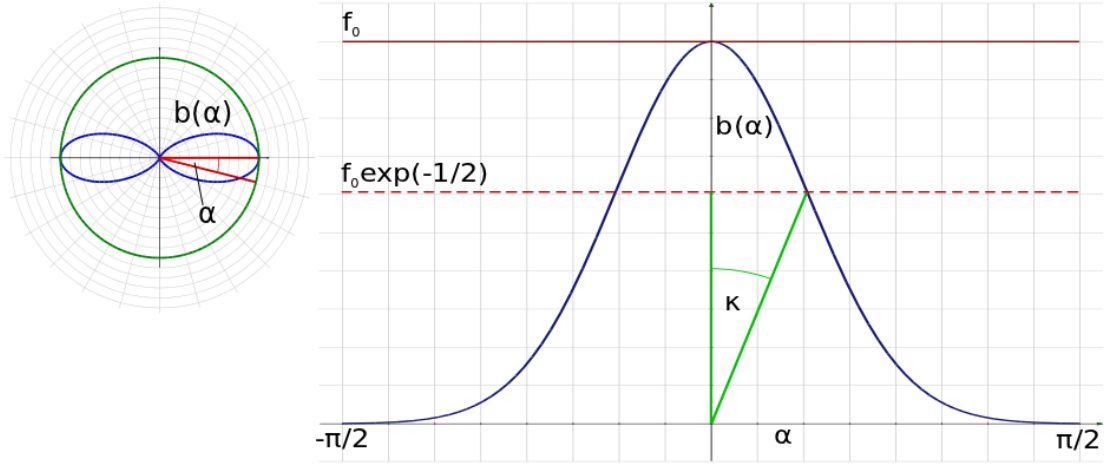


Figure 6.1: Relation between the directional peak opening angle and the concentration parameters. On the left the Bingham function is shown in blue as polar plot (a). The green circle shows the value  $f_0$ . The angle to the main direction of the Bingham function is noted as  $\alpha$ . On the right the Bingham function is shown as function of  $\alpha$  in Cartesian coordinates (b). The angle  $\kappa$  describes the angle at which the function dropped to  $\exp(-1/2)$  of its maximum value.

one wants to examine the concentration parameter and the main direction (as shown in Figure 6.1). As function of  $\alpha$ , the Bingham function reduces to:

$$\beta(\alpha) = f_0 \exp(-k_{1,2}(\sin \alpha)^2) \quad (6.2)$$

The concentration parameter dependent opening angle  $\kappa_{1,2}$  are defined as:

$$\kappa_{1,2} = \arcsin \sqrt{\frac{1}{2 k_{1,2}}} \quad (6.3)$$

This angle describes the distance to the main direction at which the function dropped to  $\exp(-1/2)$  of its maximum value. This is analogous to the angle at which a Normal distribution reaches 1-sigma level, that is:

$$\left( \mathcal{N}(\sigma) = \frac{1}{\sigma\sqrt{2\pi}} \exp\left(-\frac{1}{2}\right) \right) \quad (6.4)$$

Therefore the angle  $\kappa$  can be seen as the standard deviation angle of the Bingham function. In the following I will use both descriptions of the concentration parameters. It should, however, always be clear from context if I am referring to the opening angle or the actual concentration parameters.

The Bingham function's directions were not used for quantitative evaluations. For describing more complex properties of the fibers one can generate more complex metrics

describing the fODF by combining these parameters or using the information of the distinct populations within the voxel, as these are all fitted by Bingham functions.

## 6.3 Fiber Density (FD)

A quantity I already discussed in the context of the first SH expansion coefficient (Chapter 4.4.6) is the fiber density. This metric was extracted from the connection between the first SH expansion coefficient and the integral of the expanded function over the sphere. The integral over the Bingham function represents the angular spatial fiber density of a single fiber population therefore gives us the fiber density within the corresponding bundle.

This connection can be formulated mathematically as:

$$FD = \int_{S^2} \beta(\theta, \phi) \sin \theta \, d\theta d\phi. \quad (6.5)$$

The resulting value is the bundle's *fiber density* (FD). Since the unit of the AFD is  $(mm^3 rad)^{-1}$  integration over the radial part leads to the unit  $mm^{-3}$ .

As this integral cannot be solved analytically it has to be solved using numerical integration. This is done using the tessellation of the sphere for calculating the Bingham function value at each of these points and then solving the integral using a discrete sum and the area of the triangles used in the tessellation as described in the work of Atkinson (Atkinson, 1982).

It should be noted that the total FD in a voxel cannot be calculated from adding the individual FD. This is due to the Bingham fit not being a decomposition of the fODF, but a successive description of its features.

## 6.4 Fiber Spread (FS)

A fundamental quantity for describing the configuration of a fiber population is its spread or collinearity. This can be described in terms of the concentration parameters of the Bingham function. These parameters, however, are as I will show later on (see Chapter 6.6) not very robust.

Using the metrics  $AFD_{\max}$  and FD, one is able to define a robust metric, which describes the *fiber spread* (FS) by using their quotient.

$$FS = \frac{FD}{AFD_{\max}}. \quad (6.6)$$

This metric compares the maximum AFD to the average AFD. In case of a wide peak the average and maximum value are closer than in case of a sharp peak. This leads to the FS of a wide peak to be larger than that of a sharp peak. The FS can also be interpreted as the width of a rectangular distribution of constant height with equal FD.

The unit of the FS is radians. It should be noted that the value of the metric FS is equal to the value of the normalization constant of the non-scaled Bingham distribution.

## 6.5 Structural Complexity (CX)

A possibility of deriving metrics from a separate description of the fiber bundles within a voxel is to describe the relation of the different bundles to one another. The quantity most suited for such a comparison is the voxel wise FD. This is due to the fact, that comparing the FD within a voxel is equivalent to comparing the number of fibers within the bundles.

A property which is of great interest is the *structural complexity* (CX) within a voxel. This metric describes the fiber fraction not contained by the largest bundle. This metric is called the (structural) complexity, as the more complex the fiber structure becomes the fewer of the fibers in the voxel are contained in the largest bundle alone.

If one defines  $FD_i$  to be the fiber density of the  $i$ -th largest peak of the fODF and  $n > 1$  to be a predefined number characterizing the number of peaks investigated per voxel, then CX is defined by:

$$CX = \frac{n}{n-1} \left( 1 - \frac{\max_i FD_i}{\sum_{i=1}^n FD_i} \right). \quad (6.7)$$

The value is scaled to lie between zero and one. In case of a single fiber being present within a voxel the CX is zero. It becomes one, when all peaks contain the same number of fibers.

A bundle specific metric implicitly used in the CX metric is the *fiber fraction* (FF) which I am not going to investigate further, but which was used in the work of Schreiber and colleagues (Schreiber et al., 2013). It is defined as:

$$FF_b = \frac{FD_b}{\sum_{i=1}^n FD_i}. \quad (6.8)$$

This metric describes how dominant a fiber population is compared to all the fiber populations in the voxel, by describing the fraction of fibers in the voxel contained within the specific population. Using this metric the CX can be written as:

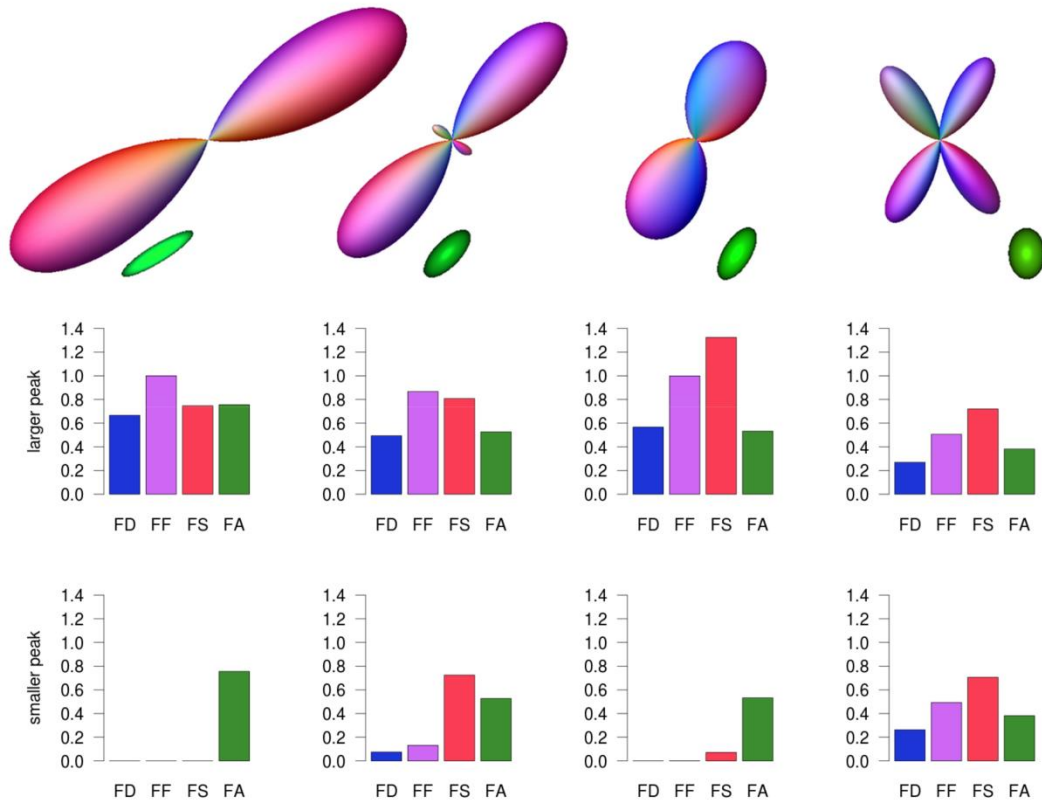


Figure 6.2: Comparison of FA and parameters of different fiber configuration. In the top row glyphs representing the fODF (purple) and the diffusion tensor (green) are visualized. Below a few of the Bingham metrics and the FA are shown for the larger and smaller peak. Image adapted from the work of Schreiber et al. (Schreiber et al., 2013).

$$CX = \frac{n}{n-1} (1 - FF_1). \quad (6.9)$$

## 6.6 Evaluating Metrics

### 6.6.1 Introduction

After defining the metrics it is important to ensure their connection to the microstructural properties they are meant to describe. One way of doing this is by applying the metrics to data with a known ground truth. The easiest ways to control the ground truth is to use simulated data as well as phantom data.



The two main questions I aim to answer by using this data are: How well are the ground truth values reconstructed and how well do the metrics specify the information gained from FA. Figure 6.2 shows some Bingham metrics and the FA for a small set of different fiber configurations.

In the following I will discuss the generation of the test data and the measurement of the brain data the metrics were applied to. Then I will go over the results in case of simulated data, phantom data and the measured human brain data. Application of the metrics to fetal dMRI data will be discussed in Chapter 8, where I classify structural changes in the brain due to brain development in terms of Bingham fit derived metrics.

## 6.6.2 Data Generation and Measurements

For evaluation, I applied the introduced method to three types of data: computer simulated data, measured data from a physical phantom, and human brain data.

The simulated data was generated in such a way that the underlying fiber distributions were exactly covered by the model (i.e., Bingham functions) and the ground truth was known. This was achieved by Bingham distributing the signal generated from a diffusion tensor, which was taken to represent the diffusion profile of a single fiber. For these Bingham distributions the parameters were varied randomly and then the reconstructed values were correlated with the ground truth. The diffusion signal was calculated by computing the forward model, that is, convolution (as described in Chapter 7.3). This was done for a single bundle as well as for a configuration involving two bundles that cross at a random angle. It was assumed that the signal attenuation generated by a single fiber, that is the deconvolution kernel, to be appropriately described by a diffusion tensor with an FA of 0.86 and the eigenvalues  $\lambda_1 = 0.0014$  and  $\lambda_2 = \lambda_3 = 0.000177$ , which corresponds to a MD of 0.0006. This kernel was estimated from the corpus callosum voxels of a human dMRI data set. The parameters of the Bingham distributions were chosen to be uniformly distributed within intervals estimated from real data, so  $0^\circ < \kappa_1, \kappa_2 < 90^\circ$ ;  $0 < f_0 < 3$  in the single fiber case. For the crossing case two Bingham distributions were assumed, crossing at an arbitrary angle between  $60^\circ$  and  $90^\circ$ . Furthermore the parameter space was reduced ( $15^\circ < \kappa_1, \kappa_2 < 30^\circ$ ;  $1 < f_0 < 2$ ) to ensure that crossing are properly resolved and to minimize Bingham function overlapping. Sixth and eighth order constrained spherical deconvolution were performed on these datasets. Afterwards the correlation between the reconstructed values of the metrics and the ground truth was calculated.

To test the Bingham fit and to find out how it behaves in more intricate geometries and under more realistic conditions, while still having ground truth knowledge to validate the results, the phantom data from the fiber cup contest was used (Fillard et al., 2011). The

creation of the physical phantom is described in (C. Poupon et al., 2008). The dataset used was measured at a b-value of 2000 and with a spatial resolution of 3 mm (isotropic voxels). As the kernel a diffusion tensor was used. It was defined by the eigenvalues  $\lambda_1 = 0.0018$  and  $\lambda_2 = \lambda_3 = 0.0014$  which corresponds to an FA of 0.12, which is the average FA in the single fiber areas of the physical phantom. Due to the different properties of the synthetic fibers, the FA is much lower than in human datasets.

Finally, the introduced methods were applied to an in-vivo human diffusion data. The experimental setup was approved by the local ethics committee of the University of Leipzig and the participant gave written informed consent before being included in the experiment. A 3D  $T_1$  weighted structural MPAGE scan (spatial resolution = 1 mm<sup>3</sup>) as well as a high resolution dMRI scan from a young right-handed volunteer were acquired on a whole-body 3 Tesla Siemens Tim Trio magnetic resonance scanner (Siemens, Erlangen, Germany) equipped with a 32-channel head array coil. For the dMRI a spin-echo echo planar imaging (EPI) sequence was applied (TE = 85 ms; TR = 13.8 s; 144 x 144 image matrix; FOV = 220 x 220 mm<sup>2</sup>; 85 axial slices (no gap); spatial resolution: 1.5 x 1.5 x 1.5 mm<sup>3</sup>, GRAPPA acceleration factor 3, no cardiac gating, 60 diffusion directions evenly distributed over the hemisphere, b-value = 1000 s/mm<sup>2</sup>). Seven images without any diffusion weighting ( $b_0$ ) were obtained: one at the beginning of the scanning sequence and one after each block of 10 diffusion-weighted images as anatomical reference for offline motion correction. To increase *signal-to-noise ratio* (SNR), the measurement was repeated three times. The structural scan was reoriented to the sagittal intercommisural plane and the brain was segmented from the skull. The  $b_0$  images were used to estimate motion correction parameters of the dMRI sequence using the rigid-body registration (Jenkinson et al., 2002), implemented in FSL (FMRIB Software Library, University of Oxford, <http://www.fmrib.ox.ac.uk/fsl/>). The motion correction for the dMRI data was combined with the global registration to the  $T_1$  anatomy. Furthermore the gradient direction was corrected for each volume with the rotation parameters. The registered images were resampled to an isotropic voxel resolution of 1.5 mm and the three acquisitions were averaged. Finally, the diffusion tensor, the three eigenvectors, and the FA value for each voxel were computed. On this dataset an eighth-order SH approximation of the fODF using MRtrix (Tournier et al., 2012) was performed. After applying CSD to the signal attenuation the result was normalized to the number of fibers in the deconvolution kernel. The kernel FD was estimated as  $3.717 \cdot 10^5$  fibers per mm<sup>3</sup> in accordance to (Aboitiz et al., 1992). The same form of normalization was applied to the phantom data using the fiber density of 1900 fibers per mm<sup>3</sup>, as described by Fillard and colleagues (Fillard et al., 2011).

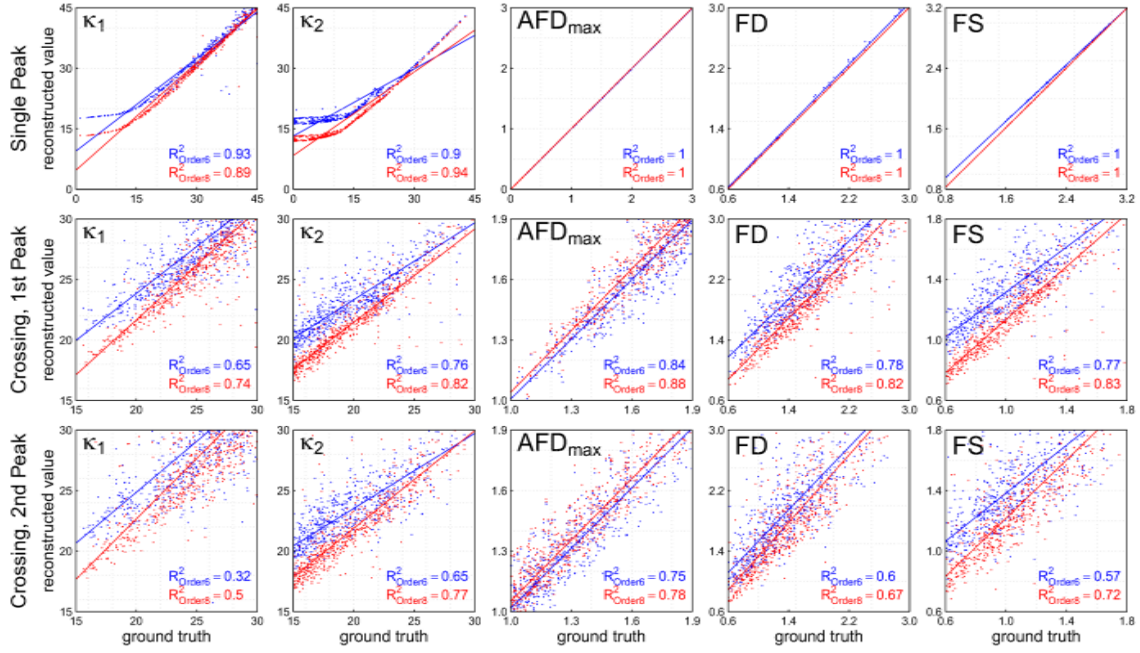


Figure 6.3: Correlation of ground truth and reconstruction. Here the correlation of metrics calculated using the Bingham fit and their ground truth values are depicted. Ground truth and reconstructed values are shown in the unit of their respective metric. The left column shows metrics reconstructed for a single fiber population being present within a voxel. The middle and right column show the metrics for the first (middle column) peak and second (right column) peak in the case of fiber crossing. In each of the panel the reconstructions are plotted for 6<sup>th</sup> (blue) and 8<sup>th</sup> (red) order SH series representation of the fODF. The lines show the linear regression results. The corresponding Pearson coefficients ( $R^2$ ) are displayed on the bottom right of each panel. As can be seen the spread of each of the parameters is smaller for the single fiber case, which leads to higher correlations.

Then the parameters of the Bingham functions were calculated, assuming each of the fODF maxima represented a single fiber population. To estimate the maxima of the SH a regularly tessellated search grid was used, which was constructed by 5 iterative refinements of a regular icosahedron resulting in 10,242 vertices and 20,480 faces.

The three largest peaks found on the search grid were chosen and the corresponding fODF peaks were approximated. In principle, more peaks are possible, depending on the quality and quantity of the available measurement information. The Bingham fit was performed using a neighborhood size of 35 points, that is all direct neighbors and neighbors of second and third order, around each maximum, which corresponds to an angle of maximal 6° per direction were used for determining the parameters of the Bingham function.

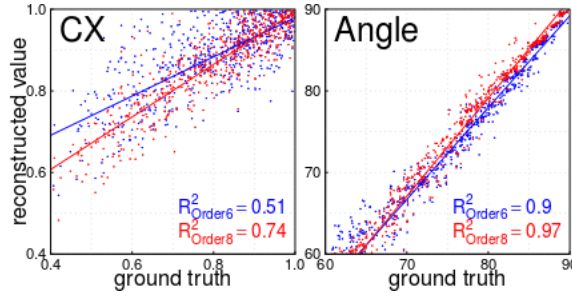


Figure 6.4: Correlation of CX as well as the crossing angle to the ground truth. Here the correlation for the metric CX as well as for the resolved crossing angle between the two peaks involved in the simulated crossing are shown. Colors and labels are same as in Figure 2.

### 6.6.3 Simulated Data

After establishing a method for generating metrics from the approximation of the fODF I established the relation of these metrics to the ground truth. This was done using simulated data. The main goal here was to derive rules on how to interpret the metrics when having applied the Bingham function based fODF peak fit to real data. For this one needs to focus on several questions.

First, one needs to know how well the metrics correlate with the ground truth and how the order of the SH reconstruction affects this correlation? This tells us in which range one can be sure, that the metrics and the ground truth are well connected.

I found that in the single fiber case the reconstructed values correlate to the ground truth very well. This can be seen in the left column of Figure 6.3. Here the ground truth and the reconstructed data show a correlation  $R^2$  very close to 1 for the metrics  $AFD_{max}$ , FD, FS and  $\kappa_2$ . Merely  $\kappa_1$  is correlated slightly worse. Of interest hereby is the strong bias in both concentration parameters for angles smaller than approximately  $17^\circ$  in case of 8<sup>th</sup> order SH reconstruction and  $20^\circ$  in the 6<sup>th</sup> order case. Outside of this area the concentration parameters show perfect alignment with the ground truth values, as do the values observed for the other metrics. Below those angles the concentration parameters are, however, reconstructed as nearly constant value independent of their ground truth value. This indicates an inability of the SH series of lower order to fit sharper peaks. Since this fit error has impact on the other metrics as well, I used only concentration angles larger than  $20^\circ$  for the analysis of the other metrics ( $AFD_{max}$ , FD, FS).

Next I analyzed the crossing fiber case. The results are shown in the middle and right column of Figure 6.3. As can be seen the crossing causes interference between the two peaks, which leads to a lower correlation of the reconstructed values to the ground truth

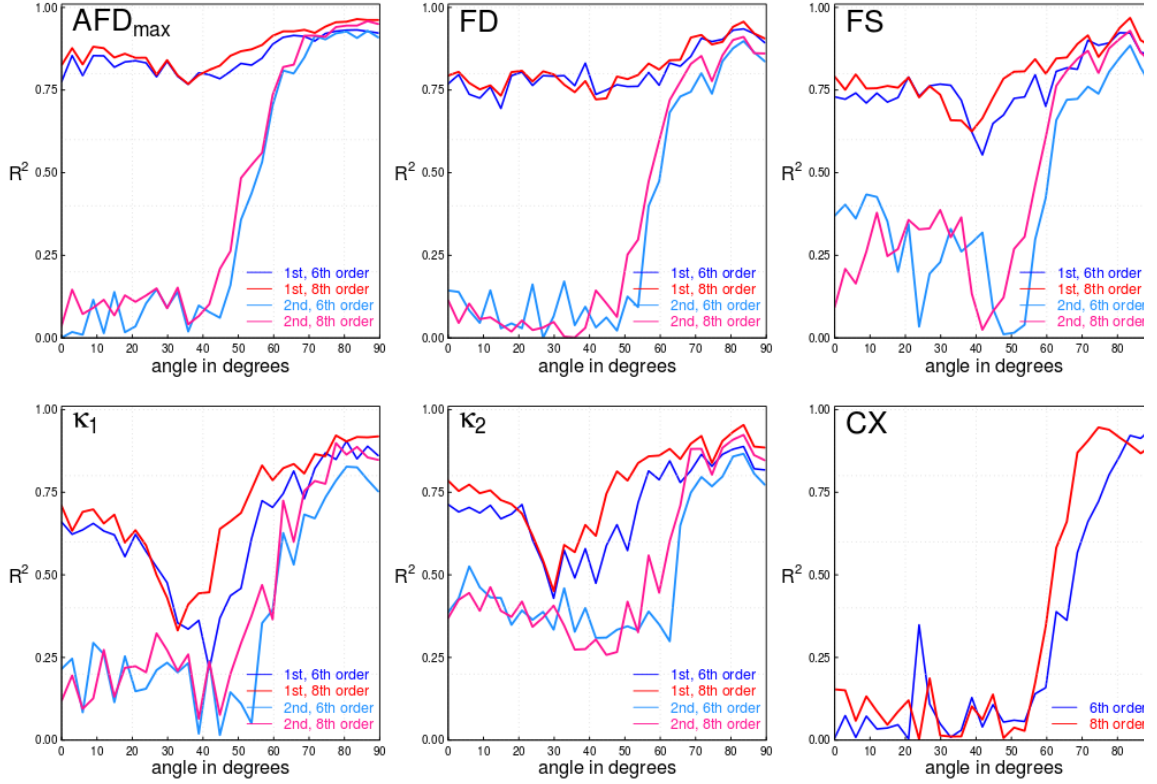


Figure 6.5: Angular dependence of the metrics ground truth correlation on the fiber crossing angle. These plots show the how the correlation between the reconstructed values and the ground truth depends on the fiber crossing angle and the order of spherical harmonic series approximation. While the correlation of the values reconstructed from the largest peak are quite high (between 0.80 and 1.00), except for the area between 10° and 40°, where lower values can be observed for some parameters (FD, FS and especially  $\kappa_1$ ), the second peaks parameters do not correlate well with the ground truth until a crossing angle of 50° is reached. Generally the higher order reconstruction shows better correlation to the ground truth.

than in the single fiber case. The metrics  $AFD_{max}$ , FD and FS are more stable than the concentration parameters, i.e. they show a higher correlation to the ground truth.

I also calculated the correlations for the CX metric and the crossing angle. These results are shown in Figure 6.4. The CX is recovered fairly well, i.e. it shows high correlation and only little bias, although the design of the simulation experiment leads to unevenly distributed CX values. The crossing angle on the other hand shows a strong bias depending on the order of SH reconstruction.

For further evaluation I mapped the crossing angle dependence of the correlation of the reconstructed values and the ground truth for 6<sup>th</sup> and 8<sup>th</sup> order SD (shown in Figure 6.5).

The noteworthy point is that the reconstructed parameters of the first peak highly correlate with the ground truth (values between 0.8 and 1.00), except between 10° and 40°, where the correlation drops off strongly for the parameters FS (0.6), FD (0.5) and  $\kappa_1$  (0.25). For the second peak the correlation is low up to an angle of 50°, which is the angle for which the peaks can correctly be separated. Furthermore one can observe how a higher order leads to a better correlation.

## 6.6.4 Phantom Data

To evaluate the metrics in a more meaningful, albeit somewhat less controlled, setting the decomposition method was applied to phantom data. Here I was especially interested if the metrics would be able to uncover the underlying fiber structure from the data. I focused on the metrics  $AFD_{max}$ , FD, FS and CX, as well as the FA for comparison. The goal was to check in a controlled environment what extra information could be revealed from the metrics derived from the fODF decomposition. The results are shown in Figure 6.6. The color maps in each example were scaled to maximize the contrast visible in the images. Values larger than the maximum value were set to red, while values smaller than the minimum were set to dark blue.

It should be noted that due to the different diffusion properties of the phantom the FA values are all much lower than in biological tissue. This change in diffusion properties, however, does not influence the values derived from the fODF as they are captured by the diffusion kernel.

I will begin by focusing on comparing the FA and the CX. Since one knows the actual fiber configurations for the phantom, shown in panel a) of Figure 6.5, one can validate the structural complexity metric by applying it to these configurations and compare it to the FA. While the complexity measure is mostly inversely proportional to the FA, in the area marked as A and circled in red, the complexity further specifies the information gained from the FA. In this area the complexity is high. This indicates a crossing fiber configuration. The value of 0.5 for the complexity metric (using a peak number of  $n = 3$ ) indicates a crossing of one large bundle containing approximately 2 times the number of fibers as the smaller bundles combined. The FA in the circled area is rather high despite of the crossing, since the smaller bundles do not influence the tensor as strongly as the larger one. When following the two crossing bundles separately one can derive the information for the voxel from the local surroundings.

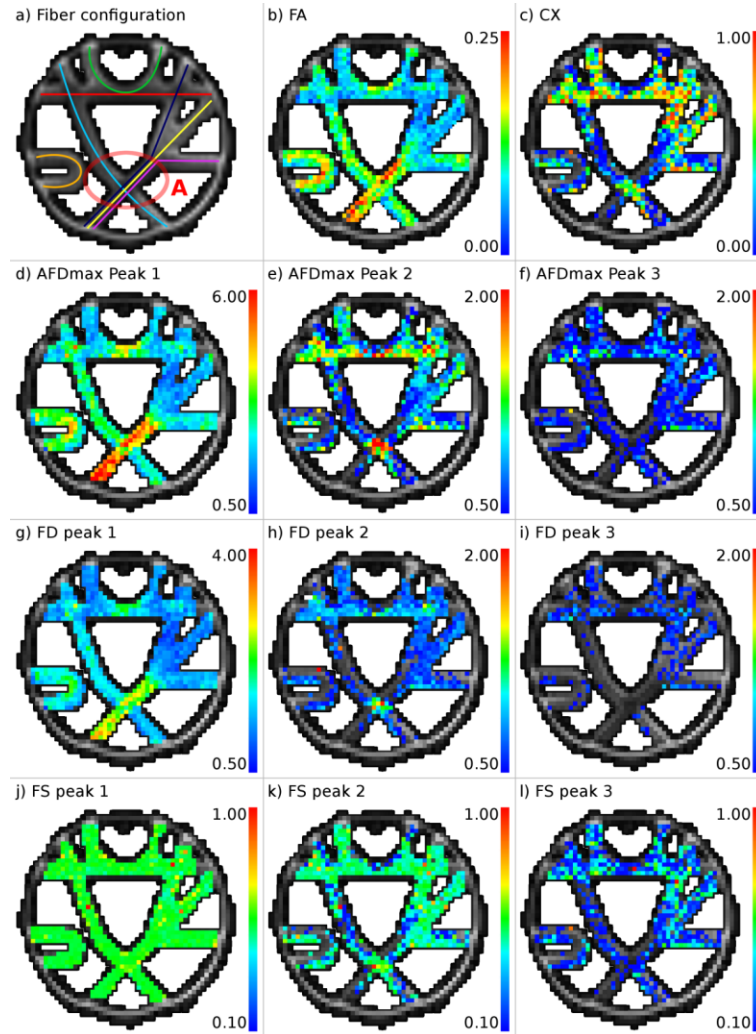


Figure 6.6: Metrics from phantom data. Here the metrics calculated from the phantom data are mapped upon the  $b_0$  image. The images were scaled for contrast. Values above the maximum value are set to red, ones below set to zero. The geometry is depicted in panel a). The metrics are shown in panels b) through l).

The complexity measure thereby not only increases the specificity, but in this case uncovers more microstructural information than the FA by indicating the underlying structure without the need to evaluate the surrounding structure. Similar information can be gained from the comparison of the  $AFD_{max}$  and FD for the different peak sizes. The  $AFD_{max}$  and the FD of the first peak show a very similar qualitative behavior to the FA. The further structural information can almost completely be gathered from the second and third peak.

An anomaly of this phantom, compared to biological data is uncovered by the metric FS. This metric is close to constant over the whole phantom, barring some noise voxels. This indicates that no significant fanning is present in this phantom and shows that the bundles



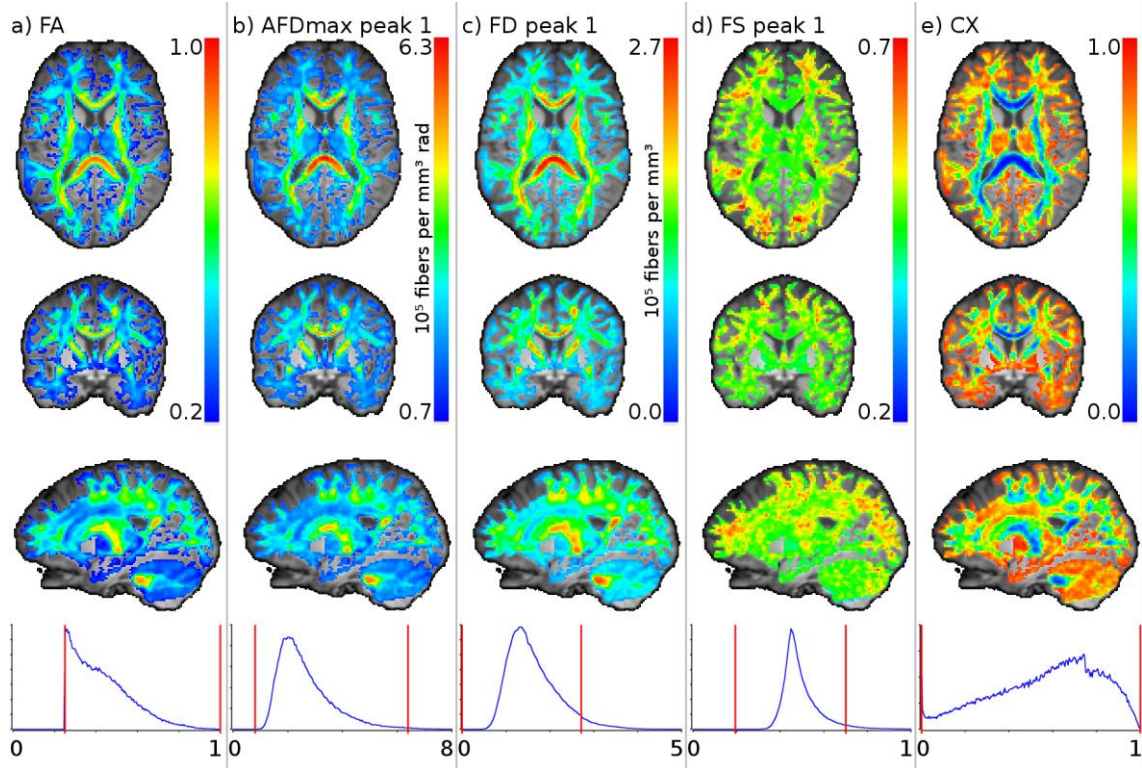


Figure 6.7: Primary metrics mapped on the human brain. Here the smoothed maps of the metrics FA, CX as well as the three metrics  $AFD_{max}$ , FD and FS which characterize the first peak are displayed. The metrics images were masked to the white matter using an FA map with a threshold of 0.15, which were manually expanded to match the white matter. These maps were then overlaid on an interpolated T1 image and scaled for contrast. The boundaries for the scaling are marked in the histograms at the bottom. The value  $n$  represents the number of voxels in which a certain value occurs. These are the images obtained from smoothing the original metrics before applying the white matter maps. The results without the smoothing steps can be found in Figure 6.11.

are all configured almost the same way. This especially leads to  $AFD_{max}$  and FD being very similar, since they are then related by a constant factor.

### 6.6.5 Human Brain Data

Next I applied the Bingham fit to fODFs from in-vivo MRI data of a human brain and evaluated the derived metrics. I will first take a look at the results from the metrics of the first peak, as well as FA and CX. To increase the visual effect of these metrics I applied a smoothing with a gauss kernel of 1 mm. The original maps are show in Figure 6.11 and Figure 6.12. The smoothened results are depicted in Figure 6.7 and Figure 6.8. Again the FA and the  $AFD_{max}$  as well as the FD of the first peak appear qualitatively similar, with high



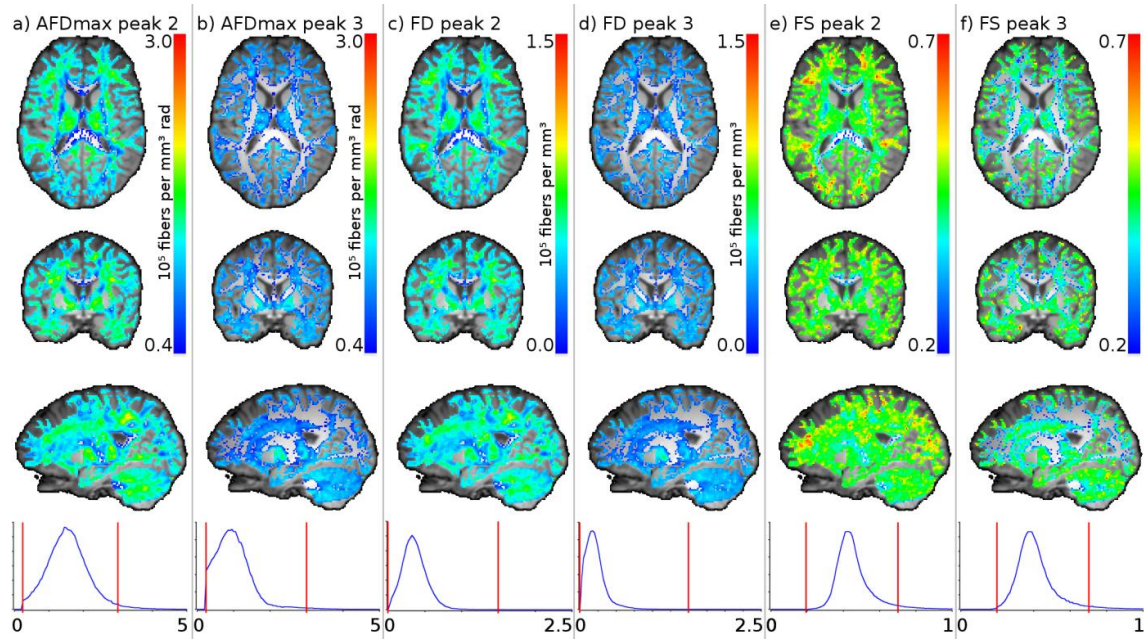


Figure 6.8: Metrics of secondary and tertiary fODF peaks. These maps were created as those in Figure 6.7, including the scaling and the histograms at the bottom. The maps for the non-interpolated metrics can be found in Figure 6.12.

values in the corpus callosum (CC) and the cortical spinal tract (CST) and low values in crossing areas and in the vicinity of the cortex (correlations as shown in Figure 6.9: FA to  $AFD_{max}$  and FA to FD both 0.62). The CX metric appears to be negatively correlated to these metrics (-0.57). One is clearly able to distinguish the crossing areas from areas with aligned fiber structure from the CX map. In other words this metric has higher values in the crossing and fanning regions, while CC and CST are shown to have medium to low structural complexity. The fiber spread also shows the expected behavior for the first peak by being higher in the corona radiata and other fanning white matter regions, while being lower and close to constant in the other regions. It is especially high in the subcortical white matter.

The metrics derived from the Bingham functions fitting the secondary and tertiary peaks of the fODF are shown in Figure 6.8. As can be seen the maps for the higher order peaks get more and more sparse due to those peaks not being present in the fODF.

The  $AFD_{max}$  parameter is significantly smaller for the second and third peak, than for the first peak. It also is the parameter by which the peaks are sorted. While the map of this parameter of the first peak was similar to the FA, the parameter is significantly different for second and third peak. In the CC and CST the second and third peaks  $AFD_{max}$  is low while being large in the crossing regions and at the grey-white-matter boundary.

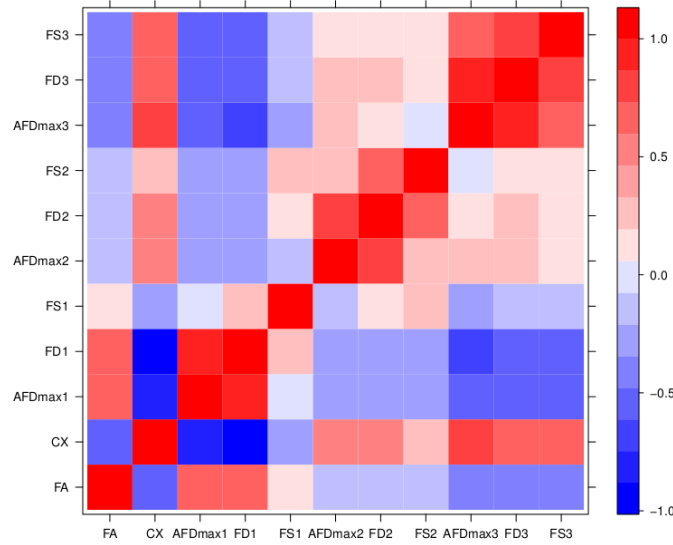


Figure 6.9: Correlation between metrics. This image shows the correlation structure of the metrics. For correlation purposes a white matter skeleton was used on which the metrics were mapped. All voxels for which either of the metrics was equal to zero was dismissed. As can be seen 3 clusters can easily be identified. The first contains FA, CX,  $AFD_{max1}$ , FD1, the second  $AFD_{max2}$ , FD2 and FS2, the third  $AFD_{max3}$ , FD3 and FS3. This indicates a strong connection between FA, as well as shape of the first peak and the microstructural properties at the same time.

The FD maps show strong dissimilarity between the first, second and third peak. While the first peak's map is similar to the FA, the second peak's map resembles the CX. The third peak's FD on the other hand is relatively smooth and has significantly smaller values.

Finally the correlations between the metrics are depicted in Figure 6.9. Here some interesting observations can be made. The FA is negatively correlated to the CX as well as positively correlated the  $AFD_{max}$  and FD of the first peak. It shows little to no correlation to any other metric, especially those of the non-primary peaks. This indicates a strong connection of the FA to the shape of the first peak. The CX, on the other hand, is correlated to all metrics, while the  $AFD_{max}$  and FD are mainly correlated within corresponding peaks, showing little to no inter-peak relationship. For inferring the spatial connection between the metrics  $AFD_{max}$ , FD, FS, CX and the FA, the spatial distribution of the summands of the Pearson correlation coefficient ( $R^2$ ) was visualized in Figure 6.10.

The average of all the summands gives the correlation between the FA and the metric, as depicted in Figure 6.9. Here one can observe that FA and the metrics  $AFD_{max}$ , FD and CX are strongly connected in areas without a high number of fiber crossings.

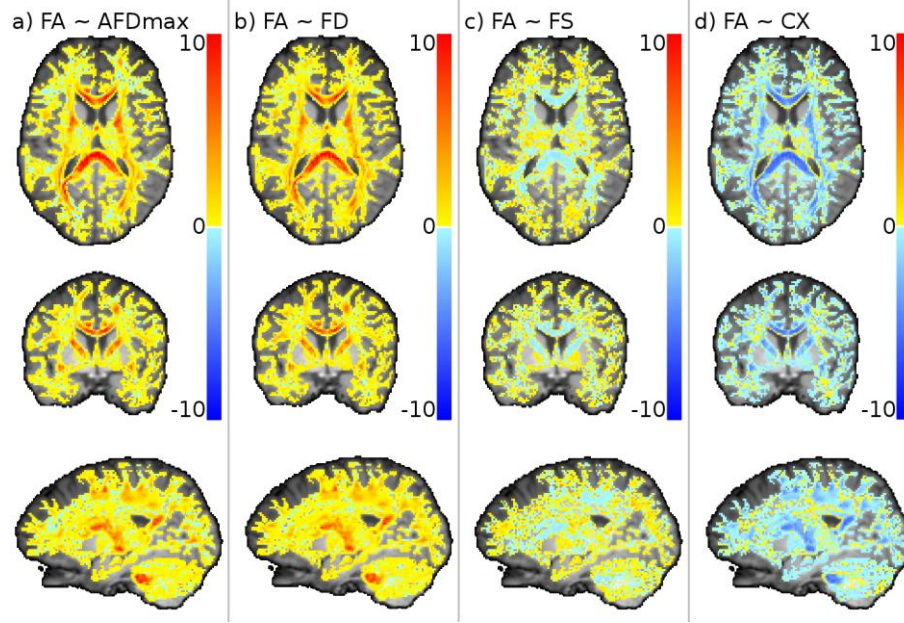


Figure 6.10: Spatial mapping of contribution to correlation with FA. The values correspond to the summands of the Pearson correlation coefficient. The average of these values over the whole masked region gives the correlation, which is shown in Figure 6.9. As can be seen, for  $AFD_{max}$ , FD and CX high values (in case of CX) low values can be found in the main fiber bundles, i.e. especially in regions without major crossings. The FS shows small negative values mainly in areas without fiber crossings.

The FS shows only a low correlation overall and also the spatial map does not reveal any areas of high connection, except for small positive summands in the crossing areas and negative values in the areas without strong crossings.

## 6.7 Conclusion

I used Bingham functions, that is, scaled Bingham distributions, to characterize the peaks of the fODF estimated from constrained spherical deconvolution (CSD). It was assumed that the peaks of the fODF to reflect the microstructural fiber bundles present in a voxel. The fitted Bingham functions share geometric properties with the fODF, which can directly be translated to metrics describing properties of the underlying fiber bundle. The introduced metrics were the fiber density (FD), maximum angular fiber density ( $AFD_{max}$ ), the fiber spread (FS) and the structural complexity (CX). I validated the metrics using simulations and then investigated their behavior using a physical phantom. Here, the known fiber layout enabled us to investigate how these metrics compare to the FA and show areas where they increase its specificity. Finally the introduced methods were applied to in-vivo brain scans. I demonstrated how the proposed metrics can be used on their own to draw conclusions

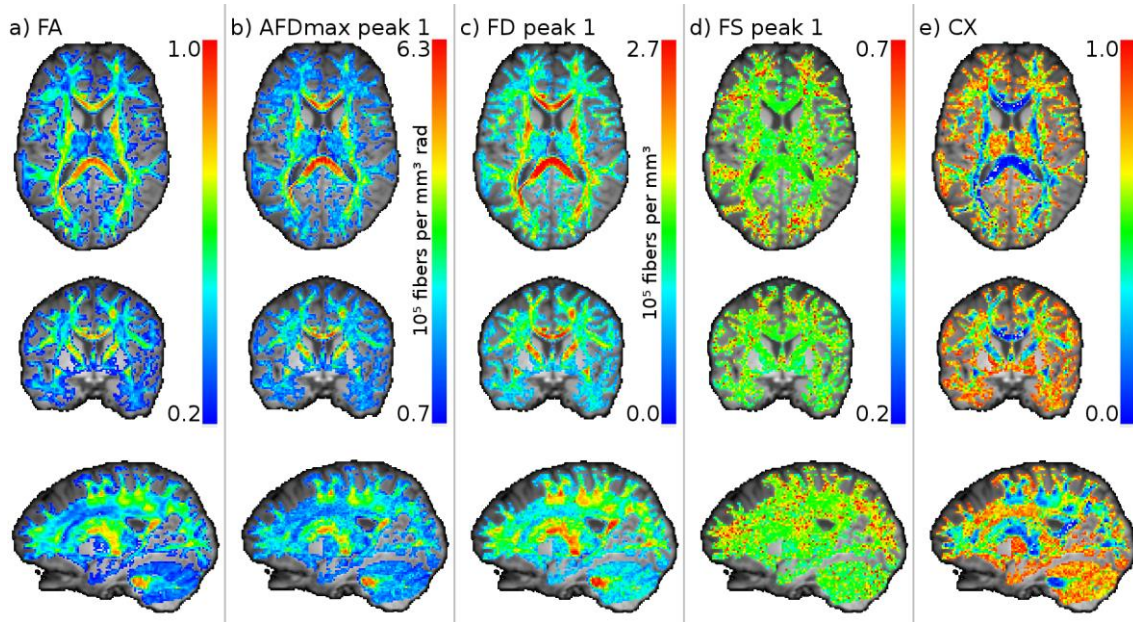


Figure 6.11: Unsmoothed metric maps for the first peak, FA and CX.

on the underlying microstructure, and how they may help to provide findings from the FA with additional meaning, thus increasing specificity.

In detail I found, that as expected, the  $AFD_{max}$  specifies areas of high fiber colinearity, the FD gives insights into the fiber density, and the CX correctly identifies regions of fiber crossings. Furthermore, I found that the CX and the  $AFD_{max}$  as well as the FD of the largest peak strongly correlate to the FA (as shown in Figure 8). Besides this, I showed that the correlation mainly originates from areas without major fiber crossings (Figure 9), therefore these metrics can be believed to hold information additional to that of the FA. This confirms that the FA is a metric describing a mixture of properties, which can be specified using the CX, FD and  $AFD_{max}$  metrics. Moreover, it confirms that the FA can be explained purely by properties of the fiber configuration and does not necessarily reflect changes in fiber properties, such as myelination.

When mapping the bundle specific metrics a bundle correspondence problem arises, that is, between neighboring voxels it is not a priori clear which fODF peaks represent the same fiber bundle. As a result of this problem, the acquired maps for bundles appear less smooth than those of non-bundle specific metrics. The elegant solution to this problem is to map the parameters along single fiber pathways obtained from tractography. The decomposition of the fODF then allows the estimation of metrics along the fibers. This was investigated in the work by Schreiber and colleagues (Schreiber et al., 2013). Here a novel tractography method is used for estimating the most probable connection between two regions of



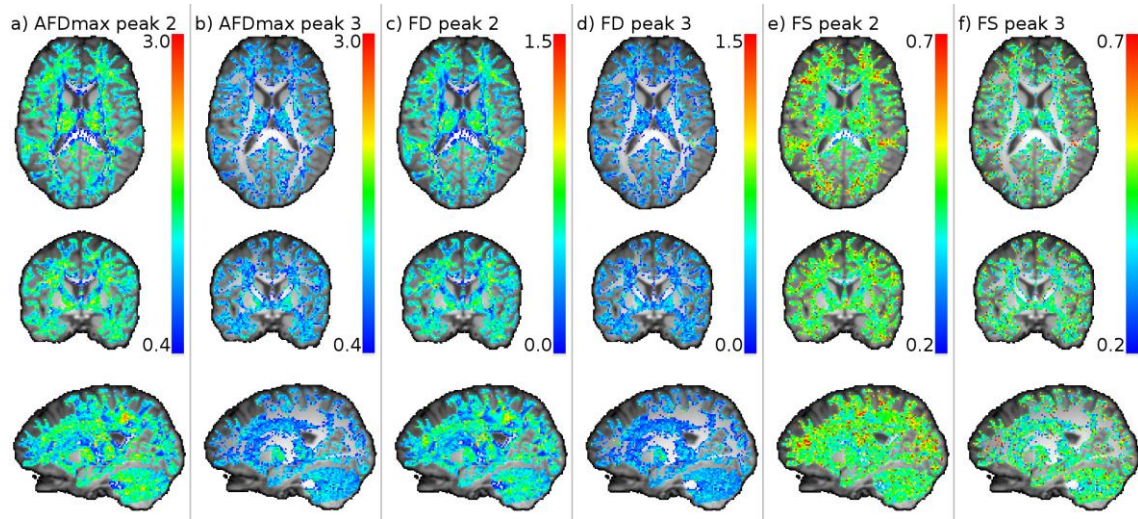


Figure 6.12: Unsmoothed metric maps for the second and third peak.

interest. Then, bundle dependent metrics like those described here are mapped along the pathways, thereby giving information on the change of the microstructure along distinct fiber bundles. A similar problem arises when bundle specific metrics need to be compared between subjects (e.g.; Jbabdi et al., 2010, Raffelt et al., 2012a).

While the increase in specificity already provides the means for more accurate investigation of regions with changing FA (or other tensor based measures) there are of course some limits concerning the spatial and angular resolution of this method, imposed by the voxel size and by the angular sampling. Moreover, the use of a constant deconvolution kernel inevitably obscures any changes in fiber properties. Hence, if there is a change in myelination or axonal diameter, this will be projected into changes in fiber density. In order to improve this situation, higher angular and especially spatial resolutions are needed (see e.g. Heidemann et al., 2012). Using multiple b-values and diffusion times does further improve the ability to resolve microstructural properties, such as axonal density and axonal diameter (Assaf and Basser, 2005, Alexander et al., 2010).

A different issue, also related to the resolution of the fODF, comes from the use of spherical harmonic representations, which, as with every truncated series expansion, introduces a bias into the reconstruction. This can be seen in the results from the conducted simulated data experiments. Here a higher order leads to a more accurate recovery of the ground truth used in the simulations. The order one can use, however, is limited by the number of gradient directions (and therefore the amount of information) measured and of course by the SNR (Jones et al., 2013). If the order of the spherical harmonic series expansion is too low, then peaks of certain sharpness (opening angle less than  $20^\circ$ , see Figure 2) cannot be

represented accurately. This also leads to crossings at small angles (for eighth order below  $50^\circ$  as shown in Figure 4) not being resolved properly, but rather being interpreted as a single large peak. As shown in Figure 8, the higher order leads to better correlation between ground truth and reconstructed values. However, with real data, stability requirements enforce regularization, which limits the effectively used model order.

A more fundamental point concerns the use of the SH representation in the spherical deconvolution scheme. Although this basis is very convenient for the calculation, it suffers from substantial limitations concerning its ability to represent the fODF. Especially if the kernel is estimated from voxels with relatively parallel fiber arrangement, such as the corpus callosum, the underlying fODF in these voxels as well as similar ones is per definition a Dirac delta function. In other words, very sharp functions have to be approximated, in particular within the large fiber bundles. On the other hand, the angular resolution of the SH representation is rather limited (as discussed in Chapter 4.6). Hence, especially for parallel fiber bundles, the SH representation is particularly weak.

Summarizing the Bingham function based fODF peak characterization is a useful tool for gaining insight into the fiber structure with higher specificity than with the FA. The direct link between the metrics and the fODF especially allows a direct correlation of differences in the metrics to changes in the structural configuration of the fiber configuration. However, this specificity also implies a loss in sensitivity, due to a loss of SNR caused by more complex models. Therefore they are best suited for the investigation of areas where one suspects changes in structure to cause changes in FA.

# 7 Bingham Fit Tractography

---

## 7.1 Introduction

The local information on the fiber layout can be used to propagate the local fiber information, allowing uncovering the larger scale fiber configuration. This process is called tractography. One of the first tractography algorithms (streamline tracking) was introduced by Mori and colleagues (S Mori et al., 1999). In this method the fiber layout is propagated starting in a seed point and then following the main direction recovered in a voxel, as long as certain conditions (e.g. FA threshold, curvature) are met. More sophisticated approaches, such as Runge-Kutta integration of the local directions (Chen and A. W. Song, 2008) and tensor lines (D. Weinstein et al., 1999), have been well established for the diffusion tensor. In particular the tensor deflection method (Lazar et al., 2003) has proven itself to produce robust tractography results and was implemented in various software packages (Fillard et al., 2007).

These improvements in tractography were not yet extensively applied to multi-directional complex models. Another advantage of the tensor based algorithms is the ease of interpolation, compared to higher order models.

Here I propose a novel scheme for integration of the improvement in tractography offered by tensor deflection to the multi-directional fODF based on the local model of spherical deconvolution. The idea is to use the additional information gained from using a higher order model, while being able to apply the framework of tensor based tracking methods, adapted only for multiple directions per voxel. This is achieved by applying the Bingham function based fODF peak fitting approach (see Chapter 5) to calculate Bingham functions representing the individual bundles present in each voxel. Afterwards I use the spherical convolution theorem (Driscoll and D M Healy, 1994) to calculate the corresponding diffusion signal for each of these bundles independently. The diffusion signal then can be used for the estimation of multiple diffusion tensors per voxel. Applying a tensor deflection algorithm, modified for selecting the tensor aligned to the current direction of propagation, I calculated a fiber tracking for visualizing the microstructure.

The work within this chapter is an original contribution.

## 7.2 Tensor Deflection

Tensor deflection is a deterministic tractography algorithm. Tractography is usually done by starting at a seed point and stepwise adding points based on the information gathered from the local model in each voxel. The most basic form of doing this is by using only the main direction in each voxel and following it. This method is called stream line tractography. The main idea behind tensor deflection (D. Weinstein et al., 1999) is to use the shape of the entire tensor for updating the direction of the tract's trajectory instead of just the main direction, thereby incorporating more of the measured information. This is done by multiplying the current direction  $\vec{v}_{in}$  with the diffusion tensor  $D$ :

$$\vec{v}_{out} = D \cdot \vec{v}_{in}, \quad (7.1)$$

to obtain the updated direction  $\vec{v}_{out}$ . The algorithm usually terminates a path if either the FA in a voxel becomes too small or the curvature of the path exceeds a predefined threshold. The deflection methods can be coupled with tensor interpolation. One strategy is to interpolate the tensor at a given point in space from the neighbors by log-Euclidian interpolation (Arsigny et al., 2006). I extended the tensor deflection to a field of tensors given in each voxel. First one has to select a tensor within a voxel for performing the deflection. This is done by choosing the tensor with the smallest angular difference between its main direction and the current direction of propagation. The same method was used for choosing the tensors within the neighboring voxels for interpolation. The selected tensors then are interpolated using the log-Euclidian metric.

## 7.3 Tensor Calculation from the Bingham Fit

The calculation of the tensor from the Bingham fit happens in two steps. First the signal of a Bingham distributed fiber population is computed. Second a diffusion tensor is fitted to the calculated signal. The basis for the computation of the signal from the fitted Bingham functions is the convolution theorem (3.33) as defined in Chapter 3.7. For the vector  $\vec{b}(p_i)$  of the Bingham function evaluated at the points  $p_i$  this is done by transformation into spherical harmonic space, convolution with the signal kernel and then back-transformation of the total signal to the gradient space. This requires a SH base matrix  $B$  which transforms to the gradient space and a SH base matrix  $C$  which is used to transform the vector  $\vec{b}(p_i)$  to the SH space. In short this can be written as:

$$\vec{E} = BD^{-1}(C^T C)^{-1}C^T \vec{b}, \quad (7.2)$$



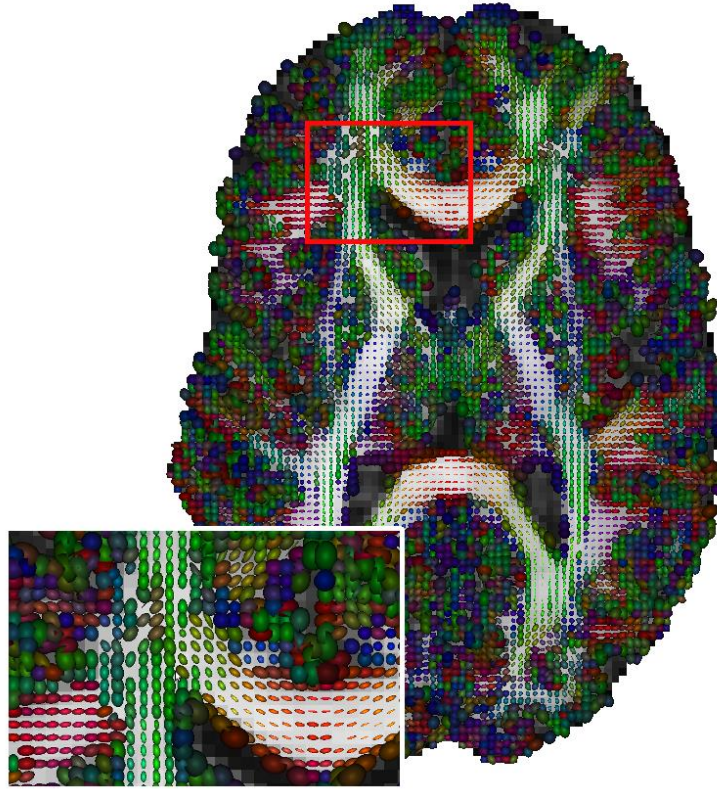


Figure 7.1: Bingham fit derived tensors. Here the tensors calculated from the Bingham fit are shown mapped onto an axial slice of the brain.

with the vector  $\vec{E}$  representing the diffusion attenuation signal in the gradient directions used for the generation of  $B$  and the matrix  $D$  being the deconvolution matrix defined in equation (4.51). The calculation of the diffusion tensor is then done, as described in Chapter 4.3.2. The resulting tensors are shown in .

The presented algorithms and methods are implemented in the open source software BrainGL (<https://code.google.com/p/braingl/>). Using this the diffusion tensor, the three eigenvectors, and the FA value for each voxel, were computed. For comparison an 8th order spherical harmonic approximation of the fODF using MRTrix (Tournier et al., 2012) was performed. The kernel was estimated from corpus callosum voxels with an FA of 0.8 or higher, indicating a single bundle direction being present within these voxels. Then Bingham functions were fitted to the largest three fODF peaks using BrainGL. Afterwards the diffusion signal corresponding to the fitted bundles was calculated and a tensor fit was performed on the reconstructed signal. For these tensors whole brain tensor deflection tractography was carried out. Every voxel in the brain's white matter was chosen as seed point and the main direction of the tensor of the peak with the largest magnitude was

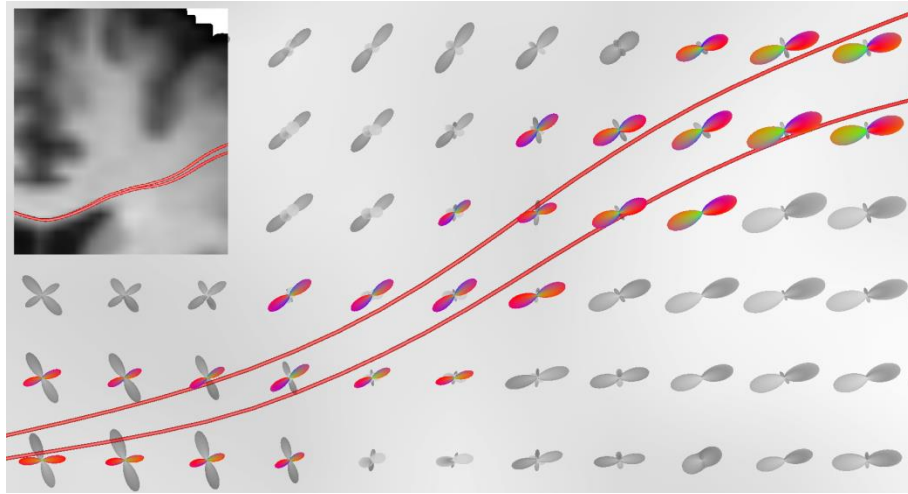


Figure 7.2: Bingham representation of peaks used in tractography. The colored peaks hereby represent peaks which the interpolation was based on. From these peaks then the diffusion signal and subsequently the tensor was calculated.

chosen as starting direction. For comparison tensor deflection tractography based on the single diffusion tensor, as well as fODF streamline propagation, as implemented in MRTrix (Tournier et al., 2012), were performed.

## 7.4 Results

The Bingham fit allows for the separation of peaks and for calculating the corresponding diffusion signal for these peaks separately. The tensors fitted to this signal represent the direction and shape of the fitted Bingham functions. This multi-tensor representation provides the framework for a robust multi-tensor-deflection. The resulting streamlines are locally smooth and robustly reconstruct the crossing fiber structure, as can be seen in Figure 7.2.

To illustrate the performance of the algorithm, the crossing region, where arcuate fasciculus, fibers of the corpus callosum and corticospinal tract cross, was used. Fibers in a crossing area from the whole brain tractography were selected using a  $3 \times 5 \times 5 \text{ mm}$  selection box implemented using a quad-tree selection (Blaas et al., 2005) in the software BrainGL. For the comparison of tractography results tractograms were calculated using the fODF peak deflection algorithm as well as the more traditionally used algorithms of tensor deflection and fODF streamline propagation. The tensor deflection was computed using BrainGL and the fODF streamline propagation was computed using MRTrix (Tournier et al., 2012). The results are shown in Figure 7.3.

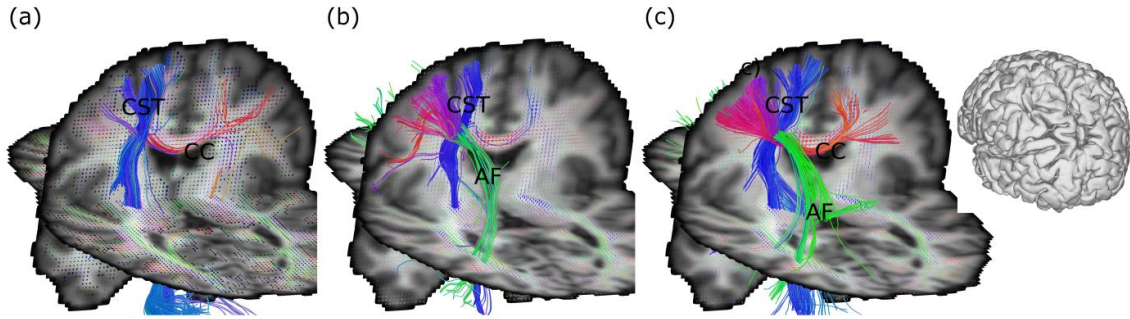


Figure 7.3: Comparison of tracking methods. From left to right the results from tensor deflection (a), spherical harmonic streamline tracking (b) and the results of the Bingham fit based peak deflection approach (c) are visualized. For selection of the bundles a selection box was positioned in the crossing region. The same box was used for all three datasets. For orientation an iso-surface of the brain is shown in the top right. The view is from posterior left. The main bundles are labeled (CC: corpus callosum, AF: arcuate fasciculus, CST: corticospinal tract). In the background the used local models are depicted, i.e. (a) the diffusion tensor, (b) the fODF and (c) the Bingham functions.

The fibers were visualized using as well textured triangle strips and point sprites employing GPU programming (Merhof et al., 2005) as GPU based glyph visualization (Hlawitschka et al., 2008). As can be seen the tensor tracking is not able to completely resolve the crossing, but instead finds only the corticospinal tract and parts of the corpus callosum. In fODF streamline propagation the spreading of fibers in the crossing area between the arcuate fasciculus and the corticospinal tract is resolved. However, the corpus callosum is not resolved completely. The fODF peak deflection algorithm is able to clearly represent each of the bundles present in the crossing area. The local smoothness and robustness is reflected on a global scale as can be seen from the comparison of the tractography results.

## 7.5 Conclusion

Corresponding diffusion signals were calculated for the three largest fiber bundles present in a voxel. This was done by fitting the peaks of the fODF with Bingham distributions and forward calculating the diffusion signal. Then a diffusion tensor was estimated for each of these signals and then a tensor deflection algorithm was applied, which was modified for multiple tensors being present in each voxel.

The fODF peak deflection algorithm was able to produce a tracking result, which in contrast to tensor tracking is able to resolve the crossing areas properly and uses more of the fODF

information, than the fODF streamline approach (see Figure 7.3). It can be seen that the information on the peak spread is necessary for completely resolving the crossings. The resulting fiber tracts of the fODF peak deflection algorithm are very smooth in comparison to the fODF streamline results. This phenomenon has been described by Westin and colleagues (Westin et al., 2002) as well as Lazar and colleagues (Lazar et al., 2003) for the tensor deflection case, as it introduces a regularization of the curvature of the reconstructed streamlines. This allows a more robust reconstruction compared to the fODF streamline propagation algorithms, based on extracting the peaks and following the local maxima. This approach takes advantage of the peak separation. The peak separation enables directly identifying the bundle used for tracking and thereby would allow direct mapping of parameters estimated for each of the peaks onto the tracking result.

It has been shown that simply by using the multi-directional information of the fODF for streamline tracking, the result drastically improves tensor tracking and is one of the most accurate tractography approaches (Fillard et al., 2011). Further evaluation of the quality of the proposed tractography method would be necessary to quantify the increase in accuracy compared to the streamline fODF approach. The fODF peak deflection algorithm is only one realization of a tensor tracking algorithm applied to the fODF by the peak fitting framework introduced in Chapter 5. This framework can easily be applied to more sophisticated tractography methods based on the diffusion tensor. Therefore the contribution of this work lies not only in the introduction of a more accurate tractography algorithm, but in presenting a framework for applying tensor based algorithms to spherical deconvolution results.

# 8 Fetus Data Analysis

---

## 8.1 Introduction

Investigation of the development of the human brain using dMRI based analysis is becoming increasingly important (Blondiaux and Garel, 2012). Since the fetal brain is much smaller than the adult brain many of the standard techniques for data acquisition and evaluation are inadequate. This presents a whole number of challenges for developing appropriate algorithms and methods as well for measuring the fetal brain data as for data processing and modeling.

One of the main questions in the analysis of fetal brain data is assessing if the brain's development is progressing in a normal manner. The point of interest is therefore the investigation of dMRI based metrics which describe the microstructure and allow for the analysis of the morphological changes. Since the Bingham metrics give a direct connection to the underlying microstructure, they are well suited for this type of analysis. So far the brain's development is measured mainly by using the brain's size and weight (Guihard-Costa and Larroche, 1992), volume (Gholipour et al., 2011; Habas et al., 2008), degree of gyrification (Chi et al., 1977), laminar organization (Z. Zhang et al., 2011) as well as simple DTI derived metrics (Huang et al., 2012).

In this chapter I present the application of the Bingham fit based metrics to fetal dMRI. Besides using the Bingham metrics themselves the change of the distribution of the values of the different metrics was observed. The more the brain develops the more it changes from a homogenous to a heterogeneous microstructural composition. An easy way to describe the distribution of the metrics for different ages is using 2D histograms of two metrics (developmental fingerprints). In the collaborative work with Viehweger and colleagues (Viehweger et al., 2013) the *Gini coefficient* (GC) was introduced as a way to describe the homogeneity of the measured values and therefore the brain's developmental age. The GC (Gini, 1912) is a dimensionless number, which broadly speaking describes the inequality amongst values of a frequency distribution. It is used in a variety of contexts, such as for example economics (Sen, 1983), biology (Damgaard and Weiner, 2000) and even astrophysics (Lisker, 2008).

Fetus	Age [weeks]	Diagnostics, prenatal	Diagnostics, postmortem
1	22	Premature rupture of membranes (PROM)	
2	20	Malformation of the heart, micrognathism	Hands with only 4 fingers
3	31	Lissencephaly of the parietal lobe	Migrational disorder (minor)
4	21	Spontaneous abortion	
5	18	Turner- syndrome	
6	19	Potter- syndrome	Agenesis kidneys
7	20	PROM, anhydramnia	Gastroschisis
8	24	Trisomy 18	
9	16	Generalised edema, micrognathism, no swallowing, club foot	Cystic hygroma of the neck
10	20	Potter- syndrome	Agenesis kidneys
11	23	PROM	
12	36	Trisomy 21	
13	17	Trisomy 18	
14	25	Skeletal dysplasia	
15	20	Spina bifida	Arnold- Chiari- malformation
16	21	Insufficiency of the cervix	
17	26	Skeletal dysplasia	
18	23	PROM, amniotic infection syndrome (AIS)	
19	19	PROM, AIS	
20	25	Placental insufficiency	
21	39	Placental insufficiency	
22	22	Skeletal dysplasia, hypochondrogenesis	
23	17	Abortian indicated due to medication of the mother	
24	22	PROM, AIS	
25	22	PROM	
26	22	Placental insufficiency	
27	23	Heterotaxia with vessel deformation	
28	21	Skeletal dysplasia	
29	19	PROM	
30	22	Spina bifida	
31	23	Spina bifida	

Figure 8.1: Data basis. List of the subjects used for the evaluation of metrics and reasons for truncation of the pregnancy. It additionally shows the age of the fetuses as well as the postmortem diagnostics. The age was determined using sonography as well as using morphological development milestones. The age included in this list is the age determined from sonography.

In the context of this analysis the GC is computed from the voxel-wise defined joint distribution of the metrics ADC, FA and CX. The hypothesis is that the GC correlates with the brain's developmental state, in other words that the GC is sensitive to the loss of homogeneity due to aging until the brain reaches a certain age.

The data analysis is based on 31 fetus scans, aborted due to a variety of causes (see Figure 8.1). Informed parental consent was obtained for all the following procedures, no financial incentives were given and the studies were approved by the ethics committee of the University of Leipzig. The specimens were kept at 4°C until they were scanned. The scans all happened within 24 hours of the termination of pregnancy. To not harm the brains structure all scans were conducted in-situ.

The work within this chapter is an original contribution. Part of it has been submitted (Viehweger et al., 2013).

## 8.2 Measurements

Since the fetal brain is too small for the use of standard MRI techniques, a more complex imaging protocol was used. As stated in the collaborative work with Viehweger and colleagues (Viehweger et al., 2013), the data was acquired using a 3T whole-body MR scanner (Tim Trio 3T, Siemens Healthcare, Erlangen, Germany) equipped with Siemens-AC038 whole body gradient coils (peak gradient strength:  $38 \frac{mT}{m}$ , maximum slew rate:  $200 \frac{T}{m \cdot s}$ ), and an 4 channel phased array RF knee coil. 48 axial slices were acquired with a 2D single shot DW-STEAM-EPI (TR/TE/Delta/delta = 12000/59/121/16ms) sequence giving 0.7 mm isotropic resolution. The TE, diffusion time, and gradient duration were optimized to provide maximum SNR for a maximum b-factor of  $1600 \text{ s } mm^{-2}$ . The bandwidth was  $950 \frac{Hz}{pixel}$ . K-space was partially sampled at 5/8 and parallel imaging was not used. The DWI protocol was acquired with 60 gradient directions at b-value of  $1600 \text{ s } mm^{-2}$  and 6 directions at  $150 \text{ s } mm^{-2}$ . The measurement was repeated 9 times, taking a total of 1 hour 38 minutes. A vendor-provided spatial matched filter approach that linearly combines complex image data from different receiver coils at each pixel separately was used for reconstructing the multichannel data from the phase array coils. The weights for the linear combination were derived from the sensitivities of each coil in that pixel and the noise correlation matrix. The virtual autopsy was performed on a 3.0 T scanner, SIEMENS, Germany. The employed sequences were T2-Trufi, T2-Trufi dynamic and T1 GE.

After acquiring the data FLIRT was used (Jenkinson et al., 2002) to remove motion artifacts caused by the vibration of the scanner (Gallichan et al., 2010) and calculated the diffusion tensor, the ADC and the FA. Then spherical deconvolution was applied using MRtrix (Tournier et al., 2012). As single fiber response manually selected regions of the corticospinal tract were used, which one can assume to be constituted of a single collinear fiber population. Basis for this mask was an FA mask, which was manually refined to mask only the brain. On the resulting fODF the Bingham fit was computed and the Bingham metrics were calculated. Then the developmental fingerprints and the Gini coefficient were determined from the ADC, FA and CX metrics for comparison of the different age groups.

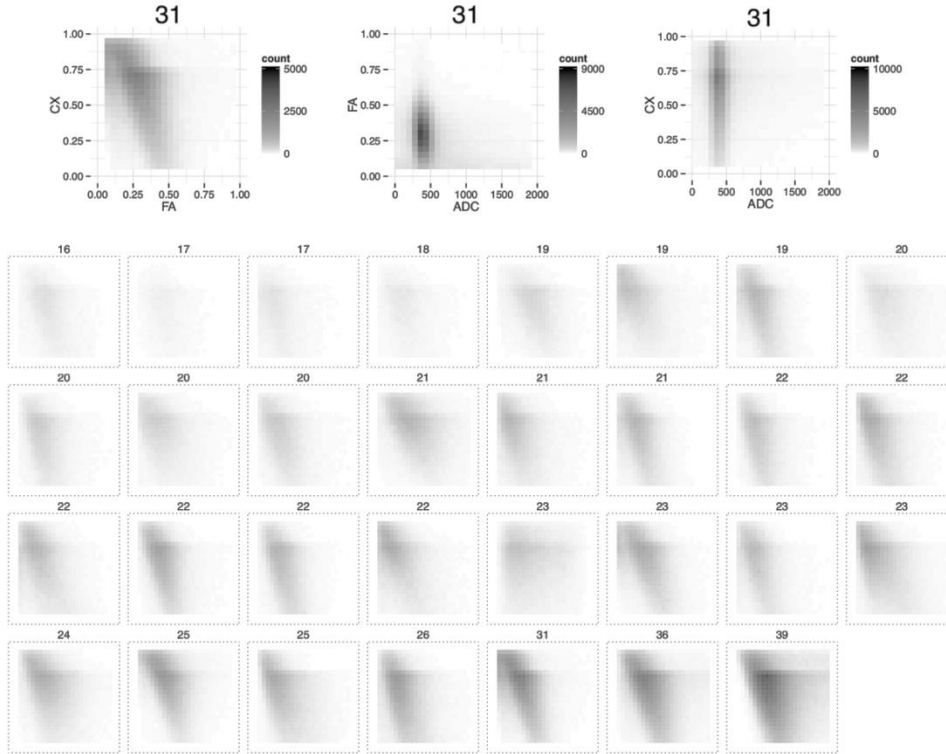


Figure 8.2: Developmental fingerprint. The top row shows an exemplar developmental fingerprint for each combination of metric using a 31 weeks old brain. Below the developmental fingerprint from FA and CX are shown as a function of age. As can be seen the fingerprints progress towards low FA and high CX values.

## 8.3 Results

The tensor metrics FA and ADC as well as the Bingham metrics were calculated and compared for different developmental ages of the brain. As can be seen they seem relatively independent of age and are unable to characterize structural changes. This is due to the limits of the tensor model. Next the Bingham metrics were investigated.

Due to strong variations in the kernel used for the calculation of the fODF on each of the datasets, a quantitative comparison of the calculated metrics is difficult. However, due to the large differences using a combined kernel is impossible as well. Additionally the strong variation in brain size makes quantitative comparison even more difficult due to very different amounts of partial volume effects occurring for the different age groups. One therefore is bound to not compare absolute but relative metrics.



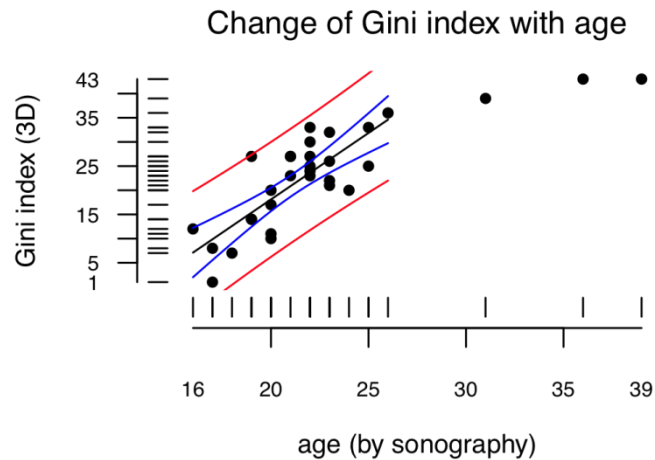


Figure 8.3: Connection between the Gini coefficient and age. As can be seen the Gini coefficient correlates well to the age in the range between 16 and 26 weeks. The red lines depict the 95% confidence interval and the blue line shows the prediction interval. Analysis of brain's older than 26 weeks was not possible in a meaningful way, due to the available data. It should be noted that the Gini coefficient is shown scaled by a factor of 100. The regression line is shown in black ( $y = 2.75x - 36.9$ ).

For this so called developmental fingerprints of two metrics were introduced. These are 2D histograms in which each bin corresponds to the number of voxels where both metrics fall into the respective interval. These histograms then describe the joint distribution of the two metrics. Due to them being most independent from changes in signal, the metrics FA, ADC and CX were chosen for further evaluations. An example for their developmental fingerprint is shown in Figure 8.2.

These developmental maps show a strong connection to the age of the fetal brain. However, these maps are difficult to assess quantitatively. For the quantitative analysis of the metric the GC, calculated from all three metrics, is used. In this context the GC describes the degree of inhomogeneity in the brain. The more homogenous the metrics are the lower the GC is. The hypothesis was that young brains are very homogenous and become more and more inhomogeneous during their development. This can be seen as the process of the brain progressively differentiating with age.

The GC was correlated with the brains age (estimated from somnography) and therefore its developmental state using a linear model. As shown in Figure 8.3 the GC is strongly connected to the brain's age for a range between 16 and 26 weeks. Outside this range it is difficult to assess the connection properly in this work, due to a lack of data.

## 8.4 Conclusions

The fODF and the Bingham metrics were calculated for a set of fetal datasets. In this study a strong relation between the developmental brain age and the GC calculated from FA, ADC and CX could be shown. This is a metric with a high potential for clinical use, as it is a simple quantitative metric, with high predictive strength. A further strong point of the use of the GC is that it can be calculated from any type of metric. It therefore can be easily adapted to newly developed HARDI metrics.

The scans the analysis is based on were conducted post-mortem. However, the goal of this work was to develop metrics which can be used for in utero diffusion imaging. Therefore in future work one would have to show that these findings transfer to such a setting. This requires estimating to which degree the found connections can be transferred to non-pathological fetuses, as most of the datasets used were from pathological fetuses. While only brains without macroscopic pathologies were used in the analysis, it cannot be guaranteed that no microstructural pathologies are present. This also implies that for the creation of Gini-coefficient nomograms in clinical use one would have to increase the number of samples significantly.

For a more detailed analysis of the Bingham metrics a follow up project has been defined in which the changes of the metrics are investigated over more locally constrained regions. In this case the analysis was done over the entire brain, which, due to the large differences in size and shape of the brains, did not allow for a good comparison of different areas within the brain. In future work it is planned to divide the brain manually into anatomical subsections in which the change in metrics can be compared quantitatively.

## 9 General Discussion

---

In this thesis I first investigated the local models focusing on their feasibility for deriving metrics. Hereby I introduced a common framework for the dODF approaches by Tristan-Vega and colleagues (Tristán-Vega et al., 2009) as well as Aganj and colleagues (Aganj et al., 2010). Due to the explicit connection between the fODF and the microstructure, I chose the fODF as local model basis for the metrics. I investigated the meaning of the coefficients of the SH representation and derived the connection between the first coefficient and the integral of the expanded function over the sphere, but did not find an easily interpretable connection between the higher order coefficients and the geometry. I therefore decided to research a parameterization of the fODF which is more easily interpretable. The first assumption was that each of the peaks of the fODF represents a single collinear fiber population. This is a reasonable assumption, as the fODF formally describes an angular spatial fiber density. The Bingham function was used, which is a scaled Bingham distribution for approximating the peaks. The basis for this was the assumption of having Bingham distributed fibers in each population, as the Bingham distribution can be seen as the spherical extension of the normal distribution. Similar approaches have been used by others, too, but not in the context of characterizing the fODF peaks for establishing metrics (Kaden et al., 2007; Kiran K Seunarine et al., 2007). Next I defined and investigated numerous metrics derived from the fitted Bingham distributions and verified the meaningfulness of these metrics through the use of simulation and phantom data analysis. After showing the connection to the ground truth and the relation to the FA, these metrics were used for computing maps of the human brain. Finally the extracted metrics and the Bingham functions were applied to tractography as well as the analysis of the morphological changes in the developing brain. Several parts of this work were presented and three papers describing the Bingham fit method, its application and specific findings are currently under review (Riffert et al., 2013; Schreiber et al., 2013; Viehweger et al., 2013).

The main result of this thesis is a method for classification of the peaks of the fODF and derivation of voxel-wise metrics which are meaningfully connected to the ground truth fiber arrangement and the properties of the fiber populations present within the voxel. These metrics were used for generation of parameter maps. This is, however, not the most useful way to display this metrics. Rather they can be used for investigation of the spatial variation of metrics along fiber populations. This is done by combination of tractography with the bundle-wise metrics. In the work of Schreiber and colleagues (Schreiber et al., 2013) the

variation of the Bingham metrics is investigated across fiber populations. This allows for example answering questions on the behavior of fibers in the vicinity of crossings, i.e. do fibers branch out or does their density increase. Furthermore it enables us to increase the specificity of FA. If a change in FA is observed in an area, for example due to a learning task, then one is able to investigate what structural change causes the FA change. This endows results with further meaning making them more interpretable. As shown by the application of the Bingham metrics on the fetal brain datasets, the metrics can be used for the characterization of structural changes due to development. Further application in analysis of anatomical change (e.g. tumor) seems promising. Overall the Bingham fit and related metrics are a step which brings us closer to the description of anatomy using metrics derived from MRI.

One of the very significant aspects of this work, which was not anticipated in the beginning, was the analysis of the SH expansion of the fODF by means of the fitted Bingham functions. The main result is that the SH base is probably not a particularly useful expansion, when the peak information is the property of interest. This is analogous to not using a Fourier series expansion when the main characteristics of interest are the maxima of a function, since the oscillating base functions lead to spurious peaks. The low number of sampling points further amplifies this effect, since it leads to a low maximum order for the SH expansion (maximum of 8<sup>th</sup> order for 60 directions).

If one combines the results from the analysis of crossing angles (Chapter 4.5.6), the Dirac delta function (Chapter 4.5.5) and the Bingham metrics connection to simulated ground truth values (Chapter 6.6.3), one can see the flaws of the SH representation of the fODF manifest. These are mainly (1) the introduction of spurious crossings correlating with the approximation error of the Dirac delta function and (2) the related problem of not being able to represent structures sharper than a certain threshold, which manifests in the peak spread becoming constant and equal to the sharpest representable spread even for an 8<sup>th</sup> order SH reconstruction. The correlation between the crossing angles and the spurious peaks of the Dirac delta approximation, however, might allow identification of spurious peaks by observing the change in crossing angle when using a different SH order, since the spurious peaks do not align for different SH orders.

The first of these two flaws has extensive consequences for tractography based on the fODF, since the peak directions are followed without discerning between true and spurious peaks. Distinguishing the spurious peaks from the true peaks is a difficult if not impossible task in scenarios where the ground truth is not known, as one would need to establish that the present microstructure is not responsible for the observed fODF peak configuration. Here again different order approximations might give a hint. The second problem makes

interpretation of microstructure close to impossible in the corresponding areas, as sharper peaks appear to have the same width. With high enough angular resolution one would theoretically be able to represent the sharper peaks by using higher SH order. When using higher orders other problems gain significance, which are the susceptibility to noise and the need for regularization. On the surface regularization does not seem like a big problem, however, as stated higher orders are needed for describing the sharp peaks. Regularization suppresses higher orders artificially reducing the overall order.

In my opinion the solution to both of these problems lies in the use of a different set of base functions. Especially the oscillating nature of the SH functions is critical when trying to describe functions, whose main feature is their peak structure. Of course this in turn means more difficult calculation of the deconvolution itself, as this base is prone to not having a simple convolution theorem. An approach which partially utilizes this is the dampened Richardson-Lucy approach, Dell'Aqua and colleagues use for deconvolution (Dell'Acqua et al., 2007). Overall a different base would need the properties of being able to describe sharp functions, be suited for description of functions on the sphere and represent the attenuation signal profiles as well as the deconvolution result accurately even when working from a sparse representation.

One of the problems in extracting information on anatomical configurations is that distinct configurations can lead to the same diffusion profile and the same fODF for that matter, as shown in the work by Jones and colleagues (Derek K Jones et al., 2013). As mentioned there this can only be handled by using a higher spatial resolution, which again leads to problems regarding the isotropy of voxels or the SNR.

A different problem lies in the evaluation of the accuracy of metrics. I compared the derived metrics with simulated data and phantom data in order to estimate the accuracy. Using simulated data has the problem of only describing an optimal environment in which the influence of unknown properties (such as the true SNR and its distribution) is not properly reflected. This leads to the need for fiber phantoms. However, realistic phantoms with known ground truth of fiber configuration as well as known fiber properties do not exist so far. The phantom data used (Fillard et al., 2011) for example does not realistically reflect even simple metrics, such as FA. While the deconvolution process is able to eliminate this effect to a certain degree using a kernel of fibers from the phantom, one cannot be certain that some of the properties of the synthetic fibers used and their behavior are reflected in the metrics.

A question more closely related to this work is the question on how to avoid the Bingham function overlap occurring due to the separate fit of the Bingham functions to the fODF peaks. There are two approaches to this: (1) Fitting the Bingham functions simultaneous

instead of separately or (2) using a cut off Bingham function for fitting only the peak. Fitting the Bingham functions simultaneously leads to problems similar to those in multi tensor fitting, reintroducing the model selection problem. This has been investigated for fitting the Bingham distribution to the diffusion signal (Kaden et al., 2007). Cutting off the Bingham function leads to a violation of the fibers within each bundle being Bingham distributed.

All the methods introduced in this work are implemented ready to use in the open source software BrainGL (<https://code.google.com/p/braingl/>). Furthermore the methods are integrated in a standard protocol used for the processing of fetal datasets.

Can we meaningfully characterize the voxel-wise bundle microstructure in terms of metrics derived from HARDI measurements? This was the question which we stated as the central point of this thesis. The answer is yes, within the accuracy of the fODF model, we can.

# 10 Abbreviations

---

ADC:	apparent diffusion coefficient.
AF	arcuate fasciculus
AFD:	angular fiber density.
AFD <sub>max</sub> :	maximum angular fiber density.
CC:	corpus callosum.
c-dODF:	circular orientation density function.
c-OPDT:	circular orientation probability density transform.
CSD:	constrained spherical deconvolution.
CSF:	cerebrospinal fluid.
CST:	cortical spinal tract.
CX:	complexity.
dMRI:	diffusion weighted MRI.
dODF:	diffusion orientation density function.
DTI:	diffusion tensor imaging.
EAP:	ensemble-average propagator.
EPI:	echo-planar imaging.
FA:	fractional anisotropy.
FD:	fiber density.
FF:	fiber fraction.
fODF:	fiber orientation density function.
FOV:	field of view.
FS:	fiber spread.
GC	Gini coefficient.
GFA:	generalized fractional anisotropy.
GRAPPA:	generalized auto calibrating partially parallel acquisitions.
HARDI:	high angular resolution diffusion imaging.

HMOA:	hindrance modulated orientational anisotropy
MD:	mean diffusivity.
MPRAGE:	magnetization prepared rapid acquisition gradient echo.
MRI:	magnetic resonance imaging.
NMR:	nuclear magnetic resonance.
PDE:	partial differential equations.
p-dODF:	planar orientation density function.
PFA:	peak fractional anisotropy.
p-OPDT:	planar orientation probability density transform.
QBI:	q-ball imaging.
SH:	spherical harmonics.
SNR:	signal-to-noise ratio.
TE:	echo time.
TR:	repetition time.



# 11 List of Figures

---

Figure 2.1: MRI images and fiber reconstruction. On the left a T1 image is shown (a). On the right the corresponding fiber reconstruction from dMRI is shown (b). Both images are visualized with an iso-surface calculated on the basis of the dMRI dataset. .... 6

Figure 2.2: Full Brain. This image was taken from the brain museum ([www.brainmuseum.org](http://www.brainmuseum.org)). The image shows a coronal slice taken from a human specimen. One can clearly observe the white matter (a) and grey matter (b). As can be seen the grey matter area close to the surface (cortex) is darker, while the more central white matter areas are lighter. The areas marked as ventricles (c) are filled with CSF. The difference in composition of these types of tissue is the main cause for contrast in MRI. .... 7

Figure 2.3: The anatomic reference planes. Images acquired in MRI are usually presented in terms of section on reference planes. In (a) we see the axial, in (b) the coronal and in (c) the sagittal reference plane. Additionally the terminology used for describing directions is introduced. .... 8

Figure 2.4: Significant fiber bundles. In this image some of the most significant fiber bundles, which are used in this thesis and their location in the brain are shown. On the left (a) the corticospinal tract (CST) is shown in blue, while the arcuate fasciculus (AF) is shown in red. On the right (b) the corpus callosum is depicted. It is divided into a frontal (red), medial (orange) and lateral (yellow) section. .... 9

Figure 2.5: Spins in a magnetic field. In a magnetic field, nuclei (which due to their spin act as small magnets) align with the external field's axis. They hereby precess around the field's axis. This precession is similar to the precession of a gyroscope. It is characterized by its frequency and its phase. The frequency defines how fast a spin is rotating and the phase defines the current position of rotation. The frequency of precession is called the Larmor frequency  $\omega_L$  and depends on the external  $B_0$  field's strength, as well as the nuclei specific gyromagnetic ratio. .... 11

Figure 2.6: The two energy states. The two energy states a nucleus can take are a low energy state (parallel) shown in (a) and a high energy state (anti-parallel) shown in (b). The difference in energy states is  $\Delta E = E_2 - E_1 = \hbar \omega_L / 2\pi$ . Due to thermal effects, a slightly higher number of nuclei are in parallel than in anti-parallel alignment with the external field. This leads to an excess magnetization of a substance in the magnetic

field in alignment with the orientation of the B0-field. This is also referred to as net-magnetization. ....	12
Figure 2.7: Axial view of a T1 and a T2 image. The composition of the tissue is the source for the contrast in MRI. In (a) the light areas correspond to white matter areas. The grey areas show the grey matter, while the CSF shows no signal and is therefore dark. In (b) the dark areas correspond to white matter areas. The light areas show the grey matter, while the CSF shows a high signal and is therefore white.....	14
Figure 2.8: Connection between k-space and MR image. In (a) the k-space image, which was read line wise, is shown. In (b) the resulting MR image is shown. The connection between the two images is the 2D-Fourier transform. ....	16
Figure 2.9: The diffusion encoding process. In this image the influence of the diffusion gradient on the phase of the spins is visualized. In (a) we see the spins all in phase after the application of the RF pulse. Here the signal $S_0$ can be observed. In (b) the application of the diffusion gradient can be seen. The spins now possess a spatially varying phase. Due to diffusion the spins randomly displace, which causes the phase to lose its spatial connection (c). Afterwards a refocusing gradient is applied (d), which is the inverse of the gradient which was applied before. This should cause the spins to return to phase coherence. The diffusion has caused phase incoherence, which manifests in a signal $S_g$ that is smaller than the signal at phase coherence. ....	18
Figure 2.10: The Stejskal-Tanner pulse gradient echo diffusion sequence. This image show the application of different gradients, the RF pulses as well as the signal readout over time. The type of gradient is marked on the left. The letters $G_x$ , $G_y$ and $G_z$ mark the encoding gradients for the respective spatial direction, $G$ marks the diffusion gradient. At the top the repetition time (TR) is shown. The gradient length $\delta$ and the time $\Delta$ during which the particles diffuse are marked as well. ....	19
Figure 3.1: The SH base functions. Here glyphs of the SH base functions are shown for orders $l = 0, 2, 4, 6$ . Negative function values are indicated in grey and positive values in color, indicating direction. ....	24
Figure 4.1: The diffusion tensor. The tensor is usually visualized as an ellipsoid. Here an isotropic (a) and an anisotropic tensor (b) are shown. The dimensions of the tensor are described by the tensor's eigenvalues ( $\lambda_i$ ) and eigenvectors ( $e_i$ ). The ellipsoid describes the distance a particle travels within the diffusion time $\tau$ . As the eigenvalues describe the dimensions of the tensor, similar eigenvectors indicate isotropy, while a difference between the eigenvalues indicates anisotropy. ....	38
Figure 4.2: Tensors colored using the RGB color map. The tensors are visualized as ellipsoids and colored using the first eigenvector. Red stands for left-right, green for anterior-	

posterior and blue for dorsal-ventral direction. Round tensors indicate more than one fiber population being present, while elongated tensors indicate collinear fiber populations. .... 40

Figure 4.3: Specificity and sensitivity of FA. On the left the same fiber configuration is shown. In the top image (a) the secondary fiber bundle (red) is increased, while in the second image the primary fiber population (blue) is decreased. Both of these changes lead to a reduction of FA. The FA therefore is sensitive to both changes, however cannot discern the changes. This implies that the FA is sensitive to changes in configuration, but not specific to the type of change. .... 42

Figure 4.4: Maps of tensor metrics. Here the tensor metrics are visualized using a coronal section. The metrics are FA (a), MD (b), AD (c), RD (d). Each of these metrics describes a different aspect of the shape of the diffusion tensor. .... 43

Figure 4.5: The principle of spherical deconvolution. In spherical deconvolution the signal is assumed to be constituted by the convolution of the signal of a single fiber (kernel) with a fODF. In theory the fODF is a sum of Dirac delta functions. Since spherical deconvolution is formulated in the space of spherical harmonic functions the fODF is blurred and appears rounder. .... 53

Figure 4.6: Effect of the CSD normalization. On the left (a) the first coefficient of the CSD is shown after normalization. On the right (b) the non-normalized image is shown. .... 56

Figure 4.7: fODF from spherical deconvolution mapped onto the brain. The glyphs are shown using an axial slice. As can be seen in the highlighted section, the fODF can discern crossing voxels, from non-crossing voxels. .... 57

Figure 4.8: Map of integral over the negative lobes. (a) absolute value of integral over negative lobes (b) relative value of integral over negative lobes. We can see the highest values occur in areas where only a single fiber population is present. .... 59

Figure 4.9: Approximation of Dirac delta function. The number of negative lobes of the Dirac delta function as well as the corresponding spurious positive peaks can be seen in (a). The higher the order is, the better the Dirac delta function is approximated, but the spurious peaks and negative lobes significantly increase as well. In (b) we see the corresponding CSD glyphs. The glyphs seem much larger for higher orders. However the integral of the CSD over the sphere is constant. The glyphs are perceived as larger due their increase in volume. .... 60

Figure 4.10: Connection between the crossing angle distribution and the SH reconstruction order. As can be seen the distribution's shape and peak vary greatly depending on the

spherical deconvolution order (90° for 4 <sup>th</sup> order, 70° for 6 <sup>th</sup> order and 50° as well as 90° for 8 <sup>th</sup> order). .....	63
Figure 5.1: The Bingham neighborhood and fit. The fODF is shown in light grey. The maximum direction $\mu_0$ of its largest peak is visualized as the red line. The directions of the Bingham distribution (green) are fitted using a small neighborhood of the maximum direction. The points considered part of the peak are those within the yellow line. To ensure that the neighboring peaks do not have too large an impact, only the neighbors of first, second and third degree are considered, which corresponds to the points in the blue area. ....	69
Figure 5.2: Fit of the fODF by Bingham functions. (a) fODF calculated by spherical deconvolution, (b) Bingham functions representing the separate peaks. The shape of each of the fitted Bingham functions closely corresponds to the fODF peak shape. ....	70
Figure 5.3: fODF and Bingham fit visualized on the brain. This image is taken from the coronal area, where the corticospinal tract and the corpus callosum cross. In (a) the fODF is shown. In (b) we see the Bingham fit for the largest peak, extracting the main bundle behavior. ....	71
Figure 6.1: Relation between the directional peak opening angle and the concentration parameters. On the left the Bingham function is shown in blue as polar plot (a). The green circle shows the value $f_0$ . The angle to the main direction of the Bingham function is noted as $\alpha$ . On the right the Bingham function is shown as function of $\alpha$ in Cartesian coordinates (b). The angle $\kappa$ describes the angle at which the function dropped to $\exp(-1/2)$ of its maximum value. ....	75
Figure 6.2: Comparison of FA and parameters of different fiber configuration. In the top row glyphs representing the fODF (purple) and the diffusion tensor (green) are visualized. Below a few of the Bingham metrics and the FA are shown for the larger and smaller peak. Image adapted from the work of Schreiber et al. (Schreiber et al., 2013). ....	78
Figure 6.3: Correlation of ground truth and reconstruction. Here the correlation of metrics calculated using the Bingham fit and their ground truth values are depicted. Ground truth and reconstructed values are shown in the unit of their respective metric. The left column shows metrics reconstructed for a single fiber population being present within a voxel. The middle and right column show the metrics for the first (middle column) peak and second (right column) peak in the case of fiber crossing. In each of the pannel the reconstructions are plotted for 6 <sup>th</sup> (blue) and 8 <sup>th</sup> (red) order SH series representation of the fODF. The lines show the linear regression results. The corresponding Pearson coefficients ( $R^2$ ) are displayed on the bottom right of each	

panel. As can be seen the spread of each of the parameters is smaller for the single fiber case, which leads to higher correlations..... 81

Figure 6.4: Correlation of CX as well as the crossing angle to the ground truth. Here the correlation for the metric CX as well as for the resolved crossing angle between the two peaks involved in the simulated crossing are shown. Colors and labels are same as in Figure 2. .... 82

Figure 6.5: Angular dependence of the metrics ground truth correlation on the fiber crossing angle. These plots show the how the correlation between the reconstructed values and the ground truth depends on the fiber crossing angle and the order of spherical harmonic series approximation. While the correlation of the values reconstructed from the largest peak are quite high (between 0.80 and 1.00), except for the area between 10° and 40°, where lower values can be observed for some parameters (FD, FS and especially  $\kappa_1$ ), the second peaks parameters do not correlate well with the ground truth until a crossing angle of 50° is reached. Generally the higher order reconstruction shows better correlation to the ground truth. .... 83

Figure 6.6: Metrics from phantom data. Here the metrics calculated from the phantom data are mapped upon the  $b_0$  image. The images were scaled for contrast. Values above the maximum value are set to red, ones below set to zero. The geometry is depicted in panel a). The metrics are shown in panels b) through l). .... 85

Figure 6.7: Primary metrics mapped on the human brain. Here the smoothed maps of the metrics FA, CX as well as the three metrics  $AFD_{max}$ , FD and FS which characterize the first peak are displayed. The metrics images were masked to the white matter using an FA map with a threshold of 0.15, which were manually expanded to match the white matter. These maps were then overlaid on an interpolated T1 image and scaled for contrast. The boundaries for the scaling are marked in the histograms at the bottom. The value n represents the number of voxels in which a certain value occurs. These are the images obtained from smoothing the original metrics before applying the white matter maps. The results without the smoothing steps can be found in Figure 6.11... 86

Figure 6.8: Metrics of secondary and tertiary fODF peaks. These maps were created as those in Figure 6.7, including the scaling and the histograms at the bottom. The maps for the non-interpolated metrics can be found in Figure 6.12..... 87

Figure 6.9: Correlation between metrics. This image shows the correlation structure of the metrics. For correlation purposes a white matter skeleton was used on which the metrics were mapped. All voxels for which either of the metrics was equal to zero was dismissed. As can be seen 3 clusters can easily be identified. The first contains FA, CX,  $AFD_{max1}$ , FD1, the second  $AFD_{max2}$ , FD2 and FS2, the third  $AFD_{max3}$ , FD3 and FS3. This

indicates a strong connection between FA, as well as shape of the first peak and the microstructural properties at the same time. ....	88
Figure 6.10: Spatial mapping of contribution to correlation with FA. The values correspond to the summands of the Pearson correlation coefficient. The average of these values over the whole masked region gives the correlation, which is shown in Figure 6.9. As can be seen, for $AFD_{max}$ , FD and CX high values (in case of CX) low values can be found in the main fiber bundles, i.e. especially in regions without major crossings. The FS shows small negative values mainly in areas without fiber crossings.....	89
Figure 6.11: Unsmoothed metric maps for the first peak, FA and CX. ....	90
Figure 6.12: Unsmoothed metric maps for the second and third peak. ....	91
Figure 7.1: Bingham fit derived tensors. Here the tensors calculated from the Bingham fit are shown mapped onto an axial slice of the brain.....	95
Figure 7.2: Bingham representation of peaks used in tractography. The colored peaks hereby represent peaks which the interpolation was based on. From these peaks then the diffusion signal and subsequently the tensor was calculated.....	96
Figure 7.3: Comparison of tracking methods. From left to right the results from tensor deflection (a), spherical harmonic streamline tracking (b) and the results of our peak deflection approach (c) are visualized. For selection of the bundles a selection box was positioned in the crossing region. The same box was used for all three datasets. For orientation an iso-surface of the brain is shown in the top right. The view is from posterior left. The main bundles are labeled (CC: corpus callosum, AF: arcuate fasciculus, CST: corticospinal tract). In the background the used local models are depicted, i.e. (a) the diffusion tensor, (b) the fODF and (c) the Bingham functions.....	97
Figure 8.1: Data basis. List of the subjects used for the evaluation of metrics and reasons for truncation of the pregnancy. It additionally shows the age of the fetuses as well as the postmortem diagnostics. The age was determined using sonography as well as using morphological development milestones. The age included in this list is the age determined from sonography.....	100
Figure 8.2: Developmental fingerprint. The top row shows an exemplar developmental fingerprint for each combination of metric using a 31 weeks old brain. Below the developmental fingerprint from FA and CX are shown as a function of age. As can be seen the fingerprints progress towards low FA and high CX values. ....	102
Figure 8.3: Connection between the Gini coefficient and age. As can be seen the Gini coefficient correlates well to the age in the range between 16 and 26 weeks. The red lines depict the 95% confidence interval and the blue line shows the prediction interval.	

Analysis of brain's older than 26 weeks was not possible in a meaningful way, due to our data basis. It should be noted that the Gini coefficient is shown scaled by a factor of 100. The regression line is shown in black ( $y = 2.75x - 36.9$ )..... 103

## 12 References

---

- Aboitiz, F., Scheibel, A.B., Fisher, R.S., Zaidel, E., 1992. Fiber composition of the human corpus callosum. *Brain Res* 598, 143–153.
- Abramowitz, M., Stegun, I.A., 1964. *Handbook of Mathematical Functions with Formulas, Graphs, and Mathematical Tables*, American Journal of Physics. Dover.
- Aganj, I., Lenglet, C., Sapiro, G., 2009. ODF reconstruction in q-ball imaging with solid angle consideration, in: ISBI. pp. 1398–1401.
- Aganj, I., Lenglet, C., Sapiro, G., Yacoub, E., Ugurbil, K., Harel, N., 2010. Reconstruction of the orientation distribution function in single- and multiple-shell q-ball imaging within constant solid angle. *Magn Reson Med* 64, 554–566.
- Alexander, A.L., Hasan, K., Kindlmann, G, Parker, D.L., Tsuruda, J S, 2000. A geometric analysis of diffusion tensor measurements of the human brain. *Magn Reson Med* 44, 283–291.
- Alexander, D.C., 2005a. Maximum Entropy Spherical Deconvolution for Diffusion MRI, in: IPMI. pp. 76–87.
- Alexander, D.C., 2005b. Multiple-fiber reconstruction algorithms for diffusion MRI., in: *Ann N Y Acad Sci*. pp. 76–87.
- Andersen, A.H., 1996. On the Rician distribution of noisy MRI data. *Magn Reson Med* 36, 331–333.
- Arsigny, V., Fillard, P., Pennec, X., Ayache, N., 2006. Log-Euclidean metrics for fast and simple calculus on diffusion tensors. *Magn Reson Med* 56, 411–421.
- Asselmlal, H.-E., Tschumperlé, D., Brun, L., Siddiqi, K., 2011. Recent advances in diffusion MRI modeling: Angular and radial reconstruction. *Med Image Anal* 15, 369–396.
- Atkinson, K., 1982. Numerical integration on the sphere. *The Journal of the Australian Mathematical Society Series B Applied Mathematics* 23, 332–347.
- Auld, D.S., Robitaille, R., 2003. Glial Cells and Neurotransmission : An Inclusive View of Synaptic Function Glial cells throughout the nervous system are closely. *October* 40, 389–400.



- Barnett, Alan, 2009. Theory of Q-ball imaging redux: Implications for fiber tracking. *Magn Reson Med* 62, 910–923.
- Basser, P J, 1995. Inferring microstructural features and the physiological state of tissues from diffusion-weighted images. *NMR Biomed* 8, 333–344.
- Basser, P J, Mattiello, J., LeBihan, D., 1994a. MR diffusion tensor spectroscopy and imaging. *Biophys J* 66, 259–267.
- Basser, P J, Mattiello, J., LeBihan, D., 1994b. Estimation of the effective self-diffusion tensor from the NMR spin echo. *J Magn Reson B* 103, 247–254.
- Behrens, T.E.J., Berg, H.J., Jbabdi, S., Rushworth, M.F.S., Woolrich, M.W., 2007. Probabilistic diffusion tractography with multiple fibre orientations: What can we gain? *Neuroimage* 34, 144–155.
- Bihan, D. Le, Breton, E., Lallemand, D., Grenier, P., Cabanis, E., Laval-Jeantet, M., Le Bihan, D., 1986. MR Imaging of Intravoxel Incoherent Motions: Application to Diffusion and Perfusion in Neurologic Disorders. *Radiology* 161, 401–407.
- Bingham, C., 1974. An Antipodally Symmetric Distribution on the Sphere. *The Annals of Statistics* 2, 1201–1225.
- Blaas, J., Botha, C.P., Peters, B., Vos, F M, Post, F.H., 2005. Fast and reproducible fiber bundle selection in DTI visualization, in: *VIS*. pp. 59–64.
- Bloch, F., 1946. Nuclear Induction. *Phys Rev* 70, 460–474.
- Blondiaux, E., Garel, C., 2012. Fetal cerebral imaging - ultrasound vs. MRI: an update. *Acta radiologica Stockholm Sweden* 1987.
- Brown, R., 1827. Brownian Motion. *Mathematica* 122, 471–493.
- Caan, M.W.A., Khedoe, H.G., Poot, D.H.J., Den Dekker, A.J., Olabarriaga, S.D., Grimbergen, K.A., Van Vliet, L.J., Vos, Frans M, 2010. Estimation of diffusion properties in crossing fiber bundles. *IEEE Trans Med Imaging* 29, 1504–1515.
- Callaghan, P.T., 1991. *Principles of Nuclear Magnetic Resonance Microscopy*. Clarendon Press, Oxford.
- Campbell, J., 2004. *Diffusion Imaging of White Matter Fiber Tracts*. McGill University.

- Canales-Rodríguez, E.J., Melie-García, L., Iturria-Medina, Y., 2009. Mathematical description of q-space in spherical coordinates: exact q-ball imaging. *Magn Reson Med* 61, 1350–1367.
- Catani, M., Bodi, I., Dell’Acqua, F., 2012. Comment on “The geometric structure of the brain fiber pathways”. *Science* 337, 1605; author reply 1605.
- Chen, B., Song, A.W., 2008. Diffusion tensor imaging fiber tracking with local tissue property sensitivity: phantom and in vivo validation. *Magn Reson Imaging* 26, 103–108.
- Chi, J.G., Dooling, E.C., Gilles, F.H., 1977. Gyral development in the human brain. *Annals of Neurology* 1, 86–93.
- Cook, P.A., Bai, Y., Hall, M.G., Nedjati-Gilani, S., Seunarine, K K, Alexander, D.C., 2005. Camino: Diffusion MRI reconstruction and processing, in: *Statistics*.
- Cory, D.G., Miller, J.B., Garroway, A.N., 1990. Time-suspension multiple-pulse sequences: applications to solid-state imaging. *Journal of Magnetic Resonance* 90, 205–213.
- Curran, E.J., 1909. A new association fiber tract in the cerebrum with remarks on the fiber tract dissection method of studying the brain. *J Comp Neurol Psychol* 19, 645–656.
- Daducci, A., McEwen, J.D., Van De Ville, D., Thiran, J.P., Wiaux, Y., 2011. Harmonic analysis of spherical sampling in diffusion MRI. *Imaging* 431, 1.
- Damgaard, C., Weiner, J., 2000. DESCRIBING INEQUALITY IN PLANT SIZE OR FECUNDITY. *Ecology* 81, 1139–1142.
- Dell’Acqua, F., Rizzo, G., Scifo, P., Clarke, R.A., Scotti, G., Fazio, F., 2007. A model-based deconvolution approach to solve fiber crossing in diffusion-weighted MR imaging. *IEEE Trans Biomed Eng* 54, 462–472.
- Dell’Acqua, F., Scifo, P., Rizzo, G., Catani, M., Simmons, A., Scotti, G., Fazio, F., 2010. A modified damped Richardson-Lucy algorithm to reduce isotropic background effects in spherical deconvolution. *Neuroimage* 49, 1446–1458.
- Dell’Acqua, F., Simmons, A., Williams, S.C.R., Catani, M., 2012. Can spherical deconvolution provide more information than fiber orientations? Hindrance modulated orientational anisotropy, a true-tract specific index to characterize white matter diffusion. *Hum Brain Mapp*.
- Descoteaux, M., 2010. High Angular Resolution Diffusion MRI : from Local Estimation to Segmentation and Tractography. PhD Thesis. University of Nice-Sophia Antipolis.

- Descoteaux, M., Angelino, E., Fitzgibbons, S., Deriche, R., 2007. Regularized, fast, and robust analytical Q-ball imaging. *Magn Reson Med* 58, 497–510.
- Descoteaux, M., Deriche, R., Knösche, T.R., Anwander, A., 2009. Deterministic and Probabilistic Tractography Based on Complex Fibre Orientation Distributions. *IEEE Trans Med Imaging* 28, 269–286.
- Descoteaux, M., Koay, C.G., Basser, Peter J, Deriche, R., 2010. Analytical q-ball imaging with optimal regularization, in: *ISMRM*.
- Dirac, P.A.M., 1982. *The Principles of Quantum Mechanics* (International Series of Monographs on Physics), 4th ed. Oxford University Press, USA.
- Driscoll, J.R., Healy, D M, 1994. Computing Fourier transforms and convolutions on the 2-sphere. *Advances in Applied Mathematics* 15, 202–250.
- Einstein, A., 1956. *Investigations on the Theory of the Brownian Movement*. Dover Pubns.
- Fick, A., 1855. Ficks first law of diffusion. *Ann Physik*.
- Fillard, P., Descoteaux, M., Goh, A., Gouttard, S., Jeurissen, B., Malcolm, J., Ramirez-Manzanares, A., Reisert, M., Sakaie, K., Tensaouti, F., Yo, T., Mangin, Jean-François, Poupon, C., 2011. Quantitative evaluation of 10 tractography algorithms on a realistic diffusion MR phantom. *Neuroimage* 56, 220–234.
- Fillard, P., Pennec, X., Arsigny, V., Ayache, N., 2007. Clinical DT-MRI estimation, smoothing, and fiber tracking with log-Euclidean metrics. *IEEE Trans Med Imaging* 26, 1472–1482.
- Gallichan, D., Scholz, J., Bartsch, A., Behrens, T.E., Robson, M.D., Miller, K.L., 2010. Addressing a systematic vibration artifact in diffusion-weighted MRI. *Hum Brain Mapp* 31, 193–202.
- Gholipour, A., Estroff, J.A., Barnewolt, C.E., Connolly, S.A., Warfield, Simon K, 2011. Fetal brain volumetry through MRI volumetric reconstruction and segmentation. *International journal of computer assisted radiology and surgery* 6, 329–339.
- Ghosh, A., Deriche, R., 2011. Extracting geometrical features & peak fractional anisotropy from the ODF for white matter characterization, in: *ISBI*. pp. 266–271.
- Gini, C., 1912. *Variabilità e mutabilità* (Variability and Mutability), *Memorie di metodologica statistica*.
- Gorczewski, K., Mang, S., Klose, U., 2009. Reproducibility and consistency of evaluation techniques for HARDI data. *MAGMA* 22, 63–70.

- Gudbjartsson, H., Patz, S., 1995. The Rician distribution of noisy MRI data. *Magn Reson Med* 34, 910–914.
- Guihard-Costa, A.M., Larroche, J.C., 1992. Growth velocity of some fetal parameters. I. Brain weight and brain dimensions. *Biology of the Neonate* 62, 309–316.
- Habas, P.A., Kim, K., Rousseau, F., Glenn, O.A., Barkovich, A.J., Studholme, C., 2008. Atlas-based segmentation of the germinal matrix from in utero clinical MRI of the fetal brain., in: *Med Image Comput Comput Assist Interv.* pp. 351–358.
- Healy, Dennis M., Hendriks, H., Kim, P.T., 1998. Spherical Deconvolution. *Journal of Multivariate Analysis* 67, 1–22.
- Hlawitschka, M., Eichelbaum, S., Scheuermann, G., 2008. Fast and Memory Efficient {GPU}-based Rendering of Tensor Data, in: *CGV.*
- Huang, H., Jeon, T., Sedmak, G., Pletikos, M., Vasung, L., Xu, X., Yarowsky, P., Richards, L.J., Kostovic, I., Sestan, N., Mori, Susumu, 2012. Coupling Diffusion Imaging with Histological and Gene Expression Analysis to Examine the Dynamics of Cortical Areas across the Fetal Period of Human Brain Development. *Cerebral cortex New York NY* 1991.
- Jenkinson, M., Bannister, P., Brady, M., Smith, S., 2002. Improved optimization for the robust and accurate linear registration and motion correction of brain images. *Neuroimage* 17, 825–841.
- Jessen, K.R., Mirsky, R., 1980. Glial cells in the enteric nervous system contain glial fibrillary acidic protein. *Nature* 286, 736–737.
- Jeurissen, B., Leemans, A., Jones, Derek K, Tournier, J.-D., Sijbers, J., 2010. Estimating the number of fiber orientations in diffusion MRI voxels: a constrained spherical deconvolution study, in: *ISMRM, 18th Scientific Meeting and Exhibition.* Stockholm, Sweden.
- Jian, B., Vemuri, B.C., 2007. A unified computational framework for deconvolution to reconstruct multiple fibers from diffusion weighted MRI. *IEEE Trans Med Imaging* 26, 1464–1471.
- Jones, Derek K, Knösche, T.R., Turner, R., 2013. White matter integrity, fiber count, and other fallacies: The do's and don'ts of diffusion MRI. *Neuroimage.*
- Kaden, E., Knösche, T.R., Anwender, A., 2007. Parametric spherical deconvolution: inferring anatomical connectivity using diffusion MR imaging. *Neuroimage* 37, 474–488.

- Kelso, N., Lee, S.-K., Bouchard, L.-S., Demas, V., Mück, M., Pines, A., Clarke, J., 2009. Distortion-free magnetic resonance imaging in the zero-field limit. *Journal of Magnetic Resonance* 200, 285–290.
- Khachaturian, M.H., Wisco, J.J., Tuch, D.S., 2007. Boosting the sampling efficiency of q-Ball imaging using multiple wavevector fusion. *Magn Reson Med* 57, 289–296.
- Kreher, B.W., Schneider, J.F., Mader, I., Martin, E., Hennig, J., Il'yasov, K.A., 2005. Multitensor approach for analysis and tracking of complex fiber configurations. *Magn Reson Med* 54, 1216–1225.
- Lauterbur, P.C., 1973. Image Formation by Induced Local Interactions: Examples Employing Nuclear Magnetic Resonance. *Nature* 242, 190–191.
- Lazar, M., Weinstein, D.M., Tsuruda, Jay S, Hasan, K.M., Arfanakis, K., Meyerand, M.E., Badie, B., Rowley, H.A., Haughton, V., Field, A., Alexander, A.L., 2003. White matter tractography using diffusion tensor deflection. *Hum Brain Mapp* 18, 306–321.
- Lenglet, C., Rousson, M., Deriche, R., 2006. DTI segmentation by statistical surface evolution. *IEEE Trans Med Imaging* 25, 685–700.
- Leow, A.D., Zhan, L., Zhu, S., Hageman, N., Chiang, M.-C., Barysheva, M., Toga, A W, McMahon, K.L., De Zubicaray, G.I., Wright, M.J., Thompson, P M, 2009. White matter integrity measured by fractional anisotropy correlates poorly with actual individual fiber anisotropy, in: ISBI. pp. 622–625.
- Lisker, T., 2008. Is the Gini coefficient a stable measure of galaxy structure? *The Astrophysical Journal Supplement Series* 179, 7.
- Makris, N., Papadimitriou, G.M., Worth, A.J., Jenkins, B.G., Garrido, L., Sorensen, A.G., Wedeen, V.J., Tuch, D.S., Wu, O., Cudkowicz, M.E., Caviness, V.S., Rosen, B.R., Kennedy, D.N., 2002. Diffusion Tensor Imaging, in: *Neuropsychopharmacology: The Fifth Generation of Progress*. LIPPINCOTT.
- Malcolm, J.G., Shenton, M.E., Rathi, Y., 2010. Filtered multitensor tractography. *IEEE Trans Med Imaging* 29, 1664–1675.
- Mansfield, P., 1977. Multi-Planar Image Formation using NMR Spin Echoes. *Journal of Physics C* 10, 55–58.
- Merboldt, K.D., Hanicke, W., Frahm, J., 1985. Self-diffusion NMR Imaging Using Stimulated Echoes. *J Magn Reson* 64, 479–486.

- Merhof, D., Sonntag, M., Enders, F., Hastreiter, P., Fahlbusch, R., Nimsky, C., Greiner, G., 2005. Visualization of diffusion tensor data using evenly spaced streamlines, in: VMV. Universit t Konstanz.
- Mori, S, Crain, B.J., Chacko, V.P., Van Zijl, P.C., 1999. Three-dimensional tracking of axonal projections in the brain by magnetic resonance imaging. *Ann Neurol* 45, 265–269.
- Moseley, M.E., Cohen, Y., Mintorovitch, J., Kucharczyk, J., Tsuruda, J., Weinstein, P., Norman, D., 1990. Evidence of Anisotropic Self-Diffusion. *Radiology* 176, 439–445.
- Onstott, T.C., 1980. Application of the bingham distribution function in paleomagnetic studies. *J Geophys Res* 85, 1500–1510.
- Pajevic, S., Pierpaoli, C., 1999. Color schemes to represent the orientation of anisotropic tissues from diffusion tensor data: application to white matter fiber tract mapping in the human brain. *Magn Reson Med* 42, 526–540.
- Parker, G.D., Marshall, A.D., Rosin, P.L., Drage, N., Richmond, S., Jones, D K, 2012. A pitfall in the reconstruction of fibre ODFs using spherical deconvolution of diffusion MRI data. *Neuroimage*.
- Parker, Geoffrey J M, Alexander, D.C., 2003. Probabilistic Monte Carlo based mapping of cerebral connections utilising whole-brain crossing fibre information., in: *Inf Process Med Imaging*. pp. 684–695.
- Pasternak, O., Assaf, Y., Intrator, N., Sochen, N., 2008. Variational multiple-tensor fitting of fiber-ambiguous diffusion-weighted magnetic resonance imaging voxels. *Magn Reson Imaging* 26, 1133–1144.
- Patel, V., Shi, Y., Thompson, Paul M, Toga, Arthur W, 2010. Mesh-based spherical deconvolution: a flexible approach to reconstruction of non-negative fiber orientation distributions. *Neuroimage* 51, 1071–1081.
- Penrose, R., 2008. A generalized inverse for matrices. *Mathematical Proceedings of the Cambridge Philosophical Society* 51, 406–413.
- Pierpaoli, C., Basser, P J, 1996. Toward a quantitative assessment of diffusion anisotropy. *Magn Reson Med* 36, 893–906.
- Pierpaoli, C., Jezzard, P., Basser, P J, Barnett, A, Chiro, G. Di, 1996. Diffusion tensor MR imaging of the human brain. *Radiology* 201, 637–648.
- Pooley, R.A., 2005. Fundamental Physics of MR Imaging<sup>1</sup>. *RadioGraphics* 25, 1087–1099.

- Poupon, C., Rieul, B., Kezele, I., Perrin, M., Poupon, F., Mangin, Jean-François, 2008. New diffusion phantoms dedicated to the study and validation of high-angular-resolution diffusion imaging (HARDI) models. *Magn Reson Med* 60, 1276–1283.
- Purcell, E.M., Torrey, H.C., Pound, R. V, 1946. Resonance absorption by nuclear magnetic moments in a solid. *Phys Rev* 69, 37.
- Rabi, I.I., Zacharias, J.R., Millman, S., Kusch, P., 1938. A New Method of Measuring Nuclear Magnetic Moment. *Physical Review* 53, 318.
- Raffelt, D., Tournier, J.-D., Rose, S., Ridgway, G.R., Henderson, R., Crozier, S., Salvado, O., Connelly, A., 2012. Apparent Fibre Density: a novel measure for the analysis of diffusion-weighted magnetic resonance images. *Neuroimage* 59, 3976–3994.
- Riffert, T.W., Schreiber, J., Anwender, A., Knösche, T.R., 2013. Beyond Fractional Anisotropy: Extraction of Bundle-Specific Structural Metrics from Crossing Fiber Models. *NeuroImage Submitted*.
- Scherrer, B., Warfield, S K, 2010. Why multiple b-values are required for multi-tensor models. evaluation with a constrained log-euclidean model, in: *ISBI*. pp. 1389–1392.
- Schreiber, J., Riffert, T.W., Anwender, A., Knösche, T.R., 2013. Tract-Based Analysis of Bundle-Specific Indices Derived from Diffusion MRI. *NeuroImage Submitted*.
- Schultz, T., Westin, C.-F., Kindlmann, Gordon, 2010. Multi-diffusion-tensor fitting via spherical deconvolution: a unifying framework., in: *Med Image Comput Comput Assist Interv*. pp. 674–681.
- Schwab, E., Afsari, B., Vidal, R., 2012. Estimation of non-negative ODFs using the eigenvalue distribution of spherical functions., in: *Med Image Comput Comput Assist Interv*. pp. 322–330.
- Sen, A., 1983. Poverty, Inequality and Development - Fields,Gs. *Economic Journal* 93, 239–240.
- Seunarine, Kiran K, Cook, P.A., Hall, M.G., Embleton, K. V, Parker, G J M, Alexander, D.C., 2007. Exploiting peak anisotropy for tracking through complex structures, in: *Computer Vision, IEEE International Conference On. Proc. IEEE 11th Int. Conf. Computer Vision ICCV 2007*, pp. 1–8.
- Song, S.-K., Sun, S.-W., Ramsbottom, M.J., Chang, C., Russell, J., Cross, A.H., 2002. Dysmyelination revealed through MRI as increased radial (but unchanged axial) diffusion of water. *Neuroimage* 17, 1429–1436.

- Stejskal, E.O., 1965. Use of Spin echoes in a pulsed magnetic-field gradient to study anisotropic,restricted diffusion and flow. *J Chem Phys* 43, 3292–3597.
- Stejskal, E.O., Tanner, J.E., 1965. Spin Diffusion Measurements: Spin Echoes in the Presence of a Time-DependentField Gradient. *J Chem Phys* 42, 288–292.
- Tabelow, K., Voss, H.U., Polzehl, J., 2012. Modeling the orientation distribution function by mixtures of angular central Gaussian distributions. *J Neurosci Methods* 203, 200–211.
- Takahashi, S., Yonezawa, H., Takahashi, J., Kudo, M., Inoue, T., Tohgi, H., 2002. Selective reduction of diffusion anisotropy in white matter of Alzheimer disease brains measured by 3.0 Tesla magnetic resonance imaging. *Neurosci Lett* 332, 45–48.
- Tanaka, H., 1999. Circular asymmetry of the paleomagnetic directions observed at low latitude volcanic sites. *Earth Planets and Space* 51, 1279–1286.
- Taylor, D.G., Bushell, M.C., 1985. The spatial mapping of translational diffusion coefficients by the NMR imaging technique. *Physics in Medicine and Biology* 30, 345–349.
- Tournier, J.-D., Calamante, F., Connelly, A., 2007. Robust determination of the fibre orientation distribution in diffusion MRI: non-negativity constrained super-resolved spherical deconvolution. *Neuroimage* 35, 1459–1472.
- Tournier, J.-D., Calamante, F., Connelly, A., 2012. MRtrix: Diffusion tractography in crossing fiber regions. *Int J Imag Syst Tech* 22, 53–66.
- Tournier, J.-D., Calamante, F., Gadian, D.G., Connelly, A., 2004. Direct estimation of the fiber orientation density function from diffusion-weighted MRI data using spherical deconvolution. *Neuroimage* 23, 1176–1185.
- Tristán-Vega, A., Westin, C.-F., Aja-Fernández, S., 2009. Estimation of fiber orientation probability density functions in high angular resolution diffusion imaging. *Neuroimage* 47, 638–650.
- Tristán-Vega, A., Westin, C.-F., Aja-Fernández, S., 2010. A new methodology for the estimation of fiber populations in the white matter of the brain with the Funk-Radon transform. *Neuroimage* 49, 1301–1315.
- Tuch, D., 2002. Diffusion MRI of Complex Tissue Structure. Harvard University and Massachusetts Institute of Technology.
- Tuch, D.S., 2004. Q-ball imaging. *Magn Reson Med* 52, 1358–1372.



- Viehweger, A., Riffert, T.W., Dithal, B., Knösche, T.R., Anwander, A., Bauer, M., Stepan, H., Sorge, I., Hirsch, W., 2013. The Gini-coefficient: A new method to assess fetal brain development. *Radiology* Submitted.
- Wedeen, V.J., Hagmann, P., Tseng, Wen-Yih Isaac, Reese, T.G., Weisskoff, R.M., 2005. Mapping complex tissue architecture with diffusion spectrum magnetic resonance imaging. *Magn Reson Med* 54, 1377–1386.
- Wedeen, V.J., Rosene, D.L., Wang, R., Dai, G., Mortazavi, F., Hagmann, P., Kaas, J.H., Tseng, W.-Y.Y.I., 2012a. The geometric structure of the brain fiber pathways. *Science* 335, 1628–1634.
- Wedeen, V.J., Rosene, D.L., Wang, R., Dai, G., Mortazavi, F., Hagmann, P., Kaas, J.H., Tseng, Wen-Yih I, 2012b. Response to comment on “the geometric structure of the brain fiber pathways”. *Science New York NY* 337, 1605.
- Weinstein, D., Kindlmann, G, Lundberg, E., 1999. Tensorlines: advection-diffusion based propagation through diffusion tensor fields, in: *VIS*. pp. 249–530.
- Westin, C.-F., Maier, S.E., Mamata, H., Nabavi, A., Jolesz, F.A., Kikinis, R., 2002. Processing and visualization for diffusion tensor MRI. *Med Image Anal* 6, 93–108.
- Yamada, K., Sakai, K., Akazawa, K., Yuen, S., Nishimura, T., 2009. MR tractography: a review of its clinical applications. *Magn Reson Med Sci* 8, 165–174.
- Zhang, N., Li, C., Jiang, T., 2013. An improved OPDT model in high angular resolution diffusion imaging. *J Math Imag Vision* 3.
- Zhang, Z., Liu, S., Lin, X., Teng, G., Yu, T., Fang, F., Zang, F., 2011. Development of laminar organization of the fetal cerebrum at 3.0T and 7.0T: a postmortem MRI study. *Neuroradiology* 53, 177–184.

# Curriculum Vitae

---

**Dipl.-Math. Till W. Riffert**



## Education

- Nov 2009 - Mai 2013    PhD student in computer science  
                                 Methods and development unit  
                                 “MEG and EEG - Cortical Networks and Cognitive Function”  
                                 Max Planck Institute for human cognitive and brain science
- Okt 2003 – Mai 2009    Diplom-Student  
                                 Major in mathematics, with focus on numerical mathematics  
                                 Minor in computer science  
                                 Friedrich-Schiller-Universität, Jena  
                                 Title of thesis: „Approximation und Simulation von Zufallsfeldern mit  
                                 Methoden der hierarchischen Matrizen“

## Publications

- 2013    Riffert, T., Schreiber, J., Anwander, A., & Knösche, T. R. (2013) *Beyond Fractional Anisotropy: Extraction of Bundle-Specific Structural Metrics from Crossing Fiber Models*. Submitted to NeuroImage
- Schreiber, J., Riffert, T., Anwander, A., & Knösche, T. R. (2013) *Tract-Based Analysis of Bundle-Specific Indices Derived From Diffusion MRI*. Submitted to NeuroImage
- Viehweger, A., Riffert, T., Dithal, B., Knösche, T. R., Anwander, A., Bauer, M., Stepan, H., Sorge, I. & Hirsch, W. (2013) *The Gini-coefficient: A new method to assess fetal brain development*. Submitted to Radiology

## Talks

- 2013    Viehweger, A., Riffert, T., Dhital, B., Knösche, T. R., Anwander, A., Sorge, I., & Hirsch, W. (2012). *The Gini-coefficient: A new method to assess fetal brain development*. Talk presented at 50. Meeting of the European Society for Pediatric Radiology (ESPR), 2013, Budapest

- 2012 Leuze, C., Bazin, P.-L., Anwander, A., Dinse, J., Wähnert, M., Riffert, T., Geyer, S., & Turner, R. (2012). *Cortical profiles of diffusion weighted imaging (DWI) data differ between cortical areas*. Talk presented at ESMRMB Congress 2012, 29th Annual Scientific Meeting. Lisbon, Portugal.

Viehweger, A., Riffert, T., Dhital, B., Knösche, T. R., Anwander, A., Sorge, I., & Hirsch, W. (2012). *Der Gini-Koeffizient: ein neuer Ansatz zur Charakterisierung des Entwicklungszustandes fetaler Hirne*. Talk presented at 49. Internationale Jahrestagung der Gesellschaft für Pädiatrische Radiologie. Düsseldorf, Germany.

- 2011 Riffert, T., Anwander, A., & Knösche, T. R. (2011). *Decomposition of the fiber orientation density function for parametric quantification of single fiber bundles*. Talk presented at ESMRMB CONGRESS 2011, 28th Annual Scientific Meeting, Leipzig, Germany.

## Poster

- 2012 Leuze, C., Anwander, A., Bazin, P.-L., Riffert, T., Geyer, S., & Turner, R. (2012). *Layer-dependent orientational structure in primary human somatosensory (S1) and motor cortices (M1)*. Poster presented at 18th Annual Meeting of the Organization for Human Brain Mapping (OHBM 2012), Beijing, China.

Riffert, T., Anwander, A., & Knösche, T. R. (2012). *Characterizing properties by fiber bundle parameters derived from the fODF*. Poster presented at 18th Annual Meeting of the Organization for Human Brain Mapping (OHBM 2012), Beijing, China.

Riffert, T., Knösche, T. R., & Anwander, A. (2012). *Quantification of fiber bundle properties using a decomposition of the fiber orientation distribution function*. Poster presented at 20th Annual Meeting of the International Society for Magnetic Resonance in Medicine, Melbourne, Australia.

- 2011 Riffert, T., Anwander, A., & Knösche, T. R. (2011). *Decomposition of the fiber orientation density function for parametric quantification of single fiber bundles*. Poster presented at ESMRMB CONGRESS 2011, 28th Annual Scientific Meeting, Leipzig, Germany.

Riffert, T., Anwander, A., & Knösche, T. R. (2011). *Parametric Quantification of Fiber Bundle Properties in Areas of Crossing Fibers*. Poster presented at CONNECT MEETING: MRI of Brain Micro-structure and Connectivity, Tel Aviv, Israel.

# Selbstständigkeitserklärung

---

Hiermit erkläre ich, die vorliegende Dissertation selbständig und ohne unzulässige fremde Hilfe angefertigt zu haben. Ich habe keine anderen als die angeführten Quellen und Hilfsmittel benutzt und sämtliche Textstellen, die wörtlich oder sinngemäß aus veröffentlichten oder unveröffentlichten Schriften entnommen wurden, und alle Angaben, die auf mündlichen Auskünften beruhen, als solche kenntlich gemacht. Ebenfalls sind alle von anderen Personen bereitgestellten Materialien oder erbrachten Dienstleistungen als solche gekennzeichnet.

.....

(Ort, Datum)

.....

(Unterschrift)